SUPERNOVAE AS GAMMA RAY EMITTERS FROM THE MEV TO THE TEV

BY

XILU WANG

DISSERTATION

Submitted in partial fulfillment of the requirements
for the degree of Doctor of Philosophy in Astronomy
in the Graduate College of the
University of Illinois at Urbana-Champaign, 2018

Urbana, Illinois

Doctoral Committee:

Professor Brian D. Fields, Chair
Professor Paul M. Ricker
Professor Tony Wong
Professor Charles F. Gammie

Abstract

Gamma rays offer unique probes of supernovae as cosmic-ray accelerators and as nucleosynthesis sites. My thesis work focuses on how to explore these two aspects of supernovae.

(1) Both starburst galaxies and ultra luminous infrared galaxies are new gamma-ray source classes discovered by *Fermi* and TeV telescopes. These extreme star-forming galaxies have high supernova rates, and thus accelerating cosmic rays that collide with dense interstellar gas to produce gamma rays ($p_{\rm cr}p_{\rm ism} \rightarrow \pi^0 \rightarrow \gamma\gamma$). Indeed these galaxies are expected to be "thick" to cosmic-ray protons and thus act as "calorimeters", where a substantial fraction of cosmic-ray energy input is emitted in gamma rays. Here we build a one-zone, "thick-target" model implementing calorimetry and placing a firm upper bound on gamma-ray emission from cosmic-ray interactions. The model assumes that cosmic rays are accelerated by supernovae, and all suffer nuclear interactions rather than escape. Our model has only two free parameters: the cosmic-ray proton acceleration energy per supernova $\epsilon_{\rm cr}$, and the proton injection spectral index s. We calculate the pionic gamma-ray emission from 10 MeV to 10 TeV, and derive the thick-target parameters for six galaxies with *Fermi*, *H.E.S.S.*, and/or *VERITAS* data. Our model provides good fits for the M82 and NGC 253, and yields $\epsilon_{\rm cr}$ and s values suggesting that supernova cosmic-ray acceleration is similar in starbursts and in our Galaxy. We find that these starbursts are indeed nearly if not fully proton calorimeters. For NGC 4945 and NGC 1068, the models are consistent with calorimetry but are less well-constrained due to the lack of TeV data. However, the Circinus galaxy and the ultraluminous infrared galaxy Arp 220 exceed our pionic upper-limit; possible explanations are discussed.

(2) In our own Galaxy, any supernova explosion would be a spectacular "once in lifetime" event. Tragically, a Galactic Type Ia supernova (SNIa) could go entirely unnoticed due to the large optical and near-IR extinction in the Milky Way plane, low radio and X-ray luminosities, and a weak neutrino signal. But fortunately SNIa emit nuclear gamma-ray lines from ^{56}Ni $\rightarrow^{56}$ Co $\rightarrow^{56}$ Fe radioactive decays. These lines fall within the *Fermi*/GBM energy range, and the ^{56}Ni 158 keV line is detectable by *Swift*/BAT. Both instruments frequently monitor the Galactic plane, which is transparent to gamma rays. Thus GBM and BAT are ideal Galactic SNIa early warning systems. We simulate SNIa MeV light curves and spectra to show that GBM and BAT could confirm a Galactic SNIa explosion, followed by *Swift* localization and observation in X-rays and UVOIR band. The time needed to sound the alarm depends on the ^{56}Ni distribution, and can be as early as a few days if $\gtrsim 10\%$ of the ^{56}Ni is in an exterior shell as suggested by SN2014J gamma data

To my family.

Acknowledgments

Foremost, I would like to thank my advisor Prof. Brian Fields, for his continuous support of my graduate life. I am very grateful for his patience, enthusiasm, and immense knowledge in guiding my research. Brian is always energetic and optimistic about research with full of interesting ideas, inspiring me to have affection for the work that I'm doing. Moreover, he helps me well prepared for the academic path: he is always there to answer any questions I have about research and academic stuff; and he encourages me to learn and practice necessary skills, such as giving talks, writing papers, talking science with people, with generous support in offering suggestions and opportunities. I could not have imagined having a better advisor for my Ph.D study.

Besides my advisor, I would like to thank the rest of my thesis committee: Prof. Paul Ricker, Prof. Charles Gammie, and Prof. Tony Wong, for their encouragement, insightful comments, and critiques. I am also thankful for the support and suggestions from my letter writer Prof. Paul Ricker in my postdoc application.

In addition, I would like to express my sincere gratitude to my collaborator and academic sister Amy Lien. She is very supportive for my research, and kind to share her academic experience with me. I really enjoy the discussion and collaboration with her.

I am also grateful for all the helpful and stimulating conversations with the professors and postdocs in the astronomy department, physics department and NCSA. My research benefited a lot from their suggestions.

Moreover, I really appreciate all the help from Jeri Cochran, Mary Margaret O'Connor, Rebecca Bare, Cory Holt, Judy Whittington, Kevin Pointer and Bryan Dunne, my graduate

life would not be so smooth without their help. I would also like to thank all the current and former graduate students in the astronomy department for their support and encouragement.

Last but not the least, my heartfelt thanks go to my family: my father Lin Wang, my mother Suping Yang and my pet Abu. I'm thankful for my parents' selfless love, firm support and endless encouragement throughout my life. No matter how far away I go, I know home is always there as my warm harbor and sturdy base. I would also like to thank my dog Abu, for being the best stress relievers and always cheering me up to survive any difficulties.

Table of Contents

List of Tables . . . . . **ix**

List of Figures . . . . . **x**

Chapter 1 Introduction **1**
1.1 Gamma Ray Astronomy 1
1.1.1 Gamma Ray Astronomy History 1
1.1.2 Gamma Ray Astronomy Features 4
1.2 Supernovae 4
1.2.1 Supernovae as Particle Accelerators 6
1.2.2 Supernovae as Nucleosynthesis Sites 8
1.2.2.1 Type Ia Supernovae 9
1.3 Dissertation Outline 11

Chapter 2 Are Starburst Galaxies proton calorimeters? **12**
2.1 Abstract 12
2.2 Introduction 13
2.3 The Thick-Target/Calorimetric Model 15
2.3.1 Model Assumptions 15
2.3.2 Cosmic-Ray Source and Propagation 17
2.3.3 Pionic Emission From Thick-Target Galaxies: the Calorimetric Model 19
2.3.4 Projectile CR Proton Index And Supernova Acceleration Energy/Efficiency 22
2.4 Model Results 24
2.4.1 Individual Starbursts 26
2.4.2 Calorimetric Limit 34
2.4.3 Neutrino estimation for individual starbursts 39
2.5 Discussion and Conclusions 40
2.6 Supplements 43
2.6.1 Order-Of-Magnitude Estimates 43
2.6.2 Energy Loss Rates 45
2.6.3 Code Description 48
2.6.4 Nuclear Enhancement Factor 48
2.7 Acknowledgments 51

Chapter 3 Using Gamma Rays as an Alarm for the Next Milky Way Type Ia Supernova 52
3.1 Abstract 52
3.2 Main Text 52
3.3 Methods 57
3.3.1 Models 58
3.3.2 Analytical formulas 61
3.3.3 Lightcurves 62
3.3.4 Localization 64
3.3.5 Discussion 65
3.4 Acknowledgments 67

Chapter 4 Conclusions 74
4.1 Preliminary and Future Work in Starburst Galaxies 74
4.1.1 The Extragalactic Gamma-ray Background Emission From Star-forming Galaxies 74
4.1.1.1 Introduction 74
4.1.1.2 Method 76
4.1.1.3 Discussion 79
4.1.2 Future Prospects of Starburst Study 80
4.2 Preliminary and Future Work in Type Ia Supernovae 82
4.2.1 Fermi/GBM background analysis and deep learning algorithm for supernova-like point sources search 82
4.2.1.1 Introduction 82
4.2.1.2 Method 83
4.2.1.3 Conclusion 86
4.2.2 Monte Carlo Simulations for SNIa Ejecta Model 86
4.2.3 Future Observations of Type Ia Supernova 86
4.2.3.1 Gamma Ray Observations 87
4.2.3.2 LSST Observation 90
4.3 Spallation of the R-process Elements from the Neutron Star Mergers 92

References 94

List of Tables

2.1 Parameters set for the starburst galaxies in Thick-Target Model. 27
2.2 Results for the starburst galaxies in Thick-Target Model. 28

List of Figures

2.1 Ratio of differential gamma-ray luminosity to total CR luminosity for a calorimetric galaxy. 25
2.2 Pionic gamma-ray spectra for NGC 253. 29
2.3 Pionic gamma-ray spectra for M82. 30
2.4 Pionic gamma-ray spectra for NGC 4945 and NGC 1068. 31
2.5 Pionic gamma-ray spectra for the Circinus galaxy and Arp 220. 32
2.6 Contour plots of χ^2 for our model fits to starburst galaxy data. 33
2.7 Plot of ratio of gamma-ray luminosity $(0.1 - 100\text{GeV})$ to total IR luminosity (8-100μm). 36
2.8 Proton Energy Losses. 47

3.1 Simulation of ^{56}Ni and ^{56}Co gamma-ray lines signal seen in a GBM/BGO detector. 68
3.2 Simulation of ^{56}Ni and ^{56}Co gamma-ray lines signal seen in a GBM NaI detector. 69
3.3 Simulation of on-axis ^{56}Ni and ^{56}Co gamma-ray lines signal seen in BAT detector. 70
3.4 Sketch of how the Earth occultation technique localizes a Galactic SNIa. . . 71
3.5 Sketch of the shell plus core model (shell model). 71
3.6 Minimum surface ^{56}Ni abundance $X_{^{56}\text{Ni}}$ versus the detected time for a 10 kpc Galactic SNIa. 72
3.7 Simulated light curves of the gamma-ray lines from a 10 kpc Galactic SNIa. . 73

4.1 The observed EGB and pionic contribution from star-forming galaxies. . . . 77
4.2 BGO background signal variation and BGO response to SNIa. 85
4.3 Simulation of light curves from a 10 kpc SNIa shells. 87
4.4 Simulated ^{56}Co lines energy spectra from a SNIa with the uniform ^{56}Ni distribution at day 21.6, 62.3 and 11.7 after the explosion, respectively. 88
4.5 Total number of gamma-ray detectable SNIa per 10 years by AMEGO. . . . 90

Chapter 1

Introduction

Gamma rays are the most energetic form of electromagnetic radiation, with photon energies above 100 keV. Generally, observed gamma-rays are non-thermal radiation. Thermal gamma-rays, especially at GeV and above energy, correspond to the blackbody sources with temperature as high as $T \geq 10^{12}K$, such objects are rare in the universe. As gamma-ray associated sources are interesting in astrophysics, such as supernovae, pulsars, gamma ray bursts, quasars and black holes, this emission offers unique probe of the extreme physical conditions in the universe. The Milky Way plane is optically thin to gamma-rays, thus gamma-ray emission can provide an unobstructed view in the Galaxy which complements the radio and far infrared observation. Moreover, gamma-rays from the extragalactic sources can help study the external galaxies and intergalactic environment.

1.1 Gamma Ray Astronomy

Gamma-ray astronomy is the astronomical observation of gamma rays, study of the corresponding astronomical sources and the related nuclear and particle astrophysics. It is a relatively young subject which is less than 100 years old, but is full of new discoveries.

1.1.1 Gamma Ray Astronomy History

The beginning of gamma-ray astronomy traced back to around 1950s, when the astronomers predicted that the universe would produce gamma rays through various processes, including cosmic ray interactions with the interstellar medium (ISM) gas, with magnetic fields, and

supernova explosions (e.g., Feenberg & Primakoff, 1948; Hayakawa, 1952; Morrison, 1958). However, due to the scattering and absorption of the Earth's atmosphere, most gamma rays coming from the space (below ∼TeV) can not reach the ground to be detected. Thus detectors above all or most of the atmosphere using balloons and spacecraft are required for the gamma-ray astronomy.

It was not until the 1960s that the gamma ray observation first became possible. Explorer XI in 1961 (Kraushaar et al., 1965), and its successor Orbiting Solar Observatory (OSO-3) in 1968 [1], were the first successful experiments with the hints of gamma rays from the Galactic plane. In the late 1960s and early 1970s, the military defense Vela satellites, designed for the detection of nuclear explosions on earth, detected gamma-ray bursts (GRBs) from deep space (Klebesadel et al., 1973). Then the gamma rays detectors on board Apollo 15 and 16 helped map gamma rays from lunar surface's radioactive decay as well as observed a diffuse background gamma rays. NASA's Small Astronomy Satellite-2 (SAS-2) was launched in 1972, confirmed the diffusive gamma-ray background discovered by OSO-3, and studied the Crab and Vela gamma-ray pulsars [2] (e.g., Thompson et al., 1975). The European COS-B satellite was launched in 1975, observed the sky for 7 years for point sources and diffusive galactic emission detections, and discovered the first extragalactic source 3C 273 (Swanenburg et al., 1978). The first solar flare gamma ray lines were discovered by OSO-7 in 1972 (Chupp et al., 1973), and the Solar Maximum Mission (SMM) launched in 1980 [3] (Forrest & Chupp, 1983). In 1979-1981, High Energy Astrophysical Observatory-3 (HEAO-3) detected 511 keV line from the electron-positron annihilation in the Galactic center (Mahoney et al., 1994).

The Compton Gamma-Ray Observatory (CGRO) was launched in 1991 and stayed in orbit for 9 years with greatly improved spatial and temporal resolution. It carried a Energetic Gamma Ray Experiment Telescope (EGRET) for energies above 30 MeV, a Compton Tele-

[1] https://heasarc.gsfc.nasa.gov/docs/heasarc/missions/oso3.html
[2] https://nssdc.gsfc.nasa.gov/nmc/spacecraftDisplay.do?id=1972-091A
[3] https://www2.hao.ucar.edu/mlso/solar-maximum-mission

scope (COMPTEL) working in 1-30 MeV, the gamma ray Burst and Transient Source Experiment (BATSE), and the Oriented Scintillation-Spectrometer Experiment (OSSE). BeppoSAX was launched in 1996 to study X-rays and also observe gamma-ray bursts [4]. And the High Energy Transient Explorer 2 (HETE-2) was launched in 2000 to study the connection between long GRBs and supernovae [5]. Since 2002, the Reuven Ramaty High Energy Solar Spectroscopic Imager (RHESSI) satellite is used for solar gamma-ray detections[6].

Currently the main space-based gamma-ray observatories are Neil Gehrels Swift Observatory (Swift), the INTErnational Gamma-Ray Astrophysics Laboratory (INTEGRAL), Fermi, and the Astrorivelatore Gamma ad Immagini Leggero (AGILE). Launched in 2002, INTEGRAL satellite measures nuclear lines and also photons from pointed sources[7]. It detected the gamma ray lines from ^{56}Ni decay in a Type Ia event SN2014J for the first time (Diehl et al., 2014; Churazov et al., 2015). Swift was launched in 2004 and carries the Burst Alert Telescope (BAT) for gamma-ray burst observations [8]. In 2007, AGILE was launched with a similar sensitivity to EGRET but a wider field of view [9]. Fermi was launched in 2008, including the Large Area Telescope (LAT) in GeV range, and the Gamma-ray Burst Monitor (GBM) in MeV range for studying gamma-ray bursts [10]. External star-forming galaxies are firstly observed in gamma rays by Fermi (e.g., Abdo et al., 2010a,d).

In TeV range, the cosmic gamma-ray induced showers in the atmosphere can be detected by ground-based experiments via the Cherenkov light. The first generation Atmospheric Cherenkov Telescope (ACTs) was in operation in early 1960s, and in late 1980s, the second generation ACTs started to be operational. The Whipple Telescope indirectly detected photons from the Crab Nebula direction in 1989 [11] (Punch et al., 1992). New generations

[4] http://www.asdc.asi.it/bepposax/
[5] http://space.mit.edu/HETE/spacecraft.html
[6] https://hesperia.gsfc.nasa.gov/rhessi3/
[7] http://sci.esa.int/integral/
[8] http://swift.gsfc.nasa.gov
[9] http://agile.rm.iasf.cnr.it
[10] http://www-glast.stanford.edu, https://gammaray.msfc.nasa.gov/gbm/
[11] http://linmax.sao.arizona.edu/help/FLWO/whipple.html

of ground-based ACTs in 2000s, like High Energy Stereoscopy System (H.E.S.S.) [12], VERITAS [13], MAGIC [14], HAWC [15] and CANGAROO [16], are now detecting blazars, supernova remnants, binary systems, pulsar wind nebular and unidentified sources with unprecedented sensitivity and resolution, complementary to current Fermi experiments.

1.1.2 Gamma Ray Astronomy Features

The mechanisms emitting gamma rays are diverse, and there are mainly two types gamma ray sources: GeV and above gamma-ray photons are indirectly from the interactions of cosmic rays coming from particle accelerators, including mechanisms like electron-positron annihilation, neutral pion decay, bremsstrahlung, inverse Compton scattering; MeV gamma-ray lines are directly from the radioactive decay of the elements from the nucleosynthesis sites in our universe. Gamma rays in GeV and above only come outside of our Solar System, and thus good for extrasolar, particularly extragalactic study, while MeV gamma rays are possibly from solar flares and the Earth's atmosphere. Therefore there are three major types of gamma ray astronomy study: (1) Diffusive gamma ray emissions, due to the interactions of cosmic rays; (2) Nuclear lines, coming from radioactive decay in our sun or the nucleosynthesis sites like supernovae in the universe; (3) Pointed sources which produce high energy particles, such as gamma ray bursts, pulsars, supernova remnants, blazars, and unidentified sources.

1.2 Supernovae

Supernovae (SN) occur during the last evolution stages of a star's life. Either a white dwarf or a massive star dies spectacularly in explosion with extraordinary luminosities, energet-

[12] https://www.mpi-hd.mpg.de/hfm/HESS/
[13] https://veritas.sao.arizona.edu
[14] https://wwwmagic.mpp.mpg.de
[15] https://www.hawc-observatory.org
[16] http://icrhp9.icrr.u-tokyo.ac.jp

ically emitting multi-messengers (photons, neutrinos and gravitational waves) and heavy elements synthesized, forming our current universe. Supernovae research is always fascinating to astronomers for centuries, as plentiful information about the supernovae and their surrounding environments can be gained in multiple ways, and involve studies in diverse fields like nuclear astrophysics, astroparticles, star formation, high energy astrophysics and cosmology.

Classification According to the light curves and the absorption lines appeared in the spectra observationally, supernovae can be generally classified into two types: Type I SN without hydrogen lines and Type II SN containing lines of hydrogen. While Type Ia SN (SNIa) can be further subdivided among Type I supernovae with the presence of strong silicon line. Another classification is based on the explosion type. A SNIa is caused by the completely disruption of a white dwarf due to the thermal runaway nuclear fusion, and thus also called as thermonuclear SN. While a core-collapse SN (CCSN) is caused by the explosion due to the expulsion of the outer layers, when a massive star collapses into a black hole or neutron star. CCSNs include Type Ib, Type Ic, and Type II supernovae.

Historical Supernovae and Milky Way Supernovae Rate Supernova study has a long history of more than 1000 years. The earliest supernova observation was in 185 AD for SN185 by Chinese astronomers, recorded as a "guest star" (e.g., Pisarski et al., 1984; Zhao et al., 2006). The brightest recorded supernova SN1006 was exploding in 1006 AD, and can be found in Chinese and Islamic literatures. The next four supernovae in record, observed with the naked eye in the history, are the famous SN1054 (created Crab Nebular), SN1181, SN1572 (produced Tycho Remnant) and SN1604 (Kepler's Supernovae). There were five Milky Way supernovae observed since 1000 AD with historical records (Stephenson & Green, 2002). Among them, SN1572 and SN1604 are confirmed Type Ia supernovae (Krause et al., 2008; Reynolds et al., 2007). With the development of telescopes, astronomers are

able to detect supernovae from external galaxies, starting with SN1885A discovered in M31 to thousands of supernova detections now, advancing our understanding of supernovae.

Milky Way supernovae are of particular interest and importance to astronomers. With a near distance less than 20 kpc, a Galactic supernova would be detectable by current detectors and provide valuable information for the studies in stellar evolution (SN progenitor types and explosion mechanisms), Galactic evolution (SN nucleosynthesis, remnants and environment feedback), and multi-messengers (SN as candidate sources for cosmic rays, neutrinos, gravitational waves). Using the historical records, we can estimate that the Galactic rate of SNIa is about 3 events per century. However, this estimation is in big bias with only two data points. In addition, no SNIa in our Galaxy has been seen since SN1604, this observation gap over 400 years may be due to the dust obscuration. Combing historical supernovae numbers with the observability simulation, Type Ia supernovae occur at a rate of ~ 1.4 events per century, while the CCSN rate is about 3.2 per century (e.g., Adams et al., 2013, and references therein). Although a Milky Way SN is rare on human timescales, the potential scientific impact merits preparations, and we look forward to seeing the next Galactic supernova in the multi-messenger era!

Supernovae are also important gamma ray sources, emitting gamma rays both directly from radioactive decay in MeV as nucleosynthesis sites, and indirectly in GeV and above energy, from the cosmic ray interactions, as particle accelerators. Combing the "old" supernovae study with the "young" gamma ray astronomy research can provide new insights into these two subjects and help improve our understandings about our universe.

1.2.1 Supernovae as Particle Accelerators

As supernovae are the final life stages of stars, they should be common in galaxies with strong star-forming activities. In addition, supernovae generally accelerate particles/cosmic rays through the diffusive shock acceleration (e.g., Blandford & Eichler, 1987). Thus star-

forming galaxies emit gamma rays indirectly through the interactions of cosmic rays, which are accelerated by the supernovae residing inside the galaxy.

Cosmic Ray Induced Gamma Rays Cosmic rays (CRs) are charged particles which are mostly protons with energy above 1 MeV, coming from the outside of our solar system and even from the external galaxies. The discovery of cosmic rays traced back to 1912 by Victor Francis Hess through a series of balloon experiments. And the source of cosmic ray was speculated as early as in 1934 by Baade & Zwicky (1934) to be supernovae. Since then, many cosmic ray experiments and theoretical studies have been conducted, and found various potential cosmic ray sources, including supernovae, active galactic nuclei, quasars, and gamma ray bursts. Cosmic rays are believed to be accelerated by supernova explosions (e.g., Baade & Zwicky, 1934; Ginzburg & Syrovatskii, 1964), proved by the pion decay feature of the gamma ray spectra from the supernova remnants IC443 and W44's observed by Fermi (Ackermann et al., 2013), and thus cosmic rays should be present in all star-forming galaxies. As CRs propagate in ISM, the inelastic collisions between CR and interstellar nuclei–both dominantly protons–lead to gamma-ray production at GeV and above energy range, via π^0 decay: $p_{\rm cr}p_{\rm ism} \rightarrow pp\pi^0, \pi^0 \rightarrow \gamma\gamma$ (Stecker, 1971; Dermer, 1986). This hadronic process occurs not only in the Milky Way, but also in other star-forming galaxies (e.g., Stecker & Venters, 2011; Abdo et al., 2009; Fields et al., 2010; Strong et al., 2010). Therefore cosmic-rays are both qualitatively and quantitatively probed by gamma-rays from the star-forming galaxies.

Starburst Galaxies "Starburst" is often used to describe an astrophysical process that involves star formation occurring at a much higher rate than the long-term average rate observed in most galaxies. Starburst can occur in entire galaxies or just regions of space, including blue compact starburst-galaxies, luminous infrared galaxy (LIRGs), especially ultraluminous infrared galaxies (ULIRGs). For example, the star formation rate (SFR) in our Milky Way is $\sim 1 M_\odot$/yr, however, SFR in the starburst galaxy NGC 1068 can be as high

as $\sim 40 M_{\odot}$/yr (Ackermann et al., 2012), and the ULIRGs Arp 220 has a even higher SFR $\sim 200 M_{\odot}$/yr (Peng et al., 2016). Thus the starburst activity will consume the available interstellar gas reservoir, where the stars are forming, over a timespan that is much shorter than the age of the galaxy. As such, starburst is a phase of galaxy's evolution, typically lasts a short period of a galaxy's history. Normal star-forming galaxies are common in the universe today, while the starburst galaxies should be common in early universe. In addition, the high SFR of a starburst is usually accompanied by much denser gas, resulting that cosmic rays accelerated in this extremely dusty region are expected to "die" mostly in collisions rather than escape in normal galaxies (e.g., Lacki et al., 2011). This situation has the maximum efficiency to emit gamma rays dominantly via π^0 decay, so the starburst galaxies are "guaranteed" gamma-ray sources (e.g., Paglione et al., 1996; Blom et al., 1999; Domingo-Santamaría & Torres, 2005; Persic et al., 2008; de Cea del Pozo et al., 2009; Rephaeli et al., 2010), and offer unique insight into the global behavior of cosmic rays over a wide range of galaxy types and star-formation rates..

1.2.2 Supernovae as Nucleosynthesis Sites

Supernovae are explosions with enormous amount of energy. In Type Ia events, a majority of the energy is used for heavy elements nucleosynthesis and the ejecta expansion, while in core collapse supernovae, neutrino emission brings away most of the energy.

Supernova nucleosynthesis is the process that fuses lighter elements carbon and oxygen during explosion to create heavier elements mainly with atomic number = 12-28 (from magnesium to nickel) (e.g., Woosley et al., 2002; Clayton, 2003; Janka et al., 2007) . Both stable nuclei and radioactive isotopes are produced during the nucleosynthesis. Measurement of the characteristic gamma-rays from these isotopes provides a useful and complementary mean of the cosmic nucleosynthesis study.

Gamma-ray Line Astronomy Gamma-ray line astronomy is the study of cosmic radioactivities in gamma ray emissions, capable to probe supernova nucleosynthesis in the nearby universe. This subject was founded with the important paper of Clayton et al. (1969). That paper suggested that supernovae produce ^{56}Ni during explosion and thus supernovae in local group galaxies should be detectable with the characteristic gamma rays from the radioactive decay of ^{56}Ni and its daughter nuclei ^{56}Co. In addition, Colgate & McKee (1969) indicated that the light curves of supernovae should be powered by the radioactive decay series of $^{56}\mathrm{Ni} \rightarrow {}^{56}\mathrm{Co} \rightarrow {}^{56}\mathrm{Fe}$. These theories were directly proved in early 1990s when the SN1987A was observed in gamma rays.

SN1987A SN1987A was a core collapse supernova in the Large Magellanic Cloud with a distance of ~ 51 kpc and was the nearest observed supernova since SN1604. The characteristic gamma ray lines from ^{56}Ni decay series were observed by gamma ray spectrometer on the SMM, the Gamma-Ray Imaging Spectrometer (GRIS) on the balloon experiments, and OSSE on the CGRO (Matz et al., 1988; Tueller et al., 1990; Kurfess et al., 1992), providing the most convincing evidence of the supernovae nucleosynthesis theories.

1.2.2.1 Type Ia Supernovae

Type Ia supernovae are end points of stellar binary evolution, acting as important distance indicators for cosmology (e.g., Phillips, 1993; Riess et al., 1998), nucleosynthesis sites of heavy elements (e.g., Clayton, 2003), cosmic-ray accelerators (e.g., Helder et al., 2009), and sources of kinetic energy in galaxy evolution (e.g., Powell et al., 2011).

Progenitors The progenitor nature of a SNIa still remains a mystery. Two competing progenitor scenarios have long been considered. In the single degenerate (SD) scenario, a carbon-oxygen white dwarf (WD) accretes mass from a companion star (a main sequence star, a subgiant, a helium star, or a red giant) (Whelan & Iben, 1973). In the double degenerate (DD) scenario, two WDs merge to explode, losing energy and angular momentum

to gravitational waves (Iben & Tutukov, 1984; Webbink, 1984). Additionally, the basic nuclear burning mechanism is still under debate: the ignited flame propagates subsonically in deflagration model, while it propagates supersonically as a shock wave in detonation. SNIa progenitor has not been detected up to now (e.g., Maoz & Mannucci, 2008), therefore neither the SD nor the DD scenarios can be determined observationally.

Nucleosynthesis and Light Curve Due to the nuclear statistical equilibrium, with equal numbers of protons and neutrons, the dominant nucleosynthesis product of a SNIa is believed to be the "double magic" radioactive nuclei ^{56}Ni (Clifford & Tayler, 1965). Thus the gamma ray lines from radioactive decay $^{56}\mathrm{Ni}\xrightarrow{8.8\mathrm{days}}{}^{56}\mathrm{Co}\xrightarrow{111.3\mathrm{days}}{}^{56}\mathrm{Fe}$ are expected to be seen in a Type Ia event. Current SNIa scenarios (such as sub-Chandrasekhar, deflagration, delayed detonations, and other models) can produce ^{56}Ni mass ranging from 0.1 to 1 solar mass. Therefore, SNIa's light curve is powered by the ^{56}Ni radioactive decay in gamma-rays. The typical SNIa light curve reaches maximum in the B band after around 15 days (Hayden et al. 2010), roughly the average diffusion time of the photons produced by the decay of ^{56}Ni in the ejecta. In the I and redder bands, a second maximum is also observed between 20 to 30 days after the B band peak (e.g., Kasen, 2006). After the peak, the light curve decays exponentially with a break at $\sim$100 days after explosion. The SNIa peak is mainly due to ^{56}Ni decay while the late time luminosity is powered by ^{56}Co. Moreover, Type Ia supernovae have similar absolute luminosity profiles related to the ^{56}Ni mass synthesized, and their light curves variations can be corrected to standard candle value to measure cosmological distance (Phillips, 1993). This measurement of distant SNIa reveals that our universe is in accelerating expansion (Perlmutter et al., 1999).

SN 2014J SN2014J was a recent closest Type Ia supernova discovered, happening in M82 with a distance of $\sim$ 3.5Mpc. INTEGRAL detected the characteristic gamma-ray lines of the ^{56}Ni radioactive decay chain. This first time line detection in a SNIa supported the theory

that large amount of ^{56}Ni is produced through the nucleosynthesis of Type Ia event (Diehl et al., 2014; Churazov et al., 2015). Moreover the claimed early time ($\sim$ 20 days) observation of the ^{56}Ni lines after the explosion suggested a surface distribution of ^{56}Ni synthesized (Diehl et al., 2014, 2015).

1.3 Dissertation Outline

Both the high energy gamma-rays from starburst galaxies (GeV range and above) and the low energy gamma lines from SNIa (MeV range and below) are closely-related with supernova explosions. The former come indirectly through the interactions between the ISM and cosmic-rays accelerated by supernova through the diffusive shock acceleration, while the latter are emitted directly from the radioactive decay of the iron-group elements (dominant product ^{56}Ni) which are generated in the ejecta of a supernova. Thus the following dissertation details my research exploring the indirect and direct way of how a supernova produce gamma-rays.

Each chapter has a separate introduction that outlines more specific background to that particular study. Chapter. 2 presents my research in cosmic-ray induced pionic gamma-ray emissions from starburst galaxies. In this study, supernovae work as cosmic ray accelerators inside the starbursts for gamma ray emissions at GeV energy range and above. Chapter. 3 will show my work about how to use current gamma ray detectors Fermi/GBM and Swift/ BAT to monitor a future Galactic SNIa and get alarmed. Here, the gamma ray signals are line emissions directly coming from the radioactive decay of ^{56}Ni and ^{56}Co synthesized during the Type Ia explosion. Finally Chapter. 4 will summarize my current preliminary work as well as future efforts in starburst galaxies and Type Ia supernovae.

Chapter 2

Are Starburst Galaxies proton calorimeters?

2.1 Abstract

Several starburst galaxies have been observed in the GeV and TeV bands. In these dense environments, gamma-ray emission should be dominated by cosmic-ray interactions with the interstellar medium ($p_{\rm cr}p_{\rm ism} \rightarrow \pi^0 \rightarrow \gamma\gamma$). Indeed, starbursts may act as proton "calorimeters" where a substantial fraction of cosmic-ray energy input is emitted in gamma rays. Here we build a one-zone, "thick-target" model implementing calorimetry and placing a firm upper bound on gamma-ray emission from cosmic-ray interactions. The model assumes that cosmic rays are accelerated by supernovae (SNe), and all suffer nuclear interactions rather than escape. Our model has only two free parameters: the cosmic-ray proton acceleration energy per supernova $\epsilon_{\rm cr}$, and the proton injection spectral index s. We calculate the pionic gamma-ray emission from 10 MeV to 10 TeV, and derive thick-target parameters for six galaxies with *Fermi*, *H.E.S.S.*, and/or *VERITAS* data. Our model provides good fits for the M82 and NGC 253, and yields $\epsilon_{\rm cr}$ and s values suggesting that supernova cosmic-ray acceleration is similar in starbursts and in our Galaxy. We find that these starbursts are indeed nearly if not fully proton calorimeters. For NGC 4945 and NGC 1068, the models are consistent with calorimetry but are less well-constrained due to the lack of TeV data. However, the Circinus galaxy and the ultraluminous infrared galaxy Arp 220 exceed our pionic upper-limit; possible explanations are discussed.

This chapter was published in the Monthly Notices of the Royal Astronomical Society as Wang, X., & Fields, B. 2018, MNRAS, 474, 4073

2.2 Introduction

Cosmic rays (CRs) are accelerated by supernovae (e.g., Baade & Zwicky, 1934; Ginzburg & Syrovatskii, 1964; Ackermann et al., 2013), and thus cosmic-ray production is an inevitable consequence of star formation. As CRs propagate in the interstellar medium (ISM), inelastic collisions between CR and interstellar nuclei–both dominantly protons–lead to gamma-ray production via π^0 decay: $p_{\rm cr}p_{\rm ism} \rightarrow \pi^0 \rightarrow \gamma\gamma$ (Stecker, 1971; Dermer, 1986). This process occurs not only in the Milky Way, but also in other star-forming galaxies (e.g., Dermer, 1986; Strong et al., 1976; Lichti et al., 1978; Pavlidou & Fields, 2001; Stecker & Venters, 2011; Abdo et al., 2009; Fields et al., 2010; Strong et al., 2010). Compared with normal star-forming galaxies like Milky Way, starbursts and ultraluminous infrared galaxies (ULIRGs, the very extreme starbursts) have exceptionally high star-formation rates and harbor regions of very dense gas. Thus cosmic rays accelerated in starbursts are expected to be lost due to interaction rather than escape, whereas normal star-forming galaxies are in the opposite regime. In the limit where all of the CR nuclei interact with ISM rather than escape, a large fraction of initial proton energy is emitted as gamma rays, making such a galaxy a "proton calorimeter" (e.g., Pohl, 1993, 1994; Lacki et al., 2011; Abramowski et al., 2012).[1] This situation has the maximum efficiency to convert supernova blast energy into gamma rays. Therefore the starbursts galaxies were anticipated to be detected as gamma-ray sources (e.g., Paglione et al., 1996; Blom et al., 1999; Domingo-Santamaría & Torres, 2005; Persic et al., 2008; de Cea del Pozo et al., 2009; Rephaeli et al., 2010).

Fermi LAT is the first gamma-ray telescope to observe the starburst galaxies, and is also the first one to study external star-forming galaxies as a population. Three of the *Fermi* detections are normal star-forming galaxies: the Large Magellanic Cloud (LMC Abdo et al., 2010a), the Small Magellanic Cloud (SMC Abdo et al., 2010b), and M31 (Abdo et al.,

[1] A closely analogous concept is cosmic-ray electron calorimetry, as suggested observationally by, e.g., the far infrared–radio correlation (e.g., Voelk, 1989).

2010c). Five additional *Fermi* detections are starburst galaxies: M82 and NGC 253 (Abdo et al., 2010d), NGC 4945 and NGC 1068 (Nolan et al., 2012), as well as the Circinus galaxy (Hayashida et al., 2013). The two nearest and brightest starbursts, M82 and NGC 253, are also detected at TeV energies by *VERITAS* (Acciari et al., 2009) and *H.E.S.S.* (Acero et al., 2009; Abramowski et al., 2012), respectively. Peng et al. (2016) and Griffin et al. (2016) recently reported *Fermi* detections of the ULIRG Arp 220. Star-forming galaxies represent a new gamma-ray source class, and offer unique insight into the global behavior of cosmic rays over a wide range of galaxy types and star-formation rates.

Various models have been built for starbursts to study the multi-frequency emissions from radio to γ-rays, considering both hadronic and leptonic processed (e.g., synchrotron radiation, inverse Compton scattering (IC), pion production). For example, Blom et al. (1999), Persic et al. (2008), de Cea del Pozo et al. (2009), Lacki et al. (2011), Lacki et al. (2014), Paglione & Abrahams (2012), Yoast-Hull et al. (2013) give their predictions of gamma-radiation from M82, while NGC 253 are anticipated to be observed in GeV-TeV range by Paglione et al. (1996), Domingo-Santamaría & Torres (2005), Rephaeli et al. (2010), Lacki et al. (2011); Lacki et al. (2014), Paglione & Abrahams (2012), Yoast-Hull et al. (2014). Recent observations and current theoretical models of starbursts are also reviewed by Ohm (2016). Many-but not all-of these models predict that hadronic processes dominate above a few GeV. In this paper, our aim is to calculate self-consistently the pionic emission from starbursts in a closed box, and to use starburst data to test this calorimetric scenario. By construction, our more focused model is economical and thus easy to test: it contains only two parameters, the cosmic-ray acceleration energy per supernova $\epsilon_{\rm cr}$, and the cosmic-ray injection index s. Some early results from our calculations were summarized in Wang & Fields (2014) and Wang & Fields (2016).

In this paper, we define a *proton calorimeter* to be a system in which cosmic-ray pionic losses dominate over other losses including escape, advection, and diffusion. Such a system is in the "thick-target" regime of cosmic-ray propagation, and a substantial fraction of the

energy injected into cosmic-ray protons energy is ultimately emitted as pionic gamma-ray photons. The calorimetric efficiency (eq. 2.18) is a measure of gamma-ray energy output to the cosmic-ray energy input.

The next section shows the assumptions, important expressions and physics of our thick-target model. § 2.4 presented the results calculated from our model when applying to five observed starbursts galaxies and the ULIRG Arp 220. In § 2.5, further discussions and conclusions are given.

2.3 The Thick-Target/Calorimetric Model

To calculate the hadronic gamma-ray output in our model, we first characterize the cosmic-ray sources and their thick-target propagation. We then use the propagated cosmic-ray flux to arrive at hadronic gamma-ray emission. The calculation in this session adopts GeV as the energy unit.

2.3.1 Model Assumptions

We describe the production and propagation of cosmic rays in a one-zone, thick-target "closed-box" model. The physical processes in our model are CR ion acceleration by SNe, followed by pion production through the interaction between the CRs and the ISM. The resulting neutral pion decay is responsible for the existing gamma-rays. The basic assumptions are:

1. cosmic-rays and ISM gas are both spatially homogeneous;

2. cosmic rays are accelerated by supernovae (SNe) with acceleration energy per SN $\epsilon_{\rm cr}$;

3. the injected cosmic-ray/proton spectrum is a power law in momentum, of spectral index s in GeV and TeV energy range;

4. all the cosmic rays will interact with ISM, i.e. the escape rate of protons is zero, *advection and diffusion loss are also ignored here*; and

5. among the gamma-ray production mechanisms, pion production and decay dominates.

Our thick-target model places a firm upper-limit on the hadronic (pionic) gamma-ray emissions from starbursts, by including only losses due to particle interactions (collisions and scattering). Other work has argued that in starburst regions, the dense gas, high supernova density and relatively hard gamma ray spectrum point to diffusion and advection losses being subdominant (e.g., Lacki & Thompson, 2010, 2013; Torres et al., 2012). We concur, and in Appendix 2.6.3, we show that in starbursts, the interaction time is much sorter than the diffusion and advection times. We thus omit these effects in our model for an upper-limit calculation. If the advection and diffusion losses were included, the actual calorimetric efficiencies are reduced, which may explain the difference in the starbursts' calorimetric efficiencies obtained with our thick-target model in § 2.4 (due to the different values of $\tau_{\rm diff}$ and $\tau_{\rm adv}$ in each starburst). We also neglect reacceleration of cosmic rays (Strong et al., 2007) inside starbursts, which merits a study in its own right. [2]

The thick-target hadronic model presented here neglects primary electron effects (inverse Compton, bremsstrahlung radiation) and secondary electron effects in gamma-ray emission. This assumption is consistent with *NuSTAR*'s upper limits on NGC 253 in the 7-20 keV band, which disfavor leptonic processes dominating in the GeV and TeV energy range (Wik et al., 2014). In addition, Strong et al. (2010) found pionic emission dominates over both primary and secondary electron emission by factors > 2 among the total Galactic luminosity in GeV range. This implies that in starbursts where cosmic ray proton losses dominate over escape, pionic emission should be even more dominant over leptonic. By assuming the CR protons lose energy continuously through the propagation inside the starbursts, the effect of

[2]Note that reacceleration due to supernova shocks would be an additional way to transfer supernova blast energy to cosmic rays, and so would amount to a component of calorimetry. If other shock contribute to reacceleration, it would give an apparent boost to the calorimetric efficiency.

secondary recoil protons (the ISM protons after *pp* collisions) appears only via the elastic scattering energy loss term, and not as a proton source term. While these effects are not large, they would only boost the gamma-ray production and lead to an even tighter limit to the gamma-ray emission.

We also ignore the effect of intergalactic absorption of the high-energy gamma rays via photon-pair production ($\gamma\gamma \to e^+e^-$) in collision with background starlight emission (e.g., Salamon & Stecker, 1998; Stecker et al., 2012) and in collision with the infrared field of the starbursts (Lacki & Thompson, 2013). The former effect will bring a steepening of the gamma-ray spectrum at high energy, but this effect is very small for the starbursts we study, which are all very nearby. The later effect can be substantial for gamma-ray energies above a few TeV, but is negligible in the GeV energy range that is our focus.

2.3.2 Cosmic-Ray Source and Propagation

The equations for cosmic-ray transport (e.g., Longair, 1981; Strong et al., 2007; Meneguzzi et al., 1971; Fields et al., 1994) can be written as

$$\partial_t N_E = \partial_E(b_E N_E) - \frac{1}{\tau_E} N_E + q_E \ + \text{advection} + \text{diffusion} \ . \tag{2.1}$$

Here and throughout, E denotes *kinetic* energy per nucleon, and $N_E \ dE$ is the number density of cosmic rays with kinetic energy $\in (E, E + dE)$. The cosmic-ray number flux density is thus $\phi(E) = v_E N_E$, with v_E the velocity at E. In eq. (2.1), τ_E is the lifetime of cosmic ray against escape, q_E is the injected cosmic ray spectrum, $b_E = -dE/dt$ is the rate of energy loss (per nucleon).

We now drastically simplify the problem, adopting the closed-box, thick-target, steady-state limit corresponding to the discussion in §2.3.1. That is, we focus on a single uniform zone, in which cosmic rays are accelerated and then propagate until lost due to their interactions, and in which acceleration and losses are driven to an equilibrium $\partial_t N_E = 0$ over the

energy loss timescale $\tau_{\rm loss} = \int dE/b \sim E/b$. We thus neglect escape, so that $1/\tau_E = 0$, and spatial uniformity implies that the gradient-driven advection and diffusion terms are zero.

The closed-box, steady-state solution to eq. (2.1) gives a proton flux density

$$\phi_{\rm p}\left(E\right) = vN_E = \frac{v_{\rm p}}{b\left(n_{\rm gas}, E\right)} \int_E^\infty dE' q_{\rm E}\left(E'\right) \tag{2.2}$$

We see that in this simple model, the cosmic-ray flux depends only the cosmic ray source function q_E and energy loss rate b.

Since cosmic rays accelerated by the supernovae in our model, energy conservation implies

$$L_{\rm cr} = \frac{dE_{\rm cr}}{dt} = E_{\rm sn} f_{\rm cr} R_{\rm sn} = \epsilon_{\rm cr} R_{\rm sn} = V \int_{E_{\rm min}}^\infty E \frac{dq}{dp} dp \tag{2.3}$$

where $L_{\rm cr}$ is the injected cosmic ray luminosity, V is the volume of the galaxy where cosmic rays are produced, $E_{\rm min}$ is the minimum kinetic energy of injected protons that can be accelerated. $E_{\rm sn}$ is the total baryonic energy released by one SN explosion. Some fraction $f_{\rm cr}$ of this explosion energy goes to accelerate cosmic rays, and this leads to the other free parameter in our model: $\epsilon_{\rm cr} = E_{\rm sn} f_{\rm cr}$the cosmic-ray proton acceleration energy per supernova. $R_{\rm sn}$ is the SN rate, which can be converted from the star formation rate (SFR) ψ by $R_{\rm sn}/\psi \sim 0.00914 M_\odot^{-1}$ (Lien & Fields, 2009).

Following the simplest (i.e., test particle) expectations of diffusive shock acceleration (e.g., Krymskii, 1977; Bell, 1978; Blandford & Ostriker, 1978) we assume the injected cosmic ray spectrum (emissivity) is a power law in momentum:

$$q_{\rm p} = \frac{dN}{dV dt dp} = \frac{dq}{dp} = \frac{q_0}{I} p^{-s} \tag{2.4}$$

where $q_0 = L_{\rm cr}/V$ is the cosmic ray luminosity density, I is the normalization factor, s, the proton spectral injection index, is a free parameter in the model (> 2.0). See §2.3.4 for more discussion of this assumption.

Finally we can get the accelerated proton spectrum:

$$\phi_{\rm p}\left(E\right) = \frac{q_0 v_{\rm p}}{Ib(n_{\rm gas}, E)} \frac{(p_{\rm p})^{1-s}}{s-1} \tag{2.5}$$

where $p_{\rm p}$ is proton's momentum, and I is a number that is determined by $E_{\rm min}$: $I = I\left(E_{\rm min}\right) = \int_{E_{\rm min}}^{\infty} E(E+m_{\rm p}) p_{\rm p}^{-s-1} dE$, $m_{\rm p}$ is the mass of proton.

2.3.3 Pionic Emission From Thick-Target Galaxies: the Calorimetric Model

Our notation and approach follows that of Dermer (1986). From the accelerated proton spectrum, we can get the pionic spectrum (in the lab frame) through the interaction $p_{\rm cr} p_{\rm ism} \rightarrow \pi^0 \rightarrow \gamma\gamma$:

$$\frac{dq_\pi(E_\pi)}{dE_\pi} = n_{\rm gas} \int_{E_{\rm p}^{\rm threshold}}^{\infty} dE_{\rm p} \phi_{\rm p}(E_{\rm p}) \frac{d\sigma_\pi(E_\pi, E_{\rm p})}{dE_\pi} \tag{2.6}$$

In turn, the gamma-ray spectrum is

$$\begin{aligned} & \frac{dq_\gamma(E_\gamma)}{dE_\gamma} [\text{photons}/(\text{cm}^3 - \text{s} - \text{GeV})] \\ = \; & 2 \int_{E_\gamma + (m_\pi^2/4E_\gamma) - m_\pi}^{\infty} dE_\pi \frac{dq_\pi(E_\pi)/dE_\pi}{((E_\pi + m_\pi)^2 - m_\pi^2)^{1/2}} \end{aligned} \tag{2.7}$$

where $E_p^{\rm threshold}(E_\pi)$ is the threshold proton kinetic energy that can produce a pion with energy E_π, and m_π is the π^0 mass. The differential cross section $d\sigma_\pi(E_p, E_\pi)/dE_\pi$ for the production of a π^0 with energy E_π can be written as $d\sigma_\pi(E_p, E_\pi)/dE_\pi = \langle \zeta \sigma_\pi(E_{\rm p}) \rangle dN(E_{\rm p}, E_\pi)/dE_\pi$. Here $\langle \zeta \sigma_\pi(E_{\rm p}) \rangle$ is the inclusive cross section for the reaction $p_{\rm cr} p_{\rm ism} \rightarrow \pi^0 \rightarrow \gamma\gamma$.

Our model self-consistently calculates the inelastic energy loss from cross-section $\langle \zeta \sigma_\pi(T_{\rm p}) \rangle$. We use the Dermer (1986) for the inclusive cross-section $\langle \zeta \sigma_\pi(E_{\rm p}) \rangle$, and thus we can get the

inelastic energy loss rate consistently (assuming the loss is approximated to be continuous):

$$b_{\rm inelastic} = 3 n_{\rm gas} v_{\rm p} \langle \zeta \sigma_\pi(E_{\rm p}) \rangle \int_0^{E_{\rm p}} E_\pi dN(E_p, E_\pi)/dE_\pi dE_\pi. \tag{2.8}$$

The crucial factor of 3 here comes from assuming the inclusive cross sections for $p_{\rm cr} p_{\rm ism} \rightarrow \pi^{\pm}$+anything are the same as π^0, i.e., the production rates for (π^-, π^0, π^+) are approximately the same. This factor of 3 has a direct impact on the gamma-ray production efficiency: the gamma energy output per energy into CRs above pionic threshold would be 1/3 if the inelastic losses were the only ones.

We also include the energy loss contributions due to nuclear elastic scattering (Gould, 1982) and ionization (Ginzburg & Syrovatskii, 1964): $b(n_{\rm gas}, E) = b_{\rm inelastic} + b_{\rm elastic} + b_{\rm ioniz}$, with rates given in the Appendix 2.6.2. These two terms also affect the gamma-ray production efficiency: ionization loss is only important at low energies, but the elastic scattering is important at all energies and in general is comparable to inelastic. Thus elastic losses are the more important to lower the CR efficiency.

The function $dN(E_{\rm p}, E_\pi)/dT_\pi$ encodes the distribution of pion energies at each proton energy. We adopt Dermer (1986)'s approach, combining Stecker's isobaric model (model S, Stecker, 1970) together with Stephens and Badhwar's scaling model (model SB, Stephens & Badhwar, 1981): for $E_{\rm p} < 3$GeV, model S is used; while model SB is adopted for $E_{\rm p} > 7$GeV; for 3GeV $< E_{\rm p} <$ 7GeV, model S and model SB is linearly connected to be used.

Collecting these results gives the emissivity

$$\begin{aligned} \frac{dq_\gamma}{dE_\gamma} &= \frac{dN_\gamma}{dV dE_\gamma dt} \\ &= \frac{\epsilon_{\rm cr} R_{\rm sn}}{V I(E_{\rm min})} I_0(E_\gamma, s) \end{aligned} \tag{2.9}$$

where $I_0(E_\gamma, s)$ is a dimensionless integration:

$$\begin{aligned} I_0(E_\gamma, s) &= \int_{E_\gamma + {m_\pi}^2/(4E_\gamma) - m_\pi}^{\infty} \frac{2dE_\pi}{p_\pi} \int_{E_p^{\rm threshold}}^{\infty} dE_{\rm p} \\ &\quad \times \frac{\sigma_\pi\left(E_{\rm p}\right)}{b(E_{\rm p})} \frac{dN\left(E_\pi, T_{\rm p}\right)}{d\left(E_\pi\right)} n_{\rm gas} v_{\rm p} \frac{p_{\rm p}^{1-s}}{s-1} \end{aligned} \tag{2.10}$$

Notice that the energy loss rate scales with gas density: $b \propto n_{\rm gas}$ (see eqs. 2.8, 2.23, and 2.24). This exactly cancels the gas density in the numerator of eq. (2.10), and thus *the gamma-ray emission is independent of the gas density for the thick-target model.* This is characteristic of calorimetry. Note further that the ratio $b/n_{\rm gas}$ depends only on the cross sections in the loss interactions. This means that I_0 and thus the gamma-ray emission depends only on the ratio of cross sections (inelastic pion production to total losses).

To account for the contribution from particle interactions involving nuclei with atomic weights $A > 1$ in both CRs and ISM, a nuclear enhancement factor of $\mathcal{A} = 0.59$ is included in the calculation. In the case of calorimetry, Appendix 2.6.4 shows that the "nuclear enhancement" $\mathcal{A} = 1/\langle A \rangle$ and so $\mathcal{A} < 1$, this arises because additional nuclei species must share a fixed CR injection energy budget.

Let d to be the distance of the source, γ-ray flux can be expressed as:

$$E_\gamma^2 F_\gamma = E_\gamma^2 \frac{dN_\gamma}{dE_\gamma dA dt} = \mathcal{A} \frac{\epsilon_{\rm cr} R_{\rm sn}}{I(E_{\rm min})} E_\gamma^2 \frac{1}{4\pi d^2} I_0(E_\gamma, s) \tag{2.11}$$

and the gamma-ray energy luminosity from the galaxy is:

$$\begin{aligned} L_\gamma &= \frac{dE_\gamma}{dt} = \int E_\gamma \frac{dq_\gamma}{dE_\gamma} dE_\gamma dV \\ &= \mathcal{A} \frac{\epsilon_{\rm cr} R_{\rm sn}}{I(E_{\rm min})} \int dE_\gamma E_\gamma I_0(E_\gamma, s) \end{aligned} \tag{2.12}$$

Note that the volume integration in our one-zone model cancels the factor in the emissivity q_γ (eq. 2.9), leading to the final result that is independent of volume. We see therefore that in

our calorimetric limit, the ratio $L_\gamma/R_{\rm SN}$ depends on the supernova acceleration parameters $\epsilon_{\rm cr}$ and s, as well as I_0 that depends only on cross sections. It is *independent* of the gas density, mass, and volume in this calorimetric model.

The luminosity $L_\gamma \propto R_{\rm sn}$, and while the SN rate is usually not measured directly, its is proportional to the star-formation rate of a galaxy. Therefore we can get

$$\frac{L_\gamma}{\psi} = \frac{0.00914 M_\odot^{-1} \mathcal{A} \epsilon_{\rm cr}}{I(E_{\rm min})} \int dE_\gamma E_\gamma I_0(E_\gamma, s) \tag{2.13}$$

that is a constant only depend on CR proton spectral index s in a calorimetric limit ($\epsilon_{\rm cr} =$ 0.3 foe, with 1 foe $\equiv 10^{51}$erg $\equiv$ 1 Bethe). L_γ/ψ is observable, so it can be used to investigate cosmic-ray properties in a calorimetric system.

We can see that, our model's gamma-radiation results only depend on two parameters: cosmic-ray proton acceleration energy per supernova $\epsilon_{\rm cr}$ (direct proportionality) and the proton injection spectral index s. We only need to vary the two parameters $\epsilon_{\rm cr}$ and s to find the best fit to the model (§2.3.4). An order of magnitude calculation of our model in Appendix 2.6.1 helps to give intuition for the final results and frame key physical issues.

2.3.4 Projectile CR Proton Index And Supernova Acceleration Energy/Efficiency

In our model, each supernova accelerates cosmic rays, which are lost via interactions with interstellar gas, and the π^0 from these interactions give rise to gamma rays. Thus the gamma-ray output ultimately depends on the CR properties of the supernova sources: the proton injection index s and CR acceleration energy per SN are the only two parameters our model. Milky Way supernova remnant (SNR) gamma-ray data together with supernova acceleration theories can give both observational and theoretical insight into the parameters we have derived for starbursts in the previous section.

Diffusive shock acceleration naturally yields a relativistic electron and ion spectra that

are each power laws in momentum, in the test-particle limit that neglects feedback from the accelerated cosmic rays onto the shock (e.g., Krymskii, 1977; Bell, 1978; Blandford & Ostriker, 1978). Although the resulting non-linear correction to diffusive shock acceleration results in a concave proton spectrum with a steeper spectrum index at high energy (e.g., Morlino & Blasi, 2016; Kang et al., 2013; Slane et al., 2014), the concavity is expected to be rather mild for a SN with particle acceleration efficiency to be at the order of ~ 10 percent (Morlino & Blasi, 2016).

For a strong shock in monatomic gas, diffusive shock acceleration gives $s \to 2.0$. In GeV and TeV energy range, the combination of observed CR flux at Earth ($\propto E^{-2.75}$) and galactic CR transportation models (e.g., Strong & Moskalenko, 1998; Evoli et al., 2008; Blasi & Amato, 2012) implies the index s to be $2.2 - 2.4$ (Caprioli, 2012). Other theories give different values of the source proton index value in SNR, for example, Fermi Collaboration (2013) gives 2.5 below 6.5 GeV and 2.8 above, for the interstellar cosmic-ray proton index; Morlino & Caprioli (2012)'s model for SNR Tycho gives $s = 2.2$. Gamma-ray emission from SNRs probes s directly (if pions dominate), and available measurements give s spanning a considerable range. *Fermi* LAT measurement of Galactic SNRs give $s = 1.53$ to 3.58 with the weighted average to be 2.39, while the spread of the index is about 1 (Acero et al., 2016). Because some SNRs are dominated by IC or bremsstrahlung that contribute to flatter photon spectra than pions, the actual source proton index estimated from *Fermi* SNR measurements would be steeper than the weighted average value of s. Particularly for the SNRs W44 and IC443 with clear characteristic pion-decay gamma-spectra, the observations give the accelerated proton index s to be about 2.4 in the energy range smaller than break energy (Ackermann et al., 2013), where the projectile CRs in the galaxies mainly come from. Moreover, for TeV gamma-rays, we expect the signal is pionic and thus these index measurements can give us a fair estimate of the CR source index. The TeV data gives the index varies between 1.8-3.1 with an average value $s \sim 2.4$ (e.g., Aliu et al., 2013; H. E. S. S. Collaboration et al., 2011; Aharonian et al., 2008).

For CR acceleration energy parameter, $\epsilon_{\rm cr} = E_{\rm sn} f_{\rm cr}$, the average kinetic energy released per SN ($E_{\rm sn}$) is 10^{51}erg (Woosley & Weaver, 1995), but there exists much uncertainties in the value of SNR acceleration efficiency to CR ($\epsilon_{\rm sn}$). If SNRs are the main sites of acceleration of cosmic rays, then 3 to 30 percent of the supernova kinetic energy must end up transferred to CR protons from various theories: Fields et al. (2001) suggested that if SNRs are the dominant sources for cosmic-ray production as well as the nucleosynthesis of lithium, beryllium, and boron in the Milky Way, an acceleration efficiency of ~ 30 percent is needed; Strong et al. (2010) obtains a CR energy input efficiency per SN of $3-10$ percent; Caprioli (2012)'s study also found the acceleration efficiency saturates at around $10-30$ percent; Dermer & Powale (2013)'s results suggest that most supernova remnants accelerate cosmic rays with an efficiency of ~ 10 percent for the dissipation of kinetic energy into nonthermal cosmic rays. The observations of SNRs also give insight into CR acceleration efficiency, for example, SNR Tycho accelerates protons up to 500 TeV with an efficiency of ~ 10 percent (Morlino & Caprioli, 2012) while the hadronic scenario of SNR RCW86 concludes that the accelerated particles energy efficiency from SNR is at the level of ~ 0.07 (Lemoine-Goumard et al., 2012). We thus adopt a fiducial value $\epsilon_{\rm cr} = 10$ percent $\times\, 10^{51}$erg $= 0.1$ foe, but note that uncertainties are large; we will adopt maximum value $\epsilon_{\rm cr,max} = 0.3$ foe as implied by the Li, Be, and B nucleosynthesis results.

2.4 Model Results

The thick-target model built in § 2.3 gives proportionality relation of the differential gamma-ray emission to $\epsilon_{\rm cr}$, and from eq. 2.12, we can see that $L_\gamma / L_{\rm CR}$ is the same for every calorimetric galaxy with the same choice of source CR proton index s, therefore

$$\frac{dL_\gamma/dE_\gamma}{L_{\rm CR}} = \frac{\mathcal{A} E_\gamma dN_\gamma/dE_\gamma dt}{L_{\rm CR}} \stackrel{\rm cal}{=} E_\gamma \frac{I_0(E_\gamma, s)}{I(T_{\rm min})} {\rm GeV}^{-1} = const \tag{2.14}$$

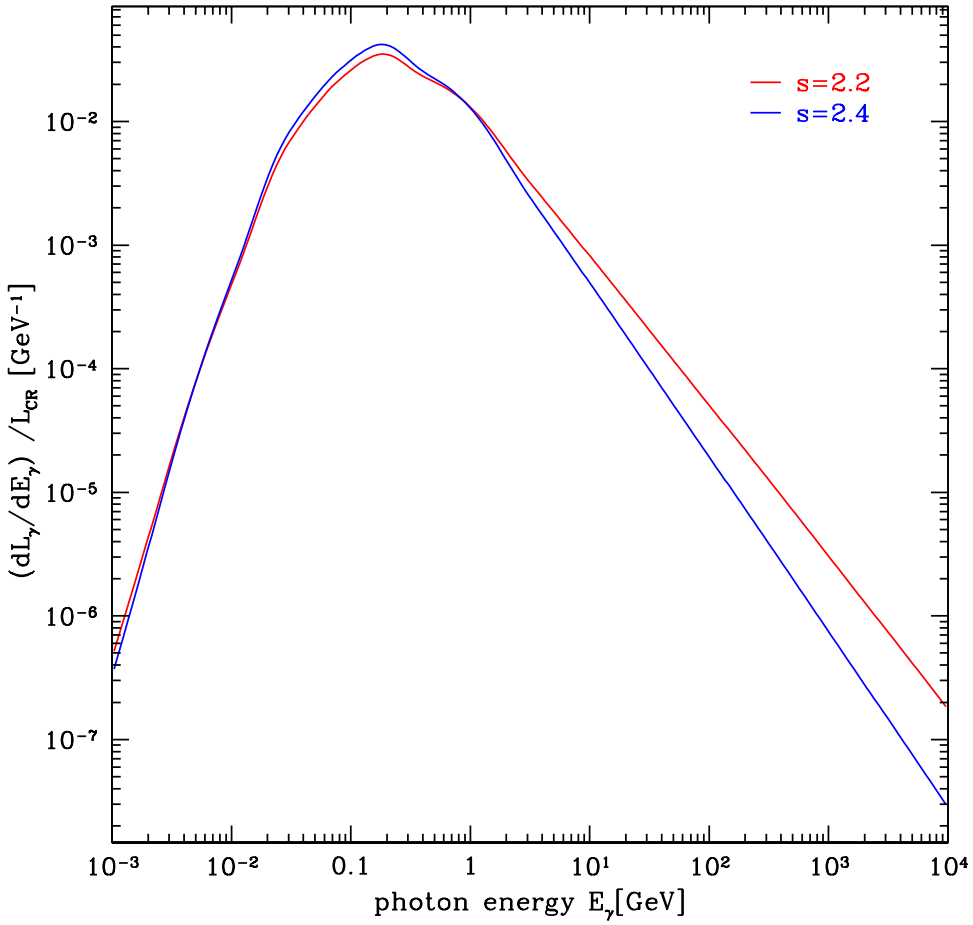

Figure 2.1: Ratio of differential gamma-ray luminosity to total CR luminosity for a calorimetric galaxy. The red line represents the result with choice of source CR index $s = 2.4$, while the blue line is for $s = 2.2$.

and the relation is shown in Fig. 2.1 with $s = 2.2$ and 2.4. Because $(dL_\gamma/dE_\gamma)/L_{\rm CR}|_s$ is the same for all calorimetric galaxies, the plot of this ratio presents the general properties of our model's results: gamma-ray emission peaks around ~ 0.15GeV and is nearly a power law at high energy. For different s, the ratios of differential gamma-ray luminosity to CR luminosity are different especially at high energy, but are always smaller than 1/3 due to energy conservation.

We now apply our model to individual starburst galaxies (§2.4.1). With their cosmic-ray parameters determined, we then compute their luminosity and evaluate their status as

calorimeters (§2.4.2).

2.4.1 Individual Starbursts

We now apply our model to five individual starbursts NGC 253, M82, NGC 4945, NGC 1068, and the Circinus galaxy, as well as the ULIRG Arp 220. The input parameters and best-fit results are listed in Table 2.1 and Table 2.2. For each galaxy we adopt an observed star-formation rate (SFR), and then calculate the pionic flux $E_\gamma^2 dN_{\pi\to\gamma\gamma}/dE_\gamma dAdt$ for each point in $(\epsilon_{\rm cr}, s)$ space. We perform χ^2 test with the observed gamma-ray data to get the best-fit model parameters:

$$\chi^2(\epsilon_{\rm cr}, s) = \sum_i \frac{(F_{\rm i} - \hat{F}_{\rm i})^2}{\sigma_{\rm i}^2} \tag{2.15}$$

where $\hat{F}_{\rm i}$ is the flux value of the data points at each photon energy $E_{\rm i}$, $F_{\rm i} = \epsilon_{\rm cr} y_{\rm i}(s)$ is our model's flux value at each $E_{\rm i}$, $\sigma_{\rm i}$ is the uncertainty of the data's flux value at each $E_{\rm i}$.

We consider injection indices in the range $s \in [2.1, 3.0]$. By maximizing the value of χ^2 at each s, we can get the best-fit values of $\epsilon_{\rm cr}$ analytically. We then compare the values of χ^2 for each s with the best-fit $\epsilon_{\rm cr}$, finally can find the best-fit value of s numerically.

From Table 2.2, we can see that the pionic gamma-ray luminosity calculated from our model agrees well with the phenomenological *Fermi* fits for the starburst galaxies M82, NGC 253, NGC 4945, NGC 1068 the Circinus galaxy, and ULIRG Arp 220.

The best-fit pionic gamma-ray spectra can be seen in Figs. 2.2 through 2.5. In left panels, the solid lines is our model's calculated differential spectral energy distribution of the five starburst galaxies with the best-fit parameters s and $\epsilon_{\rm cr}$. The red points in GeV range are *Fermi* data while blue ones in TeV range are got from *H.E.S.S* or *VERITAS*. For M82

Table 2.1: Parameters set for the starburst galaxies in Thick-Target Model.

Galaxy Name	Distance D[Mpc]	SFR ψ [$M_\odot$/yr]	SN Rate $R_{\rm SN}$ [century^{-1}]	GeV data reference	TeV data reference
M82	3.4 ± 0.9	6.3 ± 0.9	5.7 ± 0.9	Ackermann et al. (2012)	Acciari et al. (2009)
NGC 253	2.5 ± 0.5	2.9 ± 0.4	2.6 ± 0.4	Paglione & Abrahams (2012)	Abramowski et al. (2012)
NGC 4945	3.7 ± 0.8	3.5 ± 1.0	3.2 ± 0.9	Ackermann et al. (2012)	
NGC 1068	16.7 ± 3.0	38 ± 10	35 ± 9	Ackermann et al. (2012)	Aharonian et al. (2005)
Circinus	4.2 ± 0.7	2.1 ± 0.5	1.9 ± 0.5	Hayashida et al. (2013)	
Arp 220	77.0 ± 2.0	188.3 ± 10.0	172.1 ± 9.1	Peng et al. (2016)	VERITAS collaboration (2015)

Galaxy distances: Gao & Solomon (2004). Star formation rates: Ackermann et al. (2012), using Gao & Solomon (2004) total IR luminosities and Kennicutt relation (Kennicutt, 1998), except for the Circinus galaxy (Tully et al., 2009; Hayashida et al., 2013) and Arp 220 (Peng et al., 2016).
Distance uncertainties come from `http://ned.ipac.caltech.edu`. Except for the ULIRG Arp 220, the redshift-dependent distance uncertainty comes from Hubble constant error (Planck Collaboration et al., 2016) (assuming the peculiar velocity uncertainty is the same as Hubble constant uncertainty).

Table 2.2: Results for the starburst galaxies in Thick-Target Model.

Galaxy Name	CR source index $\hat{s}$	CR acceleration energy per SN $\epsilon_{\rm cr}$[foe/SN]	$L^{model}_{0.1-100\rm GeV}$ [10^{40}ergs^{-1}]	$L^{\rm Fermi}_{0.1-100\rm GeV}$ [10^{40}ergs^{-1}]	$\Gamma^{\rm Fermi}$
M82	2.275 ± 0.102	0.106 ± 0.025	1.48 ± 0.44	1.47 ± 0.14	2.25 ± 0.13
NGC 253	2.350 ± 0.037	0.116 ± 0.013	0.73 ± 0.10	0.60 ± 0.07	2.18 ± 0.09
NGC 4945	2.400 ± 0.446	$0.210(> 0.103)$	$1.64(> 0.80)$	1.17 ± 0.23	2.05 ± 0.13
NGC 1068	2.100 ± 0.617	$0.253(> 0.128)$	$13.3(> 6.7)$	15.0 ± 2.9	2.29 ± 0.19
Circinus	2.300 ± 0.486	$0.619(> 0.310)$	$2.97(> 1.48)$	2.9 ± 0.5	2.19 ± 0.12
Arp 220	2.550 ± 0.257	$0.808(> 0.404)$	$2.85(> 1.43) \times 10^2$	$(1.78 \pm 0.3) \times 10^2$	2.35 ± 0.16

Fermi gamma luminosities for the galaxies are calculated by Hayashida et al. (2013) using a power law spectral model $dN/dE \propto E^{-\Gamma}$, except for Arp 220 (Peng et al., 2016).

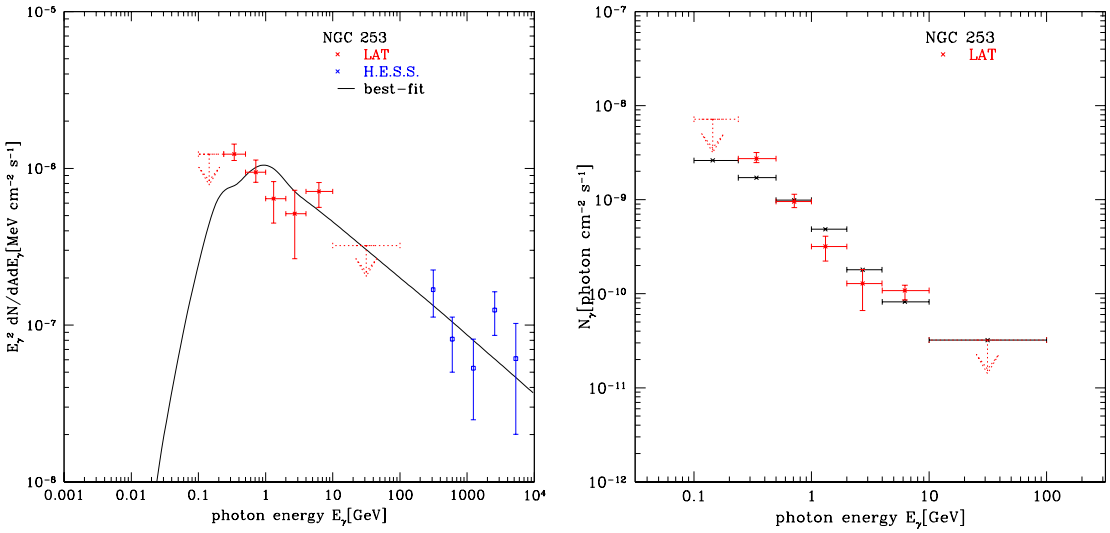

Figure 2.2: Left panel: Differential pionic gamma-ray spectrum (solid curve) for NGC 253 with the best-fit parameters: source CR index s and accelerated CR energy per SN $\epsilon_{\rm cr}$. *Fermi* points are stars (red), *H.E.S.S* points are squares (blue), black solid line is our model's best-fit to data; see Table 2.2. Right panel: Best-fit integrated pionic gamma-ray spectrum for NGC 253. Red points are *Fermi* measurement, black points are our model's best-fit results.

and NGC 253, we see that our best fit to GeV and TeV data is quite good and fairly well constrained thanks to the relatively large energy range. For NGC 1068, NGC 4945, Circinus and Arp 220, only GeV data is available and even our simple model is poorly constrained.

We note that the observed differential spectrum points are derived assuming a constant spectral index at all energies, but in our model the index varies strongly at lower energies near the "pion bump" at $m_{\pi^0}/2$. We thus plot in the right panels Figs. 2.2–2.5 the integrated photon flux $\int_{E_i^{\rm min}}^{E_i^{\rm max}} dF/dE\, dE$ over each energy bin i, whose width is spanned by the horizontal bars. This corresponds to the photon counts per energy bin, which is what *Fermi* directly measures and which is free from assumptions about spectral index. The black points are from our best-fit model, and the red points are the *Fermi* data. We see that our fits are generally good across the GeV range, including at low energies near the pion bump where the spectral index is not constant.

From Figs. 2.2–2.5, we can see that the gamma-ray spectra got from our thick-target model has the following features, as already seen in Fig. 2.1: (1) the shape only depends on

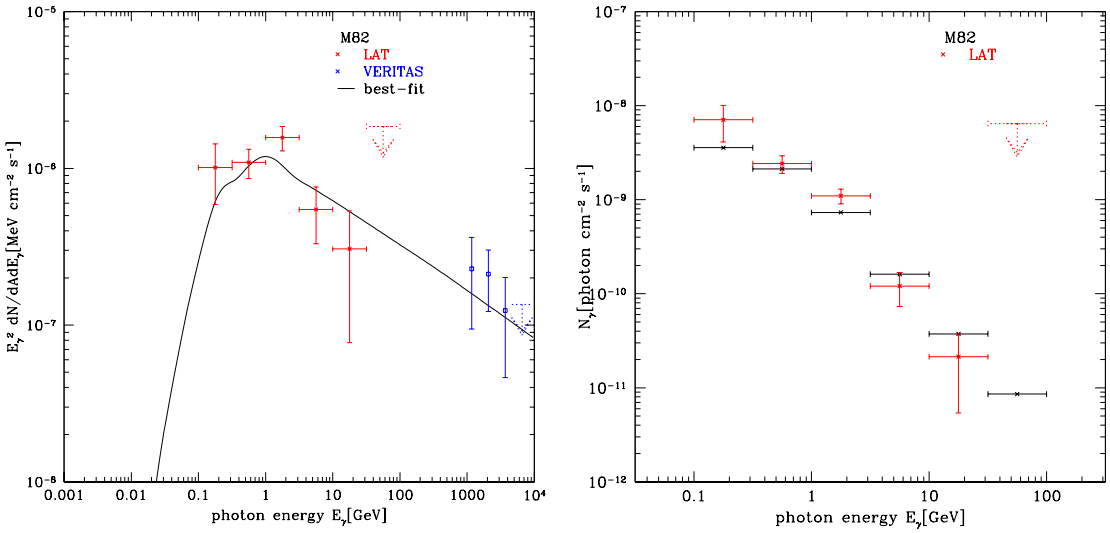

Figure 2.3: Left panel: Differential pionic gamma-ray spectrum (solid curve) for M82 with the best-fit parameters: source CR index s and accelerated CR energy per SN$\epsilon_{\rm cr}$. *Fermi* points are stars (red), *VERITAS* points are squares (blue), black solid line is our model's best-fit to data; see Table 2.2. Right panel: Best-fit integrated pionic gamma-ray spectrum for M82. Red points are *Fermi* measurement, black points are our model's best-fit results.

the injected proton spectrum; (2) the magnitude is proportional to $\epsilon_{\rm cr}$; (3) at high energies, the gamma-ray spectral index is the same as the proton injection index s; (4) in our model, the peak is due to the pion bump, which appears at $E_\gamma = m_{\pi^0} = 67.5$ MeV in plots of F_E, (Stecker, 1971; Dermer, 1986), but is shifted to ~ 1 GeV in our E^2F_E plots.

The χ^2 contour plots are shown in Fig. 2.6 with Confidence Level (CL) = (70 percent, 95 percent, 99 percent). For M82 and NGC 253, TeV data and good GeV data are available, and s and $\epsilon_{\rm cr}$ are both well-constrained. For these galaxies, $\epsilon_{\rm cr} \sim 0.1$ foe, in good agreement with canonical estimates for Milky-Way cosmic rays (Ginzburg & Syrovatskii, 1964). We see that steeper (shallower) s can be accommodated by a higher (lower) $\epsilon_{\rm cr}$. This arises physically because $\epsilon_{\rm cr}$ fixes the overall normalization, and thus to fit the high-energy data with a steeper slope requires a higher overall normalization. The resulting tension with the low-energy points limits the range of this correlation.

For the other galaxies NGC 1068, NGC 4945, Circinus and Arp 220, the lack of TeV data leaves large uncertainties in *both* s and $\epsilon_{\rm cr}$, as seen in Fig. 2.6. But Fig. 2.6 nevertheless

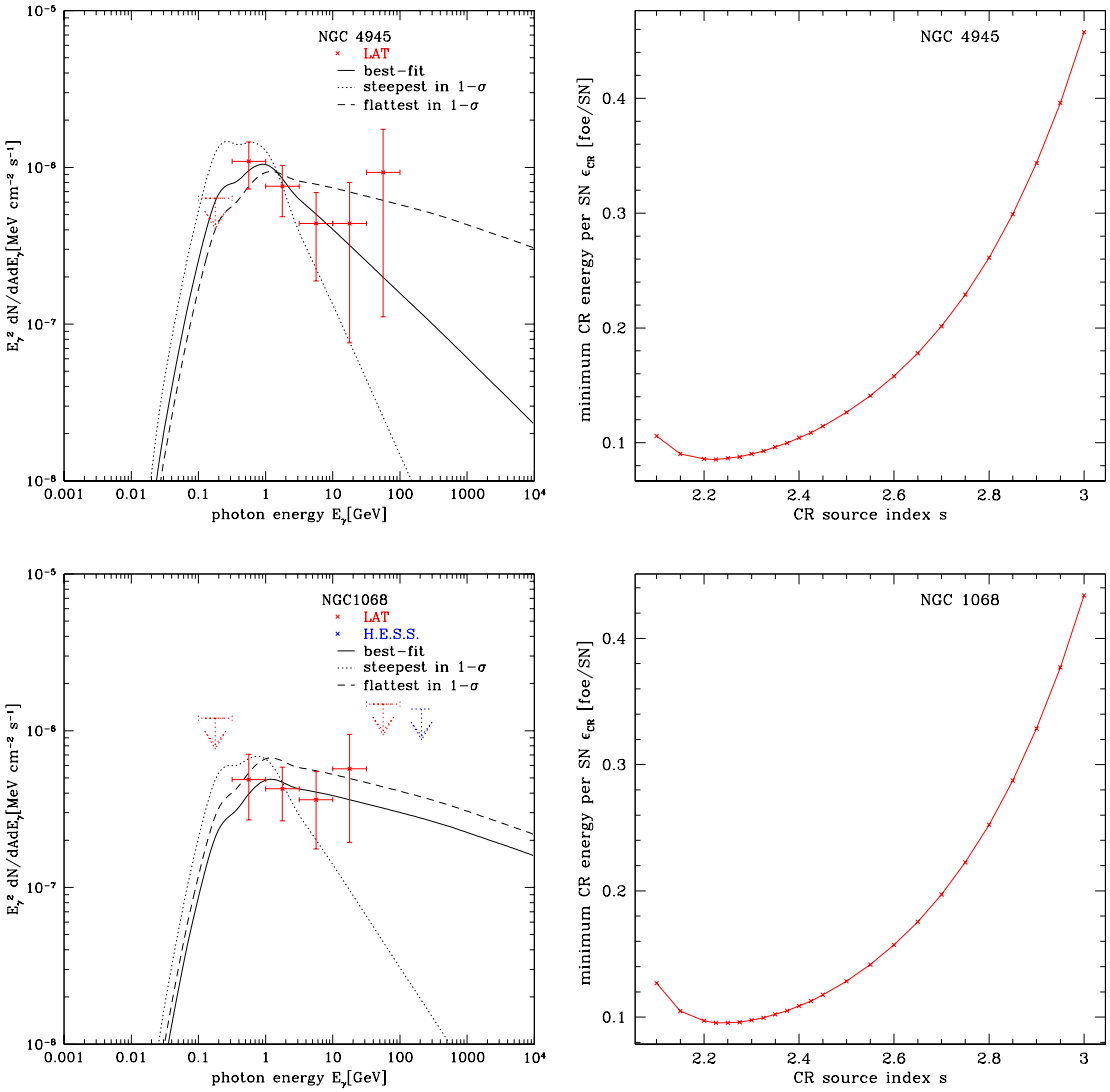

Figure 2.4: Left panel: Pionic gamma-ray spectra (solid curve) for NGC 4945 (upper) and NGC 1068 (lower) with the best-fit parameters: source CR index s and accelerated CR energy per SN $\epsilon_{\rm cr}$. *Fermi* points are stars (red), *H.E.S.S.* points are squares (blue), black solid line is our model's best-fit to data; see Table 2.2. Black dashed line is our model's flattest curve to fit the data in 1-σ error, while black dotted line is the steepest curve in 1-σ error, the parameters' values of these curves are the cross points in Fig. 2.6. Right panel: minimum $\epsilon_{\rm cr}$ vs. s for NGC 4945 (upper), NGC 1068 (lower).

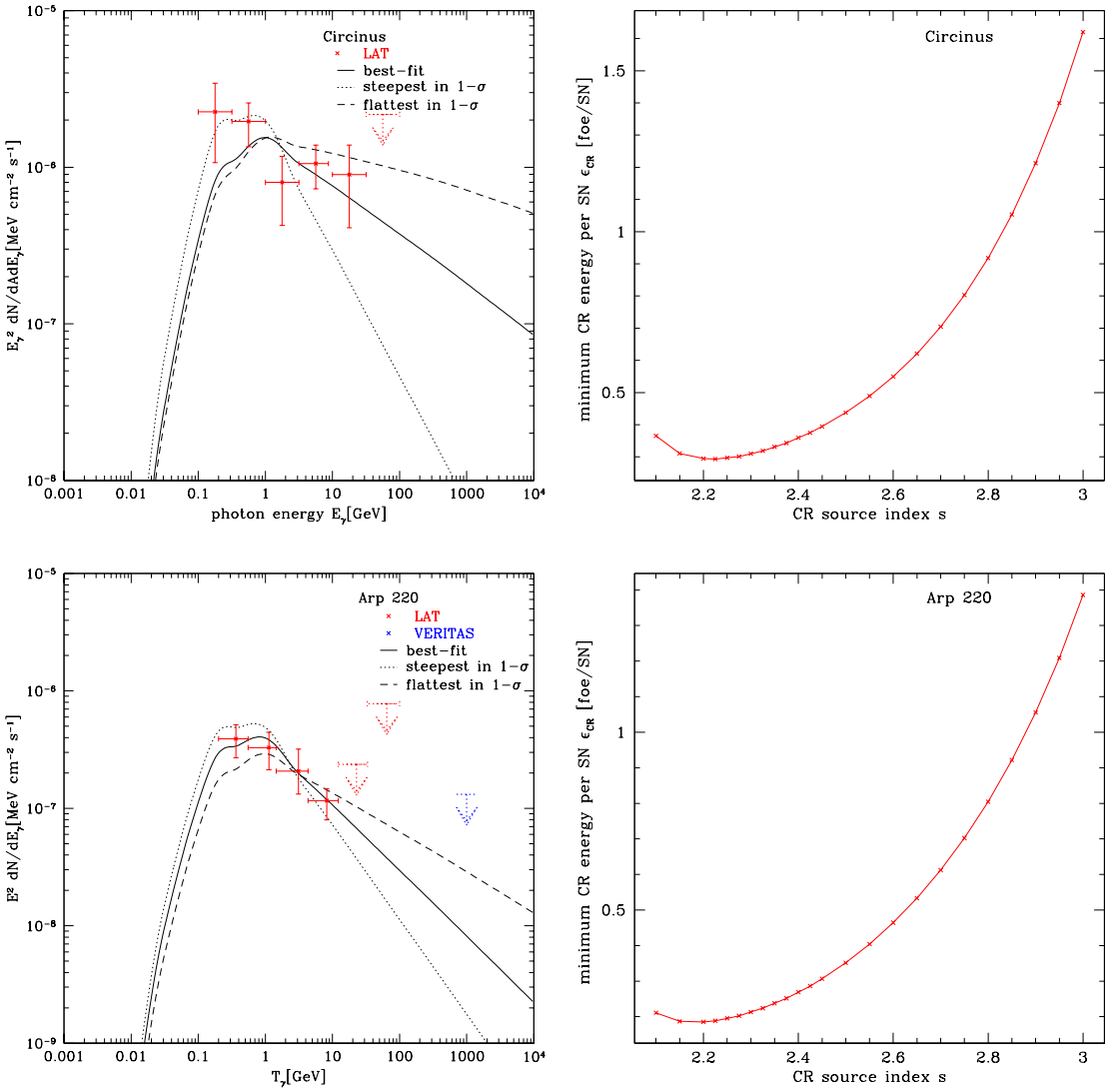

Figure 2.5: Left panel: Pionic gamma-ray spectra (solid curve) for the Circinus galaxy (upper) and Arp 220 (lower) with the best-fit parameters: source CR index s and accelerated CR energy per SN $\epsilon_{\rm cr}$. *Fermi* points are stars (red), *VERITAS* points are squares (blue), black solid line is our model's best-fit to data; see Table 2.2. Black dashed line is our model's flattest curve to fit the data in 1-σ error, while black dotted line is the steepest curve in 1-σ error, the parameters' values of these curves are the cross points in Fig. 2.6. Right panel: minimum $\epsilon_{\rm cr}$ vs. s for the Circinus galaxy (upper) and Arp 220 (lower).

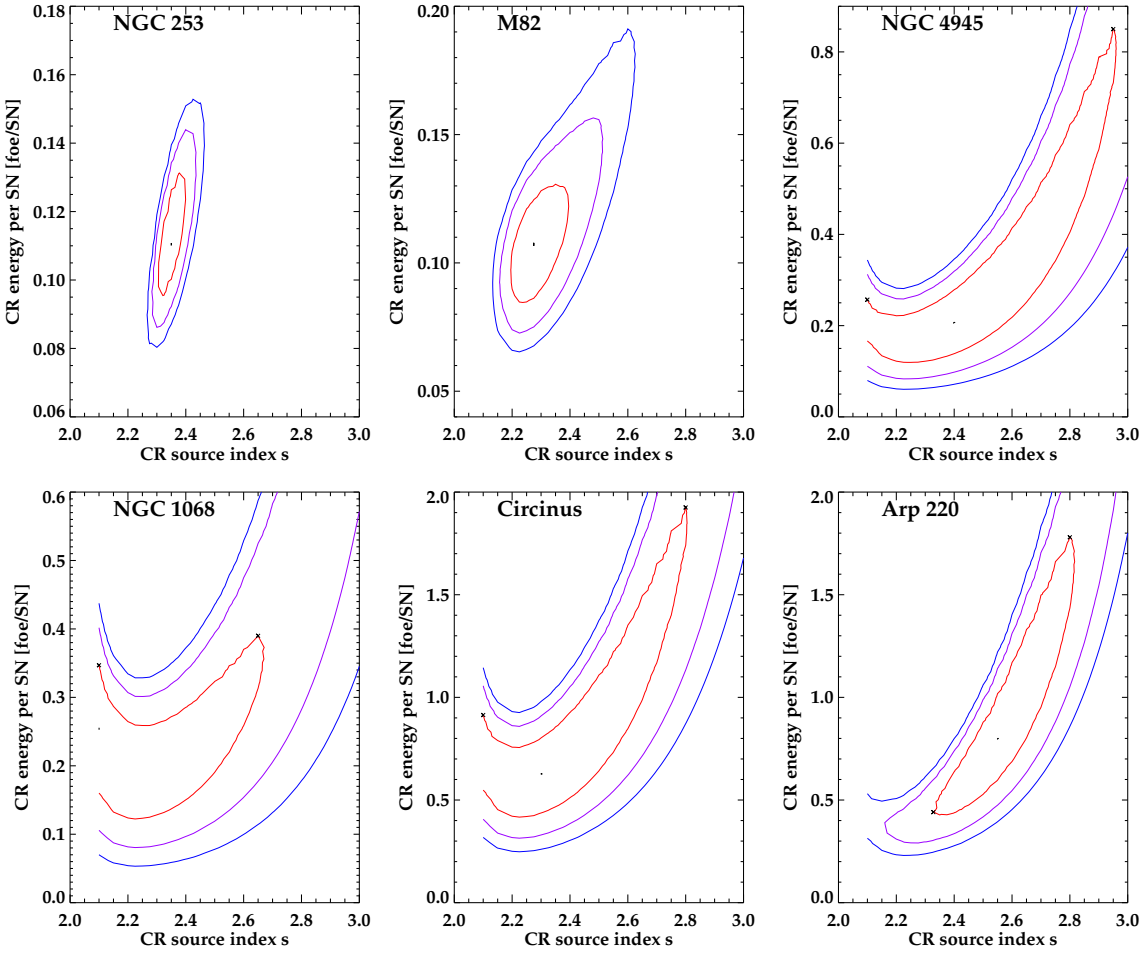

Figure 2.6: Contour plots of χ^2 for our model fits to starburst galaxy data. The best-fit values are the central black dot; (red, magenta, blue) lines represent (70 percent CL, 95 percent CL, 99 percent CL). For starbursts without TeV data and the ULIRG Arp 220, the 1-σ fit values of the flattest and steepest curves are the cross points, the corresponding curves are shown in Fig. 2.4 and Fig. 2.5.

shows that GeV data place a lower bound on $\epsilon_{\rm cr}$. Using the χ^2 to find the likelihood function P, we compute $P(> \epsilon_{\rm cr,min}|s) = 95$ percent to derive the 95 percent CL lower limit $\epsilon_{\rm cr,min}$ to the supernova energy per supernova for each value of acceleration index s. Results appear in the left panels of Figs. 2.4 and 2.5, where we see that $\epsilon_{\rm cr,min}$ is always at its smallest values for $s \sim 2.2$, i.e., the preferred theoretical and Milky-Way value. But as s increases, $\epsilon_{\rm cr}$ becomes quite large. This reiterates that TeV data for these starburst is critical to CR spectral index s and thus getting better-constrained value for $\epsilon_{\rm cr}$.

For starbursts and Arp 220 without TeV data, we illustrate the allowed high-energy behavior by plotting the $\pm 1\sigma$ flattest and steepest curves (the parameters values are the cross points in the contour plots Fig. 2.6) in addition to the best-fit curves (the parameters values are the central points in Fig. 2.6). Comparing these curves at TeV range with the sensitivities of *VERITAS*, *H.E.S.S* and *CTA*, we see that in the optimistic cases, *VERITAS* and *H.E.S.S* could measure the TeV signals from NGC 1068, NGC 4945 and the Circinus galaxy. *CTA* should perform well for all the five starbursts, and may be able to detect Arp 220 in a long-term observation as Arp 220's TeV flux is around the sensitivity of *CTA* in 50 hours (Hassan et al., 2015).

2.4.2 Calorimetric Limit

From eq. 2.13, in our closed box model the ratio of gamma-ray luminosity to the star-formation rate ψ depends only on the $(\epsilon_{\rm cr}, s)$ parameters. Further, a galaxy's star formation rate ψ scales with its far IR luminosity due to reprocessing of starlight by dust Kennicutt (1998),

$$\frac{\psi}{M_\odot yr^{-1}} = 1.3 \times 10^{-10} \frac{L_{8-100\mu m}}{L_\odot} \tag{2.16}$$

where the proportionality constant used here (Ackermann et al., 2012) is for a Chabrier (2003) initial mass function. In closed-box gamma emitters, therefore, the ratio $L_\gamma / L_{\rm IR}$ also

only depends on $\epsilon_{\rm cr}$ and s:

$$L_\gamma/L_{8-100\mu m} \;=\; \frac{L_\gamma}{\psi}\frac{\psi}{L_{8-100\mu m}} \tag{2.17}$$

where L_γ/ψ is from our model's eq. 2.13, $\psi/L_{8-100\mu m} = 1.3\times10^{-10} M_\odot yr^{-1}/L_\odot$ from eq. 2.16. This ratio provides a measure of calorimetry as we have defined it and encoded in our model.

The expected calorimetric limit ratio $L_{>1\rm GeV}/L_{8-100\mu m}$ for CR nuclei with $s = 2.0$ is $L_\gamma/L_{8-100\mu m} \sim 5.2\times10^{-4}(\epsilon_{\rm cr}/0.3$ foe) for our thick-target model. For comparison, this is significantly higher than Thompson, Quataert and Waxman (2007)'s $\sim 10^{-5}(\epsilon_{\rm cr}/0.05$ foe), but is in good agreement with Lacki et al. (2011) ratio $3.1\times10^{-4}(\epsilon_{\rm cr}/0.1$ foe) and with *Fermi* group's result $2.5\times10^{-4}(\epsilon_{\rm cr}/0.1$ foe) (Ackermann et al., 2012).

The systematic uncertainties of our calorimetric model's gamma-ray luminosity mainly come from two sources. One is the uncertainty in the $L_{\rm IR}$-SN rate conversion. While the $L_{\rm IR}$-SFR conversion introduces the error with a factor of 2-3 (Kennicutt, 1998), the fact that both SN rate and far-IR luminosity arise from massive stars brings a cancellation of the error, making the final $L_{\rm IR}$-SN rate calibration uncertainty as good as 10-20 percent (Horiuchi et al., 2011). The other main uncertainty in our model is the cross section $\sigma_{\rm pp}$ of $p-p$ reaction that is generally better than 10 percent (Olive & Particle Data Group, 2014). Furthermore, the calorimetric gamma-ray luminosity derives from the ratio $\sigma_{\rm pp,inelastic}/b(\sigma_{\rm pp,total})$, making additional cancellation of the uncertainty. So the resultant calorimetric gamma-ray luminosity should be good to $\lesssim 30$ percent or better.

The our limit $L_{0.1-100\rm GeV}/L_{8-100\mu\rm m}$ is plotted in Fig. 2.7 for different choices of CR proton index s. Note that our calorimetric limits agree with *Fermi* group's (Ackermann et al., 2012) within 30 percent, which is consistent within uncertainties.

In each of our calculations and plots for individual galaxies, the cosmic-ray acceleration efficiencies correspond to a mean value for all supernovae in the galaxy. We can compare this to typical values of $\epsilon_{\rm cr}$ for Milky Way supernovae taken from the literature. These values

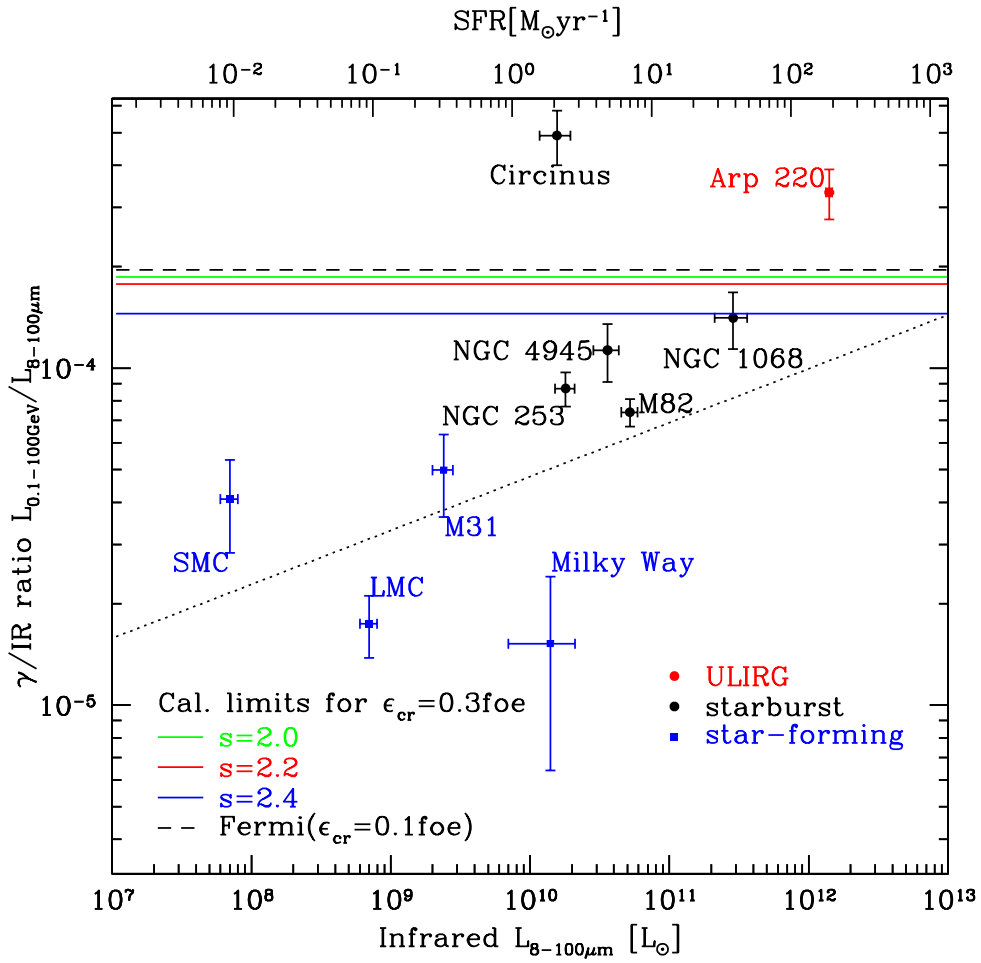

Figure 2.7: Plot of ratio of gamma-ray luminosity ($0.1 - 100$GeV) to total IR luminosity (8-100μm). Blue squares: ordinary star-forming galaxies; black points: starbursts; red: ULIRGs. Milky Way IR and gamma-ray results from Strong et al. (2010), IR data for other galaxies from Sanders et al. (2003), gamma-ray data for SMC (Abdo et al., 2010b), LMC (Abdo et al., 2010a), M31 (Abdo et al., 2010c)). Starburst IR data from Gao & Solomon (2004), gamma-ray data from Ackermann et al. (2012), except for the Circinus (Hayashida et al., 2013) and Arp 220 (Peng et al., 2016). The black dotted line: *Fermi*'s best-fit power law relation (Ackermann et al., 2012). Upper abscissa: SFR estimated from the IR luminosity (Kennicutt, 1998). The blue solid line: calorimetric gamma-ray luminosity limit assuming an average CR acceleration energy per supernova of $\epsilon_{\rm cr} = 3 \times 10^{50}{\rm erg} = 0.3$ foe with source CR index $s = 2.4$; purple and green lines for $s = 2.2$ and $s = 2.0$ respectively.The black dashed line indicated *Fermi*'s calorimetric results ($s = 2.2, \epsilon_{\rm cr} = 10^{50}{\rm erg}$) (Ackermann et al., 2012).

typically vary (e.g., Fields et al., 2001) from 0.1 foe to 0.3 foe (see § 2.3.4). We provisionally adopt a *maximum* value of $\epsilon_{\rm cr,max} = 0.3$ foe in order to judge the proton calorimetry of the starbursts. If $\epsilon_{\rm cr} > \epsilon_{\rm cr,max}$, calorimetry fails for that galaxy, because our model gives an upper-limit to the gamma-ray spectrum, possible explanations are discussed later in this section; if $\epsilon_{\rm cr} < \epsilon_{\rm cr,max}$, the starburst is a proton calorimeter with the calorimetric efficiency

$$\begin{aligned} \eta_{\rm cal} &= \frac{\gamma\text{-ray derived CR acceleration per SN}}{\text{maximum CR acceleration per SN}} \\ &= \frac{\epsilon_{\rm cr}}{\epsilon_{\rm cr,max}} \end{aligned} \tag{2.18}$$

i.e., M82 has a calorimetric efficiency of 35 percent, NGC 253 is 39 percent, NGC 1068 is 84 percent and NGC 4945 is 70 percent. For the Circinus galaxy and the ULIRG Arp 220, there are two possibilities: the galaxy is a fully proton calorimeter (the calorimetric efficiency is 100 percent) with different CR behavior; the calorimetry relation fails.

The proton calorimetry of the starbursts could also be judged by Fig. 2.7, which shows both the calorimetric limit from our model and data for all star-forming galaxies with gamma-ray detections. Here there are two measurements of the ULIRG Arp 220. Griffin et al. (2016) measure the luminosity of Arp 220 to be $8.22 \pm 3.0 \times 10^{41}$ergs/s in the energy band $[0.8, 100]$GeV, while our model's calorimetric limit L_γ in the same energy range is 5.7×10^{41}ergs/s; another independent group Peng et al. (2016) report their gamma-ray luminosity to be $1.39 \pm 0.31 \times 10^{42}$ergs/s in the energy band $[0.2, 100]$GeV, while our calorimetric limit result is 0.95×10^{42}ergs/s. Therefore, although Arp 220 is high above the calorimetric limits in Fig. 2.7, within the errors, the observed gamma-ray luminosity is not far from or even compatible with our model's calorimetric limit in the same energy range.

Fig. 2.7 allows us to draw several conclusions.

1. Normal, Milky-Way-like ("quiescent") star-forming galaxies are about an order of magnitude below the calorimetric limits. This is as expected: Milky-Way Galactic cosmic rays are known to be escape-dominated and thus their cosmic rays find themselves

in the thin-target regime, rather than thick-target calorimetric limit. We see that for these systems, most (~ 90 percent) cosmic rays escape before interacting.

2. The starburst galaxies M82, NGC 253, NGC 1068 and NGC 4945 are close to the limits, which shows that calorimetry is a good approximation for these galaxies. This further implies that quiescent and starburst galaxies occupy opposite limits of gamma-ray production.

3. Two galaxies lie above the calorimetric bounds. The Circinus galaxy lies substantially above these limits. For Arp 220, the situation is somewhat less clear.

In the case that a galaxy's gamma-ray emission truly exceeds our bound on proton calorimetry, there are several possible explanations. Two possibilities envision increased pionic emission from cosmic-ray protons, so that the galaxy remains fully a proton calorimeter (Torres, 2004; Lacki & Thompson, 2013; Yoast-Hull et al., 2015). This could occur if a galaxy harbors supernovae that are systematically more efficient accelerators than in the present Milky Way, i.e., exceeding our adopted value $\epsilon_{\rm cr,max} = 0.3$ foe. Presumably this would reflect systematically more energetic explosions and/or more favorable particle injection. A test for this scenario would be that cosmic-ray electron signatures should be similarly enhanced, e.g., radio synchrotron, or IC emission below the pion bump. A higher pionic flux would also follow if supernova rates are underestimated by far-infrared luminosity measurements, i.e, the scaling relation between the far-infrared luminosity and SFR/supernova rate is different (e.g. Hayashida et al., 2013; Fox & Casper, 2015). This would require that *less* UV from massive stars is reprocessed by dust than in quiescently star-forming galaxies, which seems difficult to arrange in starburst and/or ULIRGs.

A galaxy may also exceed the calorimetric bound because the gamma-ray emission is dominated by sources other than protons (e.g., Downes & Eckart, 2007; Sakamoto et al., 2008; Wilson et al., 2014; Tunnard et al., 2015; Yoast-Hull et al., 2017). Electron gamma emission could dominate if there is a much larger electron/proton ratio in the galaxy's

cosmic rays, or if proton escape is important (also see § 2.3.1 for primary and secondary electron emissions as well as diffusion and advection loss effects); this would imply that the gamma-ray spectrum should not show a pion feature. Finally, a galaxy can exceed our bound if it harbors an active nucleus in which a supermassive black hole jet powers gamma-ray emission. A signature here would be the time variability that is characteristic of most gamma-ray signals from active galaxies.

2.4.3 Neutrino estimation for individual starbursts

The same CR-ISM interactions that produce gamma rays also generate cosmic neutrinos, because *pp* collisions create both neutral and charged pions (e.g., Halzen & Hooper, 2002). The charged pions decay to neutrinos via $\pi^+ \rightarrow \nu_\mu \bar{\nu}_\mu \nu_{\rm e} e^+$ and $\pi^- \rightarrow \bar{\nu}_\mu \nu_\mu \bar{\nu}_{\rm e} e^-$. Thus starburst galaxies are guaranteed high-energy neutrino sources (e.g., Loeb & Waxman, 2006; Lacki et al., 2011), though their detectability depends upon the detection sensitivity.

In *pp* collisions, isospin considerations demand that $N_{\pi^\pm} \simeq 2N_{\pi^0}$ and the flavor ratio after oscillations is $\nu_{\rm e} : \nu_\mu : \nu_\tau = 1 : 1 : 1$ for both neutrinos and antineutrinos (Kamae et al., 2006; Kelner et al., 2006). The differential fluxes of gamma-rays and single-flavor neutrino $(\nu_i + \bar{\nu}_i, {\rm i} = {\rm e}, \mu, \tau)$ are approximately related as $dF_{\nu_i}/dE_{\nu_i}(E_{\nu_i} \approx E_\gamma/2) = 2dF_\gamma/dE_\gamma(E_\gamma)$ ignoring kinematic differences and absorption effects (Anchordoqui et al., 2004; Ahlers & Murase, 2014; Murase et al., 2013). Therefore for a given starburst galaxy, we estimate the upper-limit to its neutrino flux at high energy by our model's calorimetric pionic gamma-ray result and thus constrain the flux measured from neutrino telescopes like IceCube.

For the case of M82, our model gives a flux $F_{\gamma,2{\rm TeV}-2{\rm PeV}} \sim 5.2 \times 10^{-14}{\rm phcm^{-2}s^{-1}}$, the associated single-flavor neutrino flux $(1{\rm TeV} - 1{\rm PeV})$ would thus be $F_{\nu,1{\rm TeV}-1{\rm PeV}} \sim 1.0 \times 10^{-13}{\rm cm^{-2}s^{-1}}$, $dF_\nu/dE_\nu \sim 6.6\times10^{-14}(E_\nu/TeV)^{-2.275}{\rm cm^{-2}s^{-1}}$, $dF_\nu/dE_\nu(E_\nu = 1{\rm TeV}) \sim 6.6\times 10^{-14}{\rm cm^{-2}s^{-1}}$. For IceCube, the median sensitivity at 90 percent CL is $\sim 10^{-12}{\rm TeV^{-1}cm^{-2}s^{-1}}$ for energies between $1{\rm TeV} - 1{\rm PeV}$ with an E^{-2} spectrum and the upper-limit of M82 got by IceCube $\Phi^{90\ {\rm percent}}_{\nu_\mu+\bar{\nu}_\mu} = 2.94 \times 10^{-12}{\rm TeV^{-1}cm^{-2}s^{-1}}$ (IceCube Collaboration et al., 2014).

Therefore our model's estimated neutrino flux of M82 is well below the upper limit, and is more than 10 times too faint to be observed by current IceCube, in agreement with Lacki & Thompson (2013) and Murase & Waxman (2016)'s conclusion. However, stacking searches of starbursts may get a detectable signal in the next generation detectors (Lacki et al., 2011; Murase & Waxman, 2016), and the starbursts can contribute to the diffuse neutrino background that may also be detectable (Loeb & Waxman, 2006).

2.5 Discussion and Conclusions

We have constructed a two-parameter, closed-box, thick-target model to explain the gamma-ray emission from, and test the cosmic-ray calorimetry of, starburst galaxies. Pohl (1993, 1994) presented a prescient theoretical study of the calorimetric behavior of galaxies in the EGRET era. He characterized star-forming galaxies in the thick-target limit as "fractional calorimeters" for both hadrons and leptons. Specifically, Pohl pointed out that fraction of cosmic-ray energy returned in gamma-rays reflects a combination of the fraction of particle loss mechanism that can lead to gammas, and the branching to gammas in those interactions. Our approach is guided by this point of view, and we now have the benefit of GeV and TeV data on star-forming galaxies to test these ideas.

In addition, gamma-ray emission from starburst galaxies has been calculated by a number of groups (e.g., Paglione et al., 1996; Torres, 2004; Persic et al., 2008; de Cea del Pozo et al., 2009; Lacki et al., 2010, 2011; Yoast-Hull et al., 2013; Eichmann & Becker Tjus, 2016). These important papers follow calculation procedures similar to ours, and also solve the one-zone diffusion-loss equation (e.g., Meneguzzi et al., 1971; Longair, 1981) to obtain steady-state particle spectrum and in turn the gamma-ray emission. However, these papers and ours differ in several assumptions, variables and formula numerical calculations. (1) Previous treatments use the general solution to the diffusion-loss equation with different parameter choices, except for (Yoast-Hull et al., 2013, 2014, 2015) who adopt an approximate

solution with loss dominant assumption and diffusion emitted, while ours is a thick target approximation with a "closed-box" calculation, restricting ourselves to proton interactions in order to place a firm and well-defined upper-limit of the hadronic gamma emission. (2) In order to get the pionic gamma-ray spectrum dq_γ/dE_γ (eq. 2.7), we carry a full numerical evaluation of the emissivity dq_π/dE_π (eq. 2.6), while other groups either adopt the parameterization equations of differential cross section $d\sigma_\pi(E_p, E_\pi)/dE_\pi$ directly (e.g., Torres, 2004; Domingo-Santamaría & Torres, 2005), or use *GALPROP* code to calculate the differential cross section from pp collision (e.g., Lacki et al., 2010), or assume a delta function approximation for pion distribution (Yoast-Hull et al., 2013, 2014, 2015), or directly use the analytical form of the gamma energy distribution given by Kelner et al. (2006) (Eichmann & Becker Tjus, 2016). (3) These calculations to various extents present multi-frequency and multi-process models, i.e., radio plus gamma-ray emission, with both leptonic process (synchrotron, bremsstrahlung and inverse Compton) and hadronic process (pion decay) in a more complex and realistic way. This naturally entails more free parameters like the source CR parameters for both electrons and protons, diffusion loss time scale, advection loss timescale, magnetic field, gas density.

Our model *by construction* is less ambitious than these other studies, but very well-defined with only two parameters $(s, \epsilon_{\rm cr})$. Our results are, for example, independent of the galaxy's gas density. Thus our model is targeted to (1) offer a particularly direct and simple means of estimating these fundamental parameters in starburst galaxies, thus measuring their cosmic-ray acceleration properties that can be compared with those in the Milky Way; and (2) place a firm and careful upper limit to the hadronic gamma-ray luminosity of *any* star-forming galaxy.

For individual starburst galaxies, our model gives good fits to the gamma-ray data in both GeV and TeV range with proper choices of the injected proton index s and cosmic-ray proton acceleration energy per supernova $\epsilon_{\rm cr}$, showing the thick-target assumption is a plausible explanation of the observed starburst GeV and TeV emission. Our model shows

that the gamma-ray spectrum of thick-target systems shares the same index as the CR "injection" index, instead of the CR propagated index. This contrasts with the "thin-target" situation that should correspond to ordinary star-forming galaxies like Milky Way. Our fit gives the average value of s in starbursts to be ~ 2.3, which is consistent with the LAT measurement of Galactic SNRs with an average value of s to be 2.39 (Acero et al., 2016), implying that cosmic-ray acceleration by supernovae is broadly similar in starburst galaxies and the Milky Way.

The goodness of our fit of starbursts M82, NGC 253, NGC 1068 and NGC 4945 suggest that starburst galaxies are proton calorimeters with calorimetric efficiencies vary from 35 percent to 84 percent. These efficiencies may be different in reality if the actual supernova acceleration of CR rate in starbursts differ from the maximum CR acceleration energy $\epsilon_{\rm cr,max} = 0.3$ foe we have adopted; the scaling is simply $\eta_{\rm cal} = \epsilon_{\rm cr}/\epsilon_{\rm cr,max}$ (eq. 2.18) . For the Circinus galaxy, our model's gamma-ray luminosity agrees with Hayashida et al. (2013), and is above our limit, as is the ULIRG Arp 220. The gamma excesses may be explained in two ways: the galaxy is a full proton calorimeter or proton calorimetry fails for the galaxy, detailed discussions see §2.4.2. Therefore we conclude that at least for currently observed starbursts, most are nearly or fully proton calorimeters. Others have also addressed the question of proton calorimetry in starbursts. For example, Yoast-Hull et al. (2013, 2014) find M82 and NGC 253 50 percent proton calorimeters, Ackermann et al. (2012) get calorimetric efficiencies of 30 percent $-$ 50 percent for starburst galaxies with SFR $\sim 10 {\rm M}_\odot {\rm yr}^{-1}$, while Lacki et al. (2010, 2011) conclude that proton calorimetry holds for starburst galaxies with $\Sigma_{\rm gas} > 1 {\rm g\ cm}^{-2}$ and the calorimetric fraction is 0.2 for NGC 253 and 0.4 for M82. Moreover, Torres (2004), Lacki & Thompson (2013) and Yoast-Hull et al. (2015) conclude that Arp 220 is a hadronic calorimeter or nearly so. Our conclusions are consistent with these.

More data can further test starburst proton calorimetry. There are no published starburst data at energies ∼30-100 MeV; observations in this regime should reveal the characteristic "pion bump." TeV data for NGC 1068, NGC 4945, Circinus, and Arp 220 is also needed to

constrain the choices of parameters (both s and $\epsilon_{\rm cr}$) in our model with smaller uncertainty. If Arp 220 indeed saturates the proton calorimeter limit, it is the best example of a star-forming galaxy as a proton calorimeter, but it lies at the edge of GeV detectability and has no TeV measurements. As discussed in §2.4.1, *VERITAS* or *H.E.S.S* could measure the TeV signals from the starbursts NGC 1068, NGC 4945 and the Circinus galaxy within their sensitivities. Future *CTA* observations should dramatically improve our understanding of starburst galaxies, and may be able to detect Arp 220 in a long-term dedicated observation.

There still remains space to improve our model. Future work would benefit from better observational determination of galaxy distances, star-formation and supernova rates, and of course well-measured TeV gamma-ray data. The particle experimental data adopted in our model is as old as from 1980s, we would like to call for new measurements of the pion momentum distribution in the $p - p$. These data are important not only for gamma-ray emissions but also for the inelastic losses of CRs. Theoretical work would benefit from additional multi-wavelength constrains on the cosmic-ray electrons (add leptonic process in our model). Finally, if a starburst could be resolved spatially, perhaps in the TeV, this would motivate consideration of the supernova and gas distributions inside a starburst.

2.6 Supplements

2.6.1 Order-Of-Magnitude Estimates

An order of magnitude calculation of our model will help to give a sense of the final results and frame key physical issues. We aim to find the calorimetric gamma-ray emission from individual starburst galaxies.

For a starburst galaxy, the injected cosmic-ray energy rate got from supernovae explo-

ration is:

$$\begin{aligned} dE_{\rm cr}/dt &= f_{\rm cr}E_{\rm sn}R_{\rm sn} = \epsilon_{\rm cr}R_{\rm sn} \\ &= \int E_{\rm p}dN_{\rm p}/dt = L_{\rm cr} \end{aligned} \tag{2.19}$$

assuming the injected cosmic-ray spectrum is a power law in momentum here, $q_{\rm p} = dN_{\rm p}/dE_{\rm p}dt = dq/dp_{\rm p} = Cp_{\rm p}^{-s}, dE_{\rm cr}/dt = C\int_{p_{\rm min}} E_{\rm p}p_{\rm p}^{-s}dp_{\rm p}, dN_{\rm cr}/dt = C\int_{p_{\rm min}} p_{\rm p}^{-s}dp_{\rm p}$, where C is a constant, $p_{\rm min}$ is the minimal momentum of injected CR protons that can be accelerated by SN.

Our model assumes all cosmic-rays will interact with interstellar medium, the interactions involve both elastic and inelastic scattering, in the GeV energy range. Thus we can get a crude estimation that the elastic scattering CR number is about the same as the inelastic number, i.e., $dN_{\rm cr,inelastic}/dt \sim dN_{\rm cr,elastic}/dt \sim (dN_{\rm cr}/dt)/2$. For the inelastic scattering, only neutral pions could decay into photons, which take up one third of the total produced pion numbers, therefore $dN_\gamma/dt = 2dN_{\pi^0}/dt \sim 2(dN_{\rm cr,inelastic}/dt(E_{\rm cr} > E_{\rm threshold}))/3 \sim (dN_{\rm cr}/dt(E_{\rm cr} > E_{\rm threshold}))/3 = \dot{N}_{\rm cr,threshold}$, where $E_{\rm threshold}$ is the threshold kinetic energy of CR proton that can produce a pion.

$$\begin{aligned} \dot{N}_{\rm cr,threshold} &= dN_{\rm cr}/dt(E_{\rm cr} > E_{\rm threshold}) \\ &\propto \int_{p_{\rm threshold}} p_{\rm p}^{-s}dp_{\rm p} \propto \frac{p_{\rm threshold}^{1-s}}{s-1} \end{aligned} \tag{2.20}$$

In this case, we can get an estimation of the gamma-ray (number) flux from the thick-target model is:

$$\begin{aligned} F_\gamma &= \frac{1}{4\pi d^2}\frac{dN_\gamma}{dt} \\ &= \frac{1}{4\pi d^2}\frac{dN_\gamma/dt}{dE_{\rm cr}/dt}dE_{\rm cr}/dt \\ &= \frac{1}{4\pi d^2}\epsilon_{\rm cr}R_{\rm sn}\frac{1}{3}f_{\rm threshold} \end{aligned} \tag{2.21}$$

where $f_{\rm threshold} = \dot{N}_{\rm cr,threshold}/L_{\rm cr}$ is the average CR injected energy per above-threshold proton.

If $p_{\rm p} < m_{\rm p}$, protons can be approximated to be nonrelativistic, thus $E_{\rm p} \approx p_{\rm p}^2/2m_{\rm p}$, while if $p_{\rm p} > m_{\rm p}$, protons can be approximated to be relativistic, $E_{\rm p} \approx p_{\rm p}$, and $2 < s < 3$, therefore we have:

$$\begin{aligned} L_{\rm CR} &\propto \int_{p_{\rm min}} E_{\rm p} p_{\rm p}^{-s} dp_{\rm p} \\ &\propto \int_{p_{\rm min}}^{m_{\rm p}} \frac{p_{\rm p}^2}{2m_{\rm p}} p_{\rm p}^{-s} dp_{\rm p} + \int_{m_{\rm p}}^{\infty} p_{\rm p}^{1-s} dp_{\rm p} \\ &\propto \frac{m_{\rm p}^{2-s}}{2(3-s)}[1 + \frac{6-2s}{s-2} - (\frac{p_{\rm min}}{m_{\rm p}})^{3-s}] \end{aligned} \tag{2.22}$$

For fixed s, $\delta L_{\rm cr} \sim (\delta p_{\rm min}/m_{\rm p})^{3-s} \sim (\delta E_{\rm min}/m_{\rm p})^{\frac{3-s}{2}}$, when s=2.2, $\delta L_{\rm cr} \sim (\delta E_{\rm min}/m_{\rm p})^{0.4}$.Therefore for $2 < s < 3$, we can see that $L_{\rm cr}$ from CR spectrum is insensitive to $p_{\rm min}$, which is fortunate as there is no accurate determination of $p_{\rm min}$, and most $L_{\rm cr}$ comes from $p_{\rm p} \sim m_{\rm p}$.

Let $s = 2.2, f_{\rm cr} = 0.1, E_{\rm sn} = 10^{51}{\rm erg}, \epsilon_{\rm cr} = 10^{50}{\rm erg}, E_{\rm min} = 0.001{\rm GeV}, E_{\rm threshold} = 0.28{\rm GeV}$,the estimated gamma-ray flux for a certain starburst galaxy with the distance d and supernova rate $R_{\rm sn}$ is $F_\gamma \approx 3.31 \times 10^{50} R_{\rm sn}/d^2$. For the starburst galaxy NGC 253, our oder of magnitude estimation gives the flux to be $4.57 \times 10^{-9}{\rm cm}^{-2}{\rm s}^{-1}$, agrees with *Fermi* measurement $10.7 \pm 2.1 \times 10^{-9}{\rm cm}^{-2}{\rm s}^{-1}$ (Hayashida et al., 2013) in an order of magnitude.

2.6.2 Energy Loss Rates

The energy losses other than Pionic process in our model are elastic scattering and ionization, they are expressed as follows (Gould, 1982; Ginzburg & Syrovatskii, 1964):

$$\begin{aligned} b_{\rm elastic,p} &\sim 2.44 \times 10^{-16} \frac{n_{\rm p}}{cm^{-3}} \frac{E_{\rm p}}{\rm GeV} (\frac{E_{\rm p}}{m_{\rm p}c^2})^{1/2} \\ &\quad \frac{(1 + E_{\rm p}/2m_{\rm p}c^2)^{1/2}}{1 + E_{\rm p}/m_{\rm p}c^2} {\rm GeVs}^{-1} \end{aligned} \tag{2.23}$$

$$b_{\rm ionic,p} \sim 1.83\times10^{-17}(\frac{n_{\rm H}+2n_{\rm H_2}}{cm^{-3}})\frac{c}{v_{\rm p}}\{10.9+2\ln(\frac{E_{\rm p}}{m_{\rm p}c^2}) + \ln(\frac{{v_{\rm p}}^2}{c^2})-\frac{{v_{\rm p}}^2}{c^2}\}{\rm GeVs}^{-1} \quad (2.24)$$

where $n_{\rm p}$ and $n_{\rm H}+2n_{\rm H_2}$ are the number densities of protons in the ISM, which are equal to $n_{\rm gas}$. Here, $E_{\rm p}$ is the total energy of a proton, $T_{\rm p}$ denotes kinetic energy of a proton. In GeV energy range, elastic scattering contributes about 50 percent lower than inelastic scattering does to the total energy-loss during CR propagation. Therefore it is necessary to include elastic scattering during the propagation.

At high energy, $E_{\rm p}\sim T_{\rm p}$: As Fig. 2.8 shows, for $T_{\rm p}>100$GeV, $b(E_{\rm p})\propto E_{\rm p}$, therefore, eq. 2.5 gives $\phi_{\rm p}\propto {E_{\rm p}}^{-s}$;and for high T_π,$d\sigma_\pi(T_{\rm p},T_\pi)/dT_\pi=\langle\zeta\sigma_\pi(T_{\rm p})\rangle dN(T_{\rm p},T_\pi)/dT_\pi\propto 1/T_{\rm p}$, we can get $q_\pi\propto E_\pi^{-s}$ from eq. 2.6 in § 2.3.3, thus $q_\gamma\propto E_\gamma^{-s}$, or $F_\gamma\propto E_\gamma^{-s}$. Therefore the gamma-ray spectrum obtained from our thick-target model has the same spectral index s as the injected proton's.

An analytical fit to our self-consistent inelastic energy loss appears is shown in Fig. 2.8 as the black dotted curve. The fit is good with fractional error less than 2 percent over the *Fermi* energy range. The fitting function is:

$$\begin{aligned} Y = {} & 0.631x^2+0.502x-0.441, x_{\rm threshold}\le x\le -0.24 \\ & -1.66x^2-0.605x-0.575, -0.24\le x\le -0.05 \\ & -0.430x-0.568, -0.05\le x\le 0.6 \\ & -0.643x-0.440, 0.6\le x\le 0.75 \\ & -0.157\ln(x-0.639)-1.26, 0.75\le x\le 1.10 \\ & -0.677\ln(x+0.817)-0.701, 1.10\le x \end{aligned} \quad (2.25)$$

where $Y=\log_{10}(b_{\rm inelastic}/\langle\zeta\sigma_\pi(X)\rangle)$ with $x=\log_{10}(T_{\rm p}/1{\rm GeV})$, $x_{\rm threshold}=\log_{10}(T_{\rm p}^{min}/1{\rm GeV})$, for $n_{\rm gas}=1$ cm^{-3}.

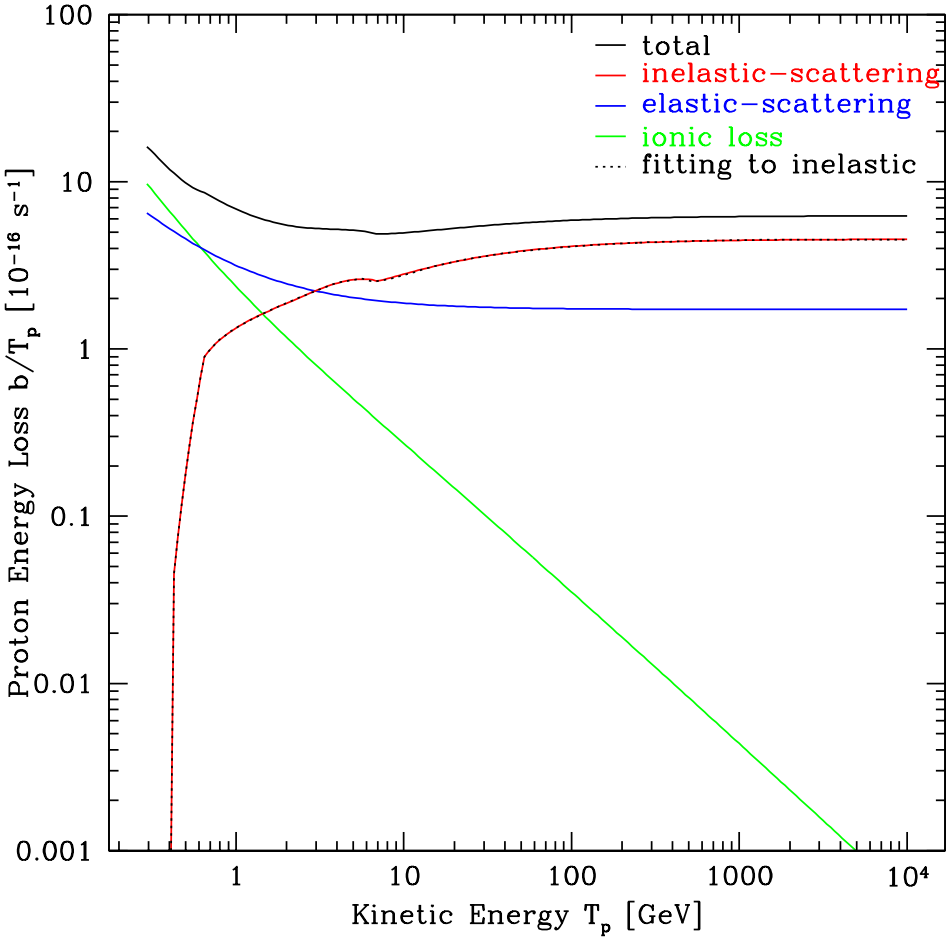

Figure 2.8: Proton Energy Losses. The black line is the total energy loss rate per proton kinetic energy, blue line is elastic energy loss rate per proton kinetic energy, green line is ionic energy loss rate per proton kinetic energy, red line is inelastic (pionic) energy loss rate per proton kinetic energy, black dotted line is our fit curve to inelastic energy loss. Here $n_{\rm gas} = 1$ cm^{-3}.

Finally, can use these results to compare collisional timescales to the timescales for other cosmic-ray losses. For a starburst, at GeV energy range, the diffusion timescale is $\tau_{\rm diff} \sim H^2/2D \sim 5 \times 10^6$yr, where $H \sim 1$kpc is the height of the disk, and we use the diffusion coefficient $D \sim 3 \times 10^{28}{\rm cm}^2/{\rm s}$ for 1 GeV protons in our Galaxy. [3] The advective escape timescale $\tau_{\rm adv} \sim r_{\rm s}/v_{\rm wind} \sim 10^6$yr is the time for a wind of speed $v_{\rm wind} \sim 300$km/s to cross the starburst nucleus region of radius $r_{\rm s} \sim 0.3$kpc (Rephaeli & Persic, 2013; Yoast-Hull et al., 2013; Lacki & Thompson, 2013). The CR interaction loss timescale is $\tau_{\rm loss} \sim E_\gamma/b \sim 1 \times 10^5$yr with the atomic hydrogen density of the interstellar medium $n_{\rm gas} \sim 500{\rm cm}^{-3}$, where b is the rate of energy loss (see Fig. 2.8 for E_γ/b value).

2.6.3 Code Description

We build a simple code following the calculation in § 2.3, using the Simpson method to do integration and the relative errors for the integrations set to be 10^{-4}. Because the model is closed box, we can do conservation check of the code: $N_\gamma = 2N_\pi = 2N_{\rm p}/3$ (number conservation), and $L_\gamma = L_\pi < L_{\rm p}/3$ (energy conservation) (Kelner et al., 2006). The code results we get fulfill the conservation check. To reduce the CPU time taken for code running, instead of doing the 3-layer integration, we do the first 2-layer integration first to get the values of q_π vs. E_π and store them as vectors, then doing the third integration to get q_γ simply by doing interpolation and extrapolation to the stored values of q_π.

2.6.4 Nuclear Enhancement Factor

In the thick-target model, the gamma-ray luminosity follows from the production and decay of neutral pions, which are dominantly produced in collisions between cosmic-ray protons and ISM protons. Heavier nuclei in both cosmic rays and the ISM an also produce neutral pions.

[3] As $D \sim E^\delta$ with $\delta \sim 0.5$, the escape timescale at TeV will be shorter, but most of the CR energy is around 1 GeV, so escape has little affect on the energy loss for the protons of interest to us. We thank the referee for pointing this out.

This effect is encoded in a "nuclear enhancement factor" $\mathcal{A}$ to be multiplied to the gamma-ray yield assuming cosmic-ray protons on ISM protons only: $dq_\gamma^{\rm total}/dE_\gamma = \mathcal{A} dq_\gamma^{\rm pp,only}/dE_\gamma$.

Assume all cosmic-ray species (j = p, He, CNO, NeMgSiS, Fe) have source spectra with the same shape in energy per nucleon $\epsilon = E_{\rm i}/A_{\rm i}$, and differ only by cosmic-ray source abundances $y_j^{\rm cr}$:

$$\frac{dq_j}{d\epsilon} = y_j^{\rm cr}\ \frac{dq_{\rm p}}{d\epsilon}. \tag{2.26}$$

Thus the cosmic-ray power needed to accelerate species j is

$$L_{{\rm cr},j} = \int dV \int E_j \frac{dq_j}{d\epsilon} d\epsilon = A_j y_j^{\rm cr}\ L_{\rm cr,p} \tag{2.27}$$

and thus the total cosmic-ray source luminosity scales with the proton luminosity as

$$L_{\rm cr} = L_{\rm cr,p} \sum_j A_j y_j^{\rm cr} = \epsilon_{\rm cr} R_{\rm sn} \tag{2.28}$$

and

$$q_{\rm cr} = q_{\rm p} \sum_j A_j y_j^{\rm cr} \tag{2.29}$$

For a closed-box model, the total flux in species j is

$$\Phi_j = \frac{v_j}{b_j} \int \frac{dq_j}{d\epsilon} d\epsilon = y_j^{\rm cr} \frac{b_{\rm p}}{b_j} \Phi_{\rm p} \tag{2.30}$$

For energy losses due to nuclear interactions between CR nuclei j and ISM nuclei i, we assume that the cross sections for $j + i \to \pi^0 + \cdots$ scale with the $pp \to \pi^0$ cross sections as $\sigma_{\rm ji}^{\rm inelastic}/\sigma_{\rm pp}^{\rm inelastic} = \sigma_{\rm ji}^{\rm elastic}/\sigma_{\rm pp}^{\rm elastic} = \sigma_{\rm ji}^{\rm total}/\sigma_{\rm pp}^{\rm total}$. This leads to energy loss rates (per nucleon)

for species j of

$$b_j = b_j^{\rm inelastic} + b_j^{\rm elastic} = b_{\rm pp} \sum_{\rm i} y_{\rm i}^{\rm ISM} \frac{\sigma_{\rm ji}^{\rm t}}{\sigma_{\rm pp}^{\rm t}} \tag{2.31}$$

$$b_{\rm p} = b_{\rm pp} \sum_{\rm i} y_{\rm i}^{\rm ISM} \frac{\sigma_{\rm pi}^{\rm t}}{\sigma_{\rm pp}^{\rm t}} \tag{2.32}$$

where $y_{\rm i}^{\rm ISM} = n_{\rm i}/n_{\rm p}$.

The emissivities of pions and gamma-ray induced by CR interactions are

$$\frac{dq_\pi^{\rm ji}}{dE_\pi} = \int d\epsilon_{\rm j} n_{\rm i} \Phi_{\rm j} \langle \zeta_{\rm ji}^\pi \sigma_{\rm ji}^\pi \rangle \frac{dN}{dE_\pi}(\epsilon_{\rm i}, E_\pi) \tag{2.33}$$

$$\frac{dq_\gamma^{ji}}{dE_\gamma} = 2 \int_{u(E_\gamma)} \frac{dE_\pi}{p_\pi} \frac{dq_\pi^{ji}}{dE_\pi} = \int q_\pi^{ji} \tag{2.34}$$

therefore the nuclear enhancement factor $\mathcal{A}$ can be expressed as

$$\begin{aligned} \mathcal{A} &= \frac{dq_\gamma^{\rm total}/dE_\gamma}{dq_\gamma^{\rm pp,only}/dE_\gamma} \\ &= \int \frac{q_\pi^{\rm pp}}{q_\pi^{\rm pp,only}} \sum_{j,i} \frac{dq_\pi^{\rm ji}/dE_\pi}{dq_\pi^{\rm pp}/dE_\pi} \\ &= \frac{q_{\rm p}}{q_{\rm cr}} \frac{b_{\rm pp}}{b_{\rm p}} \sum_{j,i} \frac{dq_\pi^{\rm ji}/dE_\pi}{dq_\pi^{\rm pp}/dE_\pi} \end{aligned} \tag{2.35}$$

As discussed in Abbott et al. (1992); Miller et al. (2007), the total multiplicity $R_{\rm ji}^{\pi^0}$ for making π^0 through collision of nuclei $i+j$ is almost universal, i.e., $R_{\rm ji}^{\pi^0} = \langle \zeta_{\rm ji}^\pi \sigma_{\rm ji}^\pi \rangle / \sigma_{\rm ji}^{\rm inelastic} = R_{\rm pp}^\pi$ =constant, thus it is safe to assume $\langle \zeta_{\rm ji}^\pi \sigma_{\rm ji}^\pi \rangle / \langle \zeta_{\rm pp}^\pi \sigma_{\rm pp}^\pi \rangle = \sigma_{\rm ji}^{\rm t}/\sigma_{\rm pp}^{\rm t}$ for all energy per nucleon

ϵ for CR nuclei j interact with ISM nuclei i, then we can get

$$\begin{aligned} \mathcal{A} &= \frac{q_{\rm p}}{q_{\rm cr}} \sum_j y_{\rm j}^{\rm cr} \\ &= \frac{1}{\sum\limits_j A_{\rm j} y_{\rm j}^{\rm cr}} \sum_j y_{\rm j}^{\rm cr} = \frac{1}{\langle A \rangle_{\rm cr}}. \end{aligned} \tag{2.36}$$

Considering the same heavier nuclei components in both CR and ISM as Mori (2009) did, if use the relative abundance of H : He : CNO : NeMgSiS : Fe=1:0.153:1.245×10^{-2}:3.65×10^{-3}:1.182×10^{-3} in Meyer (1985), the nuclear enhancement factor is $\mathcal{A} = 0.59$.

2.7 Acknowledgments

We are pleased to thank Keith Bechtol for providing the Fermi data points, Wystan Benbow for providing VERITAS data points, Roger Blandford, Ellen Zweibel and Anne Sickles for the stimulating conversation. This work was supported in part by the NASA Astrophysics Theory Program through award NNX10AC86G. We also thank the referee for her/his productive and valuable comments.

Chapter 3

Using Gamma Rays as an Alarm for the Next Milky Way Type Ia Supernova

3.1 Abstract

A Milky-Way Type Ia Supernova (SNIa) could go entirely unnoticed, being dim in radio, X-rays, and neutrinos, and suffering large optical/IR extinction in the Galactic plane. But SNIa emit nuclear gamma-ray lines from ^{56}Ni $\rightarrow^{56}$ Co $\rightarrow^{56}$ Fe radioactive decays. These lines fall within the *Fermi*/GBM energy range, and the ^{56}Ni 158 keV line is detectable by *Swift*/BAT. Both instruments frequently monitor the Galactic plane, which is transparent to gamma rays. Thus GBM and BAT are ideal Galactic SNIa early warning systems. We simulate SNIa MeV light curves and spectra to show that GBM and BAT could confirm a Galactic SNIa explosion, followed by *Swift* localization and observation in X-rays and UVOIR band. The time needed to sound the alarm depends on the ^{56}Ni distribution, and can be as early as a few days if $\gtrsim 10\%$ of the ^{56}Ni is in an exterior shell as suggested by SN2014J gamma data

3.2 Main Text

Type Ia supernovae (SNIa) play a central role in astrophysics: they are cosmic-ray accelerators (e.g., Ginzburg & Syrovatskii, 1964; Baade & Zwicky, 1934; Ackermann et al., 2013), nucleosynthesis sites of iron-group elements (Nomoto et al., 1984), and standardizable candles for cosmology (Phillips, 1993). A Galactic SNIa, i.e., one exploding in the Milky Way,

This chapter was submitted to Nature Astronomy under the authorship Wang, X., Fields, B., & Lien, A.

would provide unique insight into the SNIa phenomenon.

The Galactic SNIa rate is only ~ 1.4 events/century (Adams et al., 2013), making each explosion a "once in a lifetime" event not to be missed. Unfortunately, if a SNIa exploded in the Milky Way today, there is a real possibility it would be entirely overlooked. Although SNIa are enormously luminous at peak, a Galactic event should lie in the plane of the Milky Way disk that contains obscuring dust. Therefore the large extinction bring a faint optical or infrared signal from a SNIa (Adams et al., 2013). The radio and soft X-ray emission from SNIa are also dim, confirmed by the non-detection of the nearest Type Ia event SN2014J (Pérez-Torres et al., 2014; Margutti et al., 2014). While the SNIa neutrino signal is too weak to be detected by current instruments on earth (Odrzywolek & Plewa, 2011). And gravitational waves detection of SNIa awaits low-frequency, space-based detectors (Webbink, 2010) Moreover, a future Galactic SNIa could happen anywhere anytime in the Galactic plane, most of which are not continually monitored at most wavelengths.

Fortunately, SNIa are confirmed gamma-ray emitters, because the dominant product of these thermonuclear explosions is the doubly-magic yet unstable nucleus ${}^{56}_{28}\mathrm{Ni}^{28}$. The radioactive beta decay series ${}^{56}\mathrm{Ni} \xrightarrow{8.8\mathrm{days}} {}^{56}\mathrm{Co} \xrightarrow{111.3\mathrm{days}} {}^{56}\mathrm{Fe}$ are accompanied by gamma-ray line emission spanning energies from 158keV to 2.6MeV. Observations of the Type Ia supernova SN2014J in M82 claimed detection of the dominant ${}^{56}\mathrm{Ni}$ lines at 158 keV and 812 keV within the first 20 days (Diehl et al., 2014, 2015). Later observations reported the ${}^{56}\mathrm{Co}$ lines at 847keV and 1238keV (Churazov et al., 2015).

The Milky Way is optically thin to gamma rays, so these gamma-ray lines provide a guaranteed signal from a SNIa anywhere in the Galaxy. To exploit these lines as a SNIa alert requires gamma-ray observations of the Galactic disk at least daily. Fortunately, these data are taken as part of the ordinary operation of *Fermi*'s Gamma-ray Burst Monitor (GBM) and *Swift*'s Burst Alert Telescope (BAT).

The GBM consists of 12 NaI and 2 BGO scintillation detectors, and scans the whole

sky every three hours with a large field of view of ∼9.5 steradians [1]. The low energy NaI detectors are sensitive to photons with energy between 8 keV to 1 MeV, while BGO detectors work between 150 keV to 40 MeV, covering all the ^{56}Ni and ^{56}Co decay lines. The BAT is a sensitive coded aperture imaging telescope which points at sources with a 1.4 steradian field of view (half coded) [2]. The BAT energy range is ∼ 15-150 keV for imaging, which is able to detect the ^{56}Ni 158 keV line. The detector frequently looks at the Galactic center at least once per day and its field of view will cover most of the possible regions where next Galactic SNIa will occur[3]. These properties make GBM and BAT ideal Galactic SNIa monitors and alarms.

We now turn to our main analysis, which will confirm the viability of GBM and BAT as SNIa detectors, and assess the time needed to sound the alarm. We follow a GBM lines search approach pioneered by ref.Ng et al. (2015)'s work. To do this, we will 1) model the time history of the SN line emission, then 2) locate our SNIa at a fiducial distance of 10 kpc, and simulate the line features (light curves and spectra) in GBM and BAT. With simulations of the SN light curves (see Methods) and spectra, we can estimate the timescale at which the rising SN signal emerges as distinct from the detector background.

Our model of SNIa line emission follows the radioactive production of ^{56}Ni and ^{56}Co lines and their propagation in the expanding blast. The ejecta is initially quite dense and opaque, but becomes optically thin after ∼ 100 days (coincidentally near the ^{56}Co lifetime) (Sim & Mazzali, 2008; The & Burrows, 2014). The gamma rays of interest lose significant energy in a single Compton scattering event, so that lines in the emergent spectrum are only due to un-scattered photons. Thus, the SNIa gamma line light curves are very sensitive to the structure of the ^{56}Ni distribution in the ejecta. We therefore study two simple ^{56}Ni distributions that give a sense of the optimistic versus pessimistic cases (shell model and core

[1] `http://fermi.gsfc.nasa.gov`

[2] `http://swift.gsfc.nasa.gov`

[3] If BAT is looking at the Galactic center, using BAT partial coding map (`https://swift.gsfc.nasa.gov/proposals/bat_cal/index.html`) and the exponential probability distribution of Galactic SNIa (Adams et al., 2013), we estimate that ∼ 77% of the next Galactic SNIa will fall in the FOV of BAT.

only model, respectively). For both models, we assume a SNIa ejecta of uniform density, homologous expanding, and calculate lines only. The fiducial distance is set to be D =10 kpc[4]. For Details, see Methods.

The SNIa signal will be distinct from other high-energy transient events in the Galactic plane due to the presence of the decay lines, which serve as the SN "smoking gun". Thus, for the two models described in Methods, we simulate the spectra of ^{56}Ni and ^{56}Co decay lines from a Galactic SNIa in a single BGO detector b0 (other detectors will have the similar results), for times day 2, day 12 (when ^{56}Ni lines peak), day 24 (when ^{56}Co lines emerge for core model) and day 96.5 (when ^{56}Co lines peak) after the explosion, shown in Fig. 3.1. We assume the lines have a Gaussian profile, with Doppler broadening corresponding to a line-of-sight velocity of $\sim$ 10000km/s. The Compton scattering continuum is neglected. We adopt a rough criteria of "detectable" to be when SNIa signal/background signal $\sim$ 1, discussions see Methods.

For the shell model with surface nickel, Fig. 3.1 shows that SN Ia ^{56}Ni lines start to be comparable to background just 2 days after the explosion. By 12 days, all of the ^{56}Ni lines are distinct, and are $\sim$3-4 times bigger than the typical background; ^{56}Co lines (especially the dominant 847 keV line) begin to arise as well. Thus, in the shell model we expect GBM could detect a Galactic supernova within a few days, with spectral line features from both ^{56}Ni and ^{56}Co serving to confirm the Type Ia origin of the explosion. Even for the line flux of ^{56}Ni at $\sim$ 2 day and ^{56}Co at $\sim$ 10 days, the signal of a single line emission is actually strong enough for GBM to detect ($\gtrsim$ 100% of the BGO background).

By contrast, the core model lacks surface emission, instead placing the nickel maximally deep. In this pessimistic scenario, the early ejecta are opaque and ^{56}Ni lines are absent. Fig. 3.1 shows that ^{56}Co lines only start to emerge above background around day 24, and rise

[4]This distance is comparable to the distance to the Galactic Center, which is close to the most probable distance to a Galactic SNIa as found in ref. Adams et al. (2013), and consistent with the distance when the optical brightness is small for optical detection in ref. Nakamura et al. (2016). For other choices of distance, the flux and count rates will scale as $(10\mathrm{kpc}/\mathrm{D})^2$.

to peak at ∼100 days. Therefore, in the core model, we expect GBM could only observe ^{56}Co lines to detect the Galactic SNIa at a later time ∼ 20 days. Similar spectra and conclusions are also obtained for the NaI detector n3, the spectra plots are shown in Fig. 3.2.

We also simulate the spectra in BAT detectors at day 2, day 12 and day 24 in Fig. 3.3. BAT will not be able to detect ^{56}Ni 158 keV line for the core model as the ejecta is optically thick at early phase after the explosion. For the shell model, the on-axis signal amplitude of ^{56}Ni 158 keV line is ∼ 4-5 times larger than the average BAT background flux at day 12 after the explosion. But even at day 2, although the 158 keV signal is weak, BAT may still be able to detect the SN using the BAT image trigger (Krimm et al., 2013).

To conclude, if a SNIa were to explode at a distance of 10 kpc at our Galaxy, *Fermi*/GBM will be able to detect the signal as early as ∼ day 2 after the explosion if there is significant surface nickel, or no later than at ∼ day 50 for a pessimistic core model case. *Swift*/BAT can only see the ^{56}Ni 158 keV line, and thus requires surface nickel for detection. Moreover, if only GBM see the SNIa line signals other than 158keV line and BAT sees no line signal at the same time, this means that there is no surface ^{56}Ni in the SN ejecta. Thus, when a SNIa signal will emerge above the detector background depends upon (and probes) the mass and distribution of ^{56}Ni in the ejecta.

A SN detection would trigger a host of multi-wavelength observations. Speed and reliability of the alarm will be crucial. There are two possibilities of getting alert of a Galactic SN Ia: 1) BAT discovers the SN Ia first and localize it within arcminutes; 2) *Fermi* finds the SN Ia first and use the Earth occultation technique to localize it within degrees, shown in Fig. 3.4, follow up by BAT localization to within arcminutes. After the alert of either BAT or *Fermi*, *Swift* will turn to the SN and localize it to take spectra with both XRT and UVOT, and localize the SN with much better precision. For details of GBM and BAT localization (∼ arcseconds), see Methods.

A Galactic SNIa detection would uniquely advance our understanding on several fronts. 1) Type Ia explosions have been used as "standardizable" candles and thus cosmic distance

indicators, famously leading to the discovery of cosmic acceleration. Multi-wavelength observations of a Galactic Type Ia event would offer a powerful new probe of the Phillips relation used to standardize the lightcurves (Phillips, 1993). 2) The nature of Type Ia progenitors remains a mystery (single vs double degenerate scenarios). A Galactic SNIa would offer unique insight into the progenitor, e.g., via radio and X-ray probes of the circumstellar environment. 3) SNIa are also the dominant source of iron-group elements. *Swift*/BAT and *Fermi*/GBM observations will precisely measure the ^{56}Ni mass, and the lightcurves would encode a map of the structure and mixing of the ejecta.

Although a Milky Way SNIa is rare on human timescales, the potential scientific impact merits preparations–similar philosophy was recently vindicated by the spectacular GW170817 (Abbott et al., 2017). Luckily, our analysis shows that gamma-ray sky surveys–in the form of burst monitors or otherwise–serve as alarms if they have line sensitivity, without need for modifications in observing strategies. Our techniques can thus be applied to present and future gamma-ray missions, ensuring that we are prepared to welcome the next Galactic SNIa. This technique could also be generalized for long duration transients like solar flares (Fitzpatrick et al., 2012).

3.3 Methods

The procedure to conduct the research is following. First, build models for a SNIa's ejecta to calculate the curves and spectra of both ^{56}Ni and ^{56}Co decay from a Galactic SN Ia. Then simulate what the light-curves and spectra would look like in GBM and BAT detectors, respectively. Thirdly, compare the simulated Galactic SNIa signal with the typical background of the detector to see whether the signal is large enough to be noticed at early days and how soon we can confirm the signal is from a Galactic SNIa. Finally, after the confirmation of the signal, localize the SNIa with good accuracy in a short time using *Fermi* and *Swift*, and the followup multi-wavelength and multi-messenger observations.

3.3.1 Models

Here we build models that explore both the optimistic and pessimistic case of ejecta scenarios (shell plus core model and core only model). These will serve as inputs to the radiation transfer calculations, yielding the SNIa γ-ray light curves and spectra. To estimate the light curve and spectrum requires a model for the gamma-ray emission and transfer in the ejecta. Previous work made the assumption (plausible at the time) that SNIa are spherically symmetric and stratified, with ^{56}Ni buried deep in the core (e.g., Bussard et al., 1989). These calculations found that SNIa are opaque to gamma-rays for $\sim$100 days due largely to Compton scattering in the initially dense ejecta. If this were the case, then a Galactic SNIa would likely not be discovered until months after the explosion, delaying followup observations until well after the peak optical emission. Fortunately, *INTEGRAL* observations of SN2014J reported ^{56}Ni lines within $\sim$20 days after the explosion, far earlier than expected. This initial line flux corresponds to about 10% of the total expected ^{56}Ni mass (Diehl et al., 2014, 2015) at the surface (in fact, the proposed geometry has the nickel concentrated in a belt). Later observations firmly detected the ^{56}Co lines which imply an initial ^{56}Ni mass very close to $0.5M_{\odot}$ (Churazov et al., 2015).

We adopt a zeroth-order uniform ejecta model following ref.Bussard et al. (1989)'s work, where the electron number density profile $n_{\rm e}$ is assumed to be flat in radius and drops to zero at the outer radius of ejecta $a = a_0 + v_0 t$. Here a_0 is the ejecta radius at the explosion time, v_0 is the velocity at the outermost radius and is given by $v_0 = (10E_{\rm ej}/3M_{\rm ej})^{1/2}$, $M_{\rm ej}$ is the total mass of the debris, $E_{\rm ej}$ is the total kinetic energy ejected. Therefore the volume of the ejecta is $V = 4\pi a^3/3$, $n_{\rm e} = Y_{\rm e} n_{\rm b} = M_{\rm ej}/(\mu_{\rm e} m_{\rm p} V)$, where $n_{\rm b}$ is the baryon density, $Y_{\rm e}$ is the mean electron number per baryon, $m_{\rm p}$ is the proton mass. We adopt $M_{\rm ej} \sim M_{\rm Chandrasehkhar} = 1.4M_{\odot}$, and $Y_{\rm e} \approx 1/2$ here for a Galactic SNIa.

For uniform density ejecta, the mass density is just $\rho = \rho_{\rm Ni} = M_{\rm ej}/V_{\rm ej}$, therefore $n_{\rm Ni}/n_{\rm e} = (\rho_{\rm Ni}/m_{\rm Ni})/(Y_{\rm e}\rho/m_{\rm p}) = 1/Y_{\rm e}A_{^{56}{\rm Ni}}$. The ejecta is expanding homologously, i.e., $v(r) \propto r$, r is

the radius from the center $r \sim vt$.

The number emission coefficient for line E_i is

$$j = \frac{dN_i}{dtdVd\Omega} = b_i \frac{dN_{\rm Ni,or,Co}}{dtdVd\Omega} = b_i \frac{dn_{\rm Ni,or,Co}}{dtd\Omega} \tag{3.1}$$

where b_i is the branching ratio of the gamma-ray line at photon energy E_i. The Doppler effects are neglected here, which will broaden the decay lines but at a level below the resolution of *Fermi* and *Swift*.

The source function is

$$S = \frac{j}{n_{\rm e}\sigma} = \frac{b_i}{n_{\rm e}\sigma(E_i)} \frac{dn}{dtd\Omega} = \frac{b_i}{4\pi n_{\rm e}\sigma(E_i)} \frac{dn}{dt} \tag{3.2}$$

where,

$$\frac{dn_{\rm Ni}}{dt}|_{\rm decay} = \frac{n_{\rm Ni}|_{\rm decay}}{t_{\rm mean,^{56}Ni}} = \frac{n_{\rm Ni}|_{\rm decay}(t=0)}{t_{\rm mean,^{56}Ni}} e^{-t/t_{\rm mean,^{56}Ni}} = n_{\rm Ni}|_{\rm decay}(t=0) f_{\rm Ni}(t) \tag{3.3}$$

$$\frac{dn_{\rm Co}}{dt}|_{\rm decay} = \frac{n_{\rm Ni}|_{\rm decay}(t=0)}{t_{\rm mean,^{56}Co} - t_{\rm mean,^{56}Ni}} \cdot (e^{-t/t_{\rm mean,^{56}Co}} - e^{-t/t_{\rm mean,^{56}Ni}}) = n_{\rm Ni}|_{\rm decay}(t=0) f_{\rm Co}(t) \tag{3.4}$$

To avoid confusion with optical depth τ, we use $t_{\rm mean,^{56}Ni} = 8.8{\rm days}, t_{\rm mean,^{56}Co} = 111.3{\rm days}$ for the mean lifetime of the radioactive ^{56}Ni and ^{56}Co,respectively. $\sigma(E_i)$ is the cross-section when photons propagate through the dense material of the ejecta (use ^{56}Co as an estimation), including coherent scattering (Klein Nishina cross section) and incoherent scattering, photoelectric absorption, and pair production, values adopted from XCOM website [5]

Therefore the source function can be written as

$$S = b_i \frac{X_{^{56}\rm Ni}}{4\pi\sigma A_{^{56}\rm Ni} Y_e} f_{\rm Ni,or,Co}(t) \tag{3.5}$$

[5] `https://www.nist.gov/pml/xcom-photon-cross-sections-database`

where $X_i = A_i Y_i$, $Y_i = n_i/n_b$, and $\sum X_i = 1$. Let x_i to be the ionization fraction of nuclei i, then $Y_e = \sum x_i Z_i Y_i = \langle xZ/A \rangle \approx \langle x \rangle /2$. For a fully ionized shell of pure ^{56}Ni, we obtain a ratio $n_{^{56}\mathrm{Ni}}/n_e = X_{^{56}\mathrm{Ni}}/(A_{^{56}\mathrm{Ni}} Y_e) \approx 2/A_{^{56}\mathrm{Ni}}$.

If S is constant, from the radiative transfer equation $dI/d\tau = -I + S$, we can get the intensity to be

$$I(\tau) = I(0)e^{-\tau} + S\int_0^\tau e^{-(\tau-\tau')}d\tau' = I(0)e^{-\tau} + S(1-e^{-\tau}) \tag{3.6}$$

where optical depth $\tau = \int n_{\mathrm{e}}(r)\sigma dl = n_{\mathrm{e}}\sigma a \cdot (l/a) = \tau_a \cdot l/a$.

Let θ to be the angle between line of sight and the line between ejecta center and observer, thus total flux from the ejecta should be an integral of the intensity over the solid angle extended by the ejecta, i.e.,

$$F = \int I cos\theta d\Omega \approx 2\pi \int I\theta d\theta \tag{3.7}$$

For a shell plus core model (shortened as shell model thereafter), motivated by SN2014J (Diehl et al., 2014) and ignoring the Compton continuum emission, we assume total ^{56}Ni mass $M_{^{56}\mathrm{Ni,total}} = 0.5M_\odot$ with 10% of the mass distributed at the outmost shell of the ejecta with radius a and depth h, while the remain Ni is in the core with radius R_0 and subtended angle $\theta_0 \sim R_0/D$, where D is the distance between the earth and the SNIa. The angle subtended by the shell is between $\theta_1 \sim (a-h)/D$ and $\theta_2 \sim a/D$. Thus the ejecta emission is in the region between $\pm\theta_2$. Sketch of the shell model see Fig. 3.5.

For $\theta_1 \leq \theta \leq \theta_2$, the photon pathlength is $l_2 = 2\sqrt{a^2 - (D\theta)^2}$, the intensity is

$$I_2 = S(1 - e^{-\tau_a \cdot l_2/a}). \tag{3.8}$$

For $\theta_0 \leq \theta \leq \theta_1$, photon will travel two different regions through the line of sight,

$l_1 = \sqrt{a^2 - (D\theta)^2} - \sqrt{(a-h)^2 - (D\theta)^2}$, $s_1 = 2\sqrt{(a-h)^2 - (D\theta)^2}$, the intensity is

$$I_1 = S(1 - e^{-\tau_a \cdot l_1/a}) \cdot (e^{-\tau_a \cdot (s_1+l_1)/a} + 1). \quad (3.9)$$

For $0 \leq \theta \leq \theta_0$, photon will travel three different regions through the line of sight, $l_0 = 2\sqrt{R_0^2 - (D\theta)^2}, s_0 = \sqrt{(a-h)^2 - (D\theta)^2} - \sqrt{R_0^2 - (D\theta)^2}$, the intensity is

$$\begin{aligned} I_0 &= S(1 - e^{-\tau_a \cdot l_1/a}) \cdot e^{-\tau_a \cdot (2s_0+l_0+l_1)/a} + S(1 - e^{-\tau_a \cdot l_0/a}) \cdot e^{-\tau_a \cdot (s_0+l_1)/a} \\ &\quad + S(1 - e^{-\tau_a \cdot l_1/a}). \end{aligned} \quad (3.10)$$

Therefore, the flux for shell model is

$$F_{\rm shell}(E_i, t) = 2\pi(\int_0^{\theta_0} I_0 \theta d\theta + \int_{\theta_0}^{\theta_1} I_1 \theta d\theta + \int_{\theta_1}^{\theta_2} I_2 \theta d\theta). \quad (3.11)$$

Similarly, for a core only model where all the Ni is distributed in the core with radius R_0 ($h = 0$ in the shell model case), the flux is

$$F_{\rm core}(E_i, t) = 2\pi(\int_0^{\theta_0} I_0 \theta d\theta + \int_{\theta_0}^{\theta_1} I_1 \theta d\theta). \quad (3.12)$$

with $\theta_1 = \theta_2 = a/d$.

3.3.2 Analytical formulas

Analytical formulas for SNIa flux can be obtained in the limits of optical depth τ_a.

1)When the ejecta is optically thick $\tau_a \gg 1$, the flux for shell model is

$$F(E_i, t) = \pi S \frac{a^2}{D^2} = \frac{b_i X_{^{56}\rm Ni}}{4 A_{^{56}\rm Ni} Y_e \sigma} \frac{a^2}{D^2} f_{\rm Ni,or,Co}(t). \quad (3.13)$$

which is only determined by the surface ^{56}Ni abundance $X_{^{56}\rm Ni}$, ionization status Y_e and

surface velocity. This equation fits our simulation perfectly at early time, shown in the right panel in Fig. 3.7. Therefore for a certain SNIa, at early times when the ejecta is optically thick, there is an accurate analytical relation between $X_{^{56}\mathrm{Ni}}$ and the detected time t_{detected}, defined as when the SN line signal is about the same as the detector background signal:

$$X_{^{56}\mathrm{Ni}} = \frac{A_{^{56}\mathrm{Ni}} Y_e \sigma}{b_i} \frac{4D^2}{a^2} \frac{F_{\mathrm{background}}(E_i, t_{\mathrm{detected}})}{f_{\mathrm{Ni,or,Co}}(t_{\mathrm{detected}})} \tag{3.14}$$

which is shown in Fig. 3.6 for GBM/BGO detection. For a "uniform mixing" scenario, i.e., ^{56}Ni is uniformly distributed in the spherical ejecta with $X_{^{56}\mathrm{Ni}} \sim 35.7\%$, the ^{56}Ni 158keV signal can be seen as early as $\sim$ day 3. So a SNIa signal is able to be seen at early time, as long as the surface ^{56}Ni abundance is at least a few percent, and may be distributed in any shape, e.g., a "plume".

2)When the ejecta is optically thin $\tau_a \ll 1$, the flux is

$$\begin{aligned} F(E_i, t) &= \frac{b_i}{4\pi D^2} \frac{dN_{\mathrm{Ni,or,Co}}}{dt} \\ &= \frac{b_i}{4\pi D^2} \frac{M_{Ni}}{A_{^{56}\mathrm{Ni}} m_p} f_{\mathrm{Ni,or,Co}}(t) \end{aligned} \tag{3.15}$$

which only depends on the total ^{56}Ni mass $M_{^{56}\mathrm{Ni}}$ of the SNIa. Thus for a certain SNIa, with whatever ejecta distribution, the line flux is always the same when the ejecta is optically thin.

3.3.3 Lightcurves

The goal of GBM and BAT is to identify transients like the gamma-ray bursts that exceed the background emission. A typical gamma-ray burst rise timescale is a few seconds, for which GBM and BAT triggering is optimized. But the signal from a Galactic SNIa rise and decay lasts weeks ($t_{\mathrm{mean},^{56}\mathrm{Ni}} = 8.8\mathrm{days}, t_{\mathrm{mean},^{56}\mathrm{Co}} = 111.3\mathrm{days}$), meaning the Galactic SNIa signal will appear as a long-duration increase in the background, instead of triggering the

detector. So we need to compare our simulation of light curves and spectra from a Galactic SNIa with the background of GBM and BAT detectors to check whether the signal is large enough to be noticed and how soon we can confirm a Galactic SNIa after its explosion and sound the alarm. Discussions of BGO and BAT background see the following discussion section.

Fig. 3.7 shows the simulated SNIa light curves of both ^{56}Ni decay lines (the dominant 158 keV and 812 keV lines) and ^{56}Co decay line (the dominant 847 keV line), for both the shell model and core model. For the optimistic case (shell model), we can see that the line fluxes from ^{56}Ni decay will exceed the BGO background at first few days after the explosion and reach the peak at $\sim$ 10 days when the fluxes are $\gtrsim$ 4-5 times higher than the background. Therefore, if the shell model is true, the ^{56}Ni decay signal from a Galactic SNIa will be noticed as early as first days after the explosion. Although ^{56}Co decay line fluxes are much smaller compared to ^{56}Ni at early days, they still exceed the BGO background flux at $\sim$ 8 days and reach the peak at $\sim$ 100 days. For the most pessimistic case (core model), the ejecta remains optically thick at first tens of days after the explosion, thus ^{56}Ni lines will be too weak to be observed by the detector. Also ^{56}Co lines will emerge much later than the shell model case, after $\sim$ 20 days. Then ^{56}Co lines will reach the peak at a similar time and evolve to be the same as the shell model at later time, with the same total ^{56}Ni mass. Similar conclusions will be obtained for the ^{56}Ni 158keV line observed by BAT detectors with a similar background flux at the 158keV bin. In addition, the right panel in Fig. 3.7 show that the analytical formula eq 3.13 fits the simulated light curves perfectly at a few days when the ejecta is optically think, meaning that we could predict accurately the line signal from a Galactic SNIa at early days after the explosion and the observations will give important information about the ejecta.

3.3.4 Localization

Because *Fermi* orbits the Earth with an altitude 555 km $\sim 10\% R_{\oplus}$, about 30% of *Fermi*'s field of view is always blocked by the Earth. About 85% of the sky is occulted in one orbit, so that point sources will typically be eclipsed once per orbit, as seen in Fig. 3.4. From the eclipse flux decrement and timing, sources can be identified and located. The Earth Occultation Technique and Earth Occultation Imaging have been successfully used to search for known and unknown point sources for GBM (Wilson-Hodge et al., 2012; Rodi et al., 2014). The occultation duration will depend on the elevation angle β between the source and the orbital plane. The angular resolution ranges from $\sim 0.5^{\circ}$ for $\beta = 0$ to $\sim 1.25^{\circ}$ for $\beta = 66^{\circ}$, and the timescale of localization is ∼P, where $P = 96$ minutes is *Fermi*'s orbital period. For $\beta > 66^{\circ}$, occultation does not occur, GBM need to wait to precess to another orbit to have signal blocked.

BAT may be the first, perhaps the *only* way to detect a Galactic SN Ia simultaneously in both X-ray and UV and optical bands. *Swift* BAT has PSF of 22.5 arcmin for an on-axis source (Tueller et al., 2010), this alone is good enough to be easily within the field of view (FOV) for many ground-based optical/IR telescopes such as DECam on the *Dark Energy Survey*, and later *LSST* When BAT will find the SNIa depends on when it happens to be in its FOV, and thus on the *Swift* scan strategy. A Galactic SNIa could also be seen at other wavelengths. If there is an X-ray signal, *Swift*/XRT precision is good to about 1 pixel or ~ 2.4 arcsec. If *Swift*/UVOT sees a signal, the precision is similar, which will be in the FOV of all optical/IR telescopes. But UVOT is difficult to localize the Galactic SN due to the crowdedness of stars and bright sources in the Galactic plane. Therefore after BAT discover the Galactic SNIa, XRT will followup to confirm the SN and localize it with a relatively cleaner background. If there is no X-rays seen, UVOT will be used to localize the SN with white filter, finally take the spectra with both UV and optical filters.

3.3.5 Discussion

Both the GBM and BAT detectors' background and response files are from HEASARC site, processed with `Xspec`. [6]. Background files are selected from typical GBM (cspec files) and BAT daily files for a particular detector when the satellite is looking at the Galactic center.

As the two BGO detectors and 12 NaI detectors mounted on GBM are pointing at different direction, if a SNIa signal is seen in one detector, other detectors are expected to observe the similar signal with phase delay. BAT background file is the total background signal measured by all the active detectors. We have included both the mask effect and the detector degrading effect. For an on-axis signal, half of the detectors are masked by the coded aperture mask. And the active detectors of BAT are decreasing with time (Lien et al., 2016), therefore we use recent background signal (2017 year) and 50% as the active detector percentage (current active detector ratio is $\sim$ 56%) for a fair comparison. When BAT is looking at the Galactic center, its FOV is $\pm$ 20 degree along the long axis. For our simulations, the 26.56 deg off-axis signal is $\sim$ 90% of the on-axis signal from same Galactic SNIa, thus we estimate the off-axis effect will decrease $\sim$ 10% of the supernova signal.

Any supernova signal in the GBM and BAT must compete with the (time varying) gamma-rays background always present. Above $\sim$150 keV, the background sources are dominantly secondary gamma rays created by cosmic-ray interactions in the Earth's atmosphere, and in the spacecraft itself (Meegan et al., 2009). The average variations of both GBM and BAT background over one orbit are about $\sim$ 50% (Fitzpatrick et al., 2012; Ajello et al., 2008), due to the variation of cosmic-ray flux densities in the atmosphere. Although the background is dominated by cosmic rays, which are affected by solar activity, we find that the variations over years or solar cycle is quite small ($\lesssim$ 20%), based on our crude analysis of the detectors' daily data from different years. The background variation analysis here exclude orbits passing the South Atlantic Anomaly (SAA). These background variations can

[6] `http://heasarc.gsfc.nasa.gov/xanadu/xspec/,\http://heasarc.gsfc.nasa.gov/FTP/fermi/data/gbm/,ftp://legacy.gsfc.nasa.gov/swift/calib_data/bat/`

be seen as a noise source that is much larger than, and in addition to, the detectors' background errors in each exposure due to counting statistics. Therefore we require that SNIa signal/background $\sim$1 for discovery or detection, which we believe is a good first approximation and a safe, conservative approach when one does not know the background level at the time of the possible discovery.

Accounting for all these effects, SNIa signal will still be detectable by both GBM and BAT within several days after explosion if there is significant surface ^{56}Ni in the SNIa. If there is not, we will have to wait weeks. The uncertainty of surface ^{56}Ni abundance dwarfs these other concerns.

With advanced technique, it's possible that there is a better and more precise criteria for "detectable". For example, comparing the background after 15 and 30 orbits to diminish the GBM orbital variations (Fitzpatrick et al., 2012), when the satellite is over the same part of the Earth in latitude and longitude. Even then there are worries about variations in photomultiplier gain. BAT will perhaps do a better job for early signal detection, especially using the image trigger technique (Krimm et al., 2013). For example, if BAT looks at the Galactic center daily for a snapshot $\sim 10^3$s, the 5σ noise flux level around 158keV is $\sim 3.5\times10^{-3}\mathrm{s}^{-1}\mathrm{cm}^{-2}$ (Baumgartner et al., 2013), which is far smaller than the SNIa signal at first day. However, the potential detection difficulties are the imaging and localization limit of BAT at high energy (around 150-200 keV) and possible low surface ^{56}Ni abundance of the SNIa. So while better detection criteria is for sure interesting, it is a big job to develop and test the strategy, and beyond the scope of this paper.

We only consider the nuclear lines emitted from SNIa (zero-scattered photons from the ^{56}Ni and ^{56}Co decay) here for a conservative analysis of the SNIa observation. In addition, the instrumental effect introduces "fake" continuum in the simulated spectra, dominant over the continuum due to Compton scattering (the simulation of detected lines are much wider than the theoretical lines). The signal will be enlarged if the Compton continuum is included (adding scattered photons), making the signal easier to detect. The instrumental effect also

brings "fake" flux at $\sim$ 100-200 keV from the ^{56}Co lines at higher energy at later time $\sim$ 100 days, making the signal even exceeding the background at lower energy, shown in Fig. 3.1.

Based on our simulations of SNIa spectra and light curves, indeed, even for an extreme distance of 20 kpc, the signal will eventually be detectable (e.g., at $\sim$ day 12 for the shell model). Thus essentially any Galactic SNIa will be detectable by *Fermi* and *Swift*. Obviously, the closer the event, the sooner its gamma signature will emerge.

3.4 Acknowledgments

BDF thanks Raph Hix for conversations that inspired this work. We are also pleased to acknowledge fruitful conversations with John Beacom, Valerie Connaughton, Ryan Foley, Athol Kemball, Sylvain Guiriec, Shunsaku Horiuchi, Kenny C.Y. Ng, and Paul Ricker. This work benefited from discussions at the 2018 Frontiers in Nuclear Astrophysics Conference supported by the National Science Foundation under Grant No. PHY-1430152 (JINA Center for the Evolution of the Elements). This work was supported in part by the NASA Swift GI program, grant NNX16AN81G.

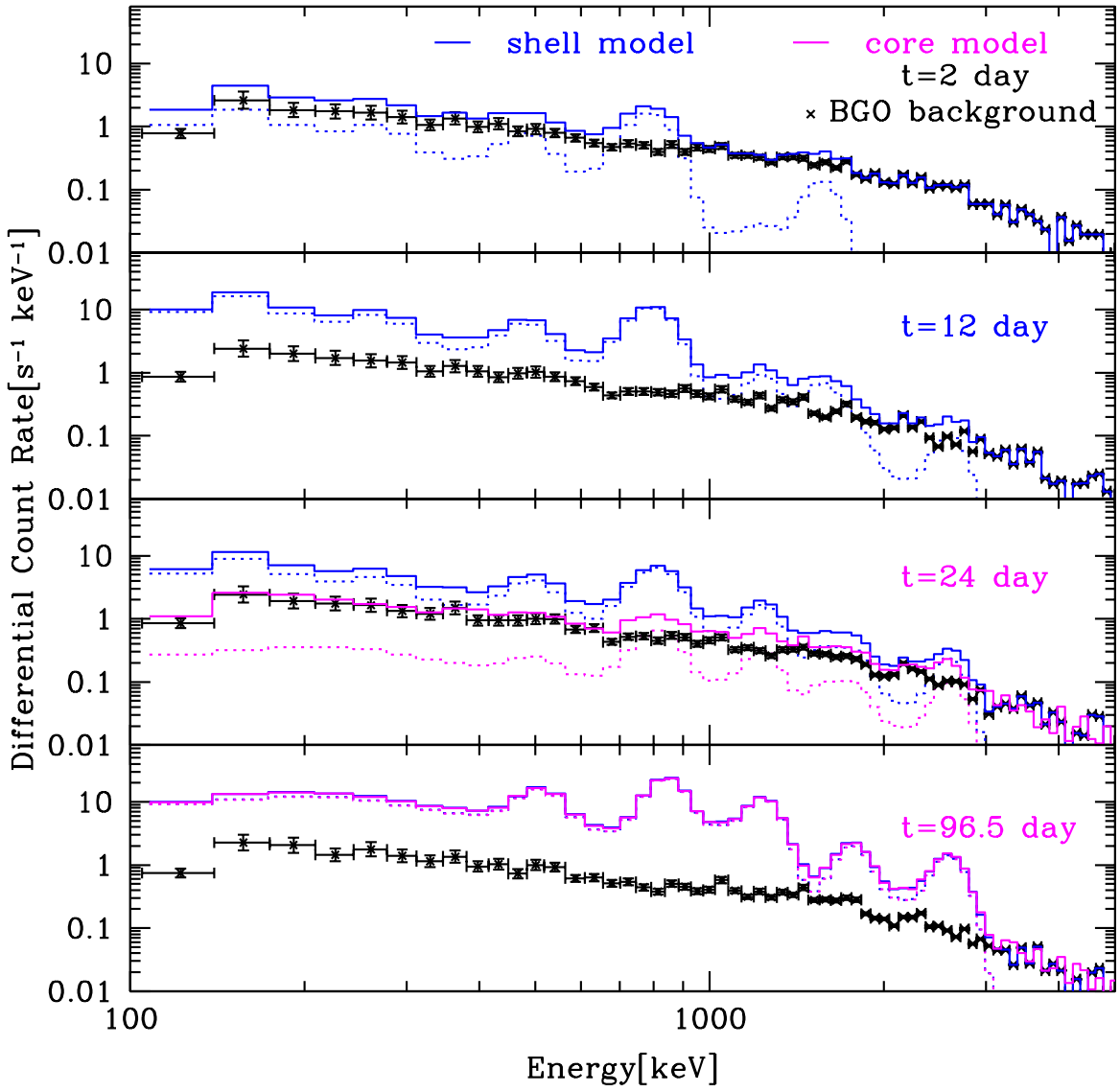

Figure 3.1: Simulation of ^{56}Ni and ^{56}Co gamma-ray lines signal seen in a GBM/BGO detector, from a 10 kpc Galactic SNIa after 2 day (above), 12 day (middle above), 24 day (middle below) and 96.5 day (below) of its explosion. The black points represent a typical background spectrum from detector b1. Dotted lines are the simulated SNIa ^{56}Ni and ^{56}Co decay lines signal, and solid lines are the total signal expected to be seen by the detectors (sum of the background and SNIa signal). Blue lines are for shell model, magenta are for core model.

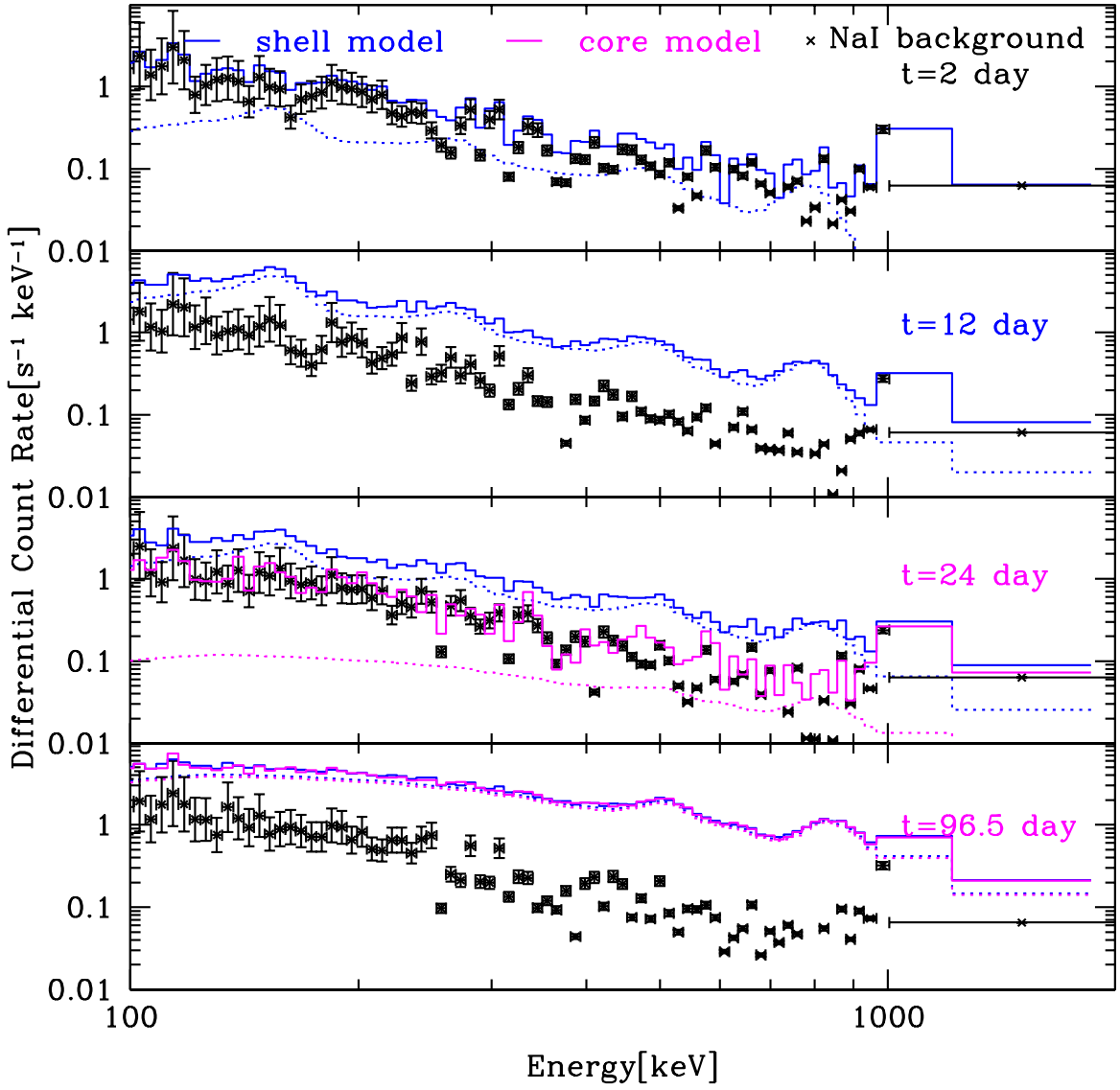

Figure 3.2: Simulation of ^{56}Ni and ^{56}Co gamma-ray lines signal seen in a GBM NaI detector, from a 10 kpc Galactic SNIa after 2 day (above), 12 day (middle above), 24 day (middle below) and 96.5 day (below) of its explosion. The black points represent a typical background spectrum from detector n3. Dotted lines are the simulated SNIa ^{56}Ni and ^{56}Co decay lines signal, and solid lines are the total signal expected to be seen by the detectors (sum of the background and SNIa signal). Blue lines are for shell model, magenta are for core model.

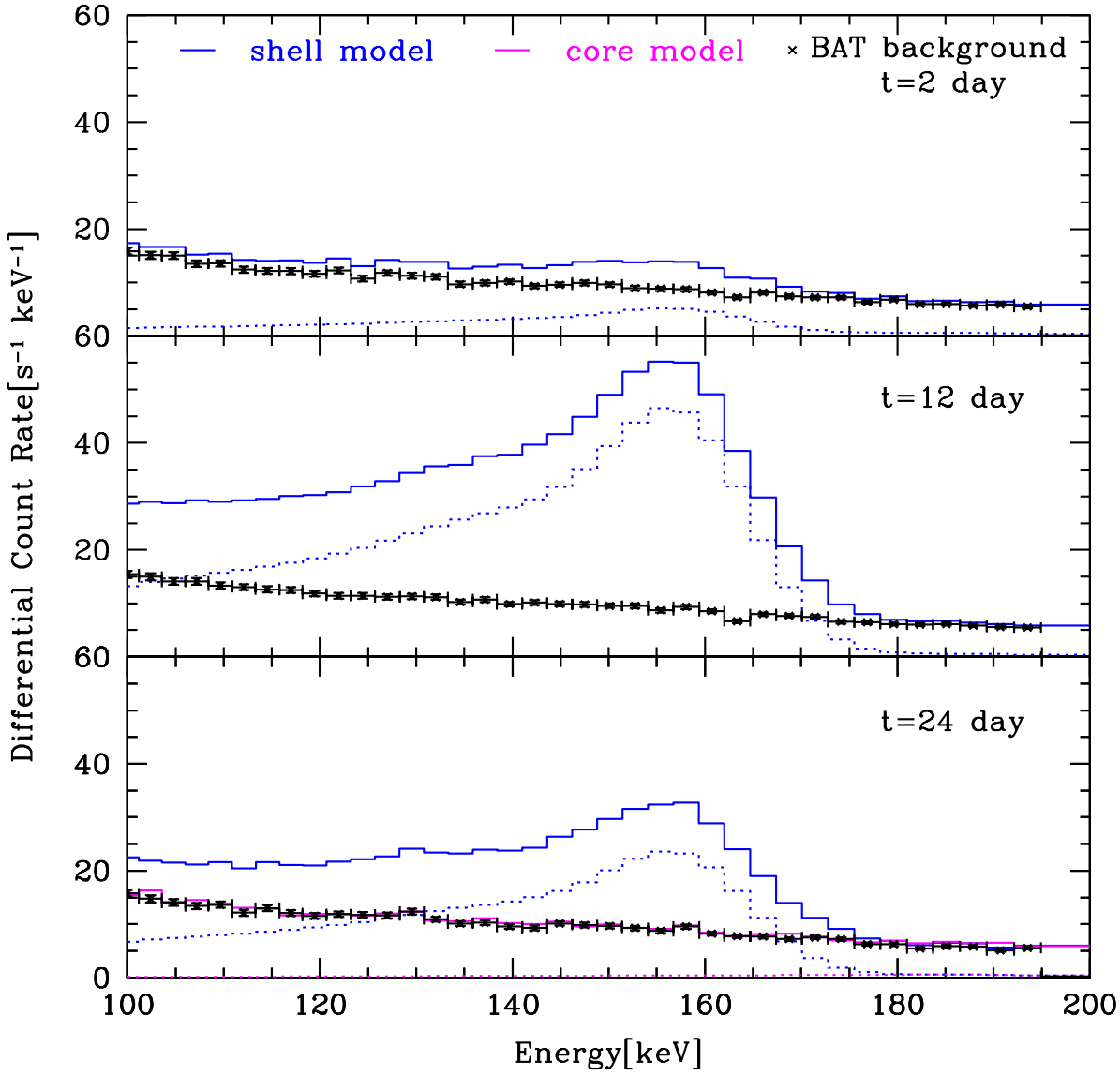

Figure 3.3: Simulation of on-axis ^{56}Ni and ^{56}Co gamma-ray lines signal seen in BAT detector, from a 10 kpc Galactic SNIa after 2 day (above), 12 day (middle) and 24 day (below) of its explosion. The black points represent a typical background spectrum from BAT detectors. Dotted lines are the simulated SNIa ^{56}Ni and ^{56}Co decay lines signal, and solid lines are the total signal expected to be seen by the detectors (sum of the background and SNIa signal). Blue lines are for shell model, magenta are for core model.

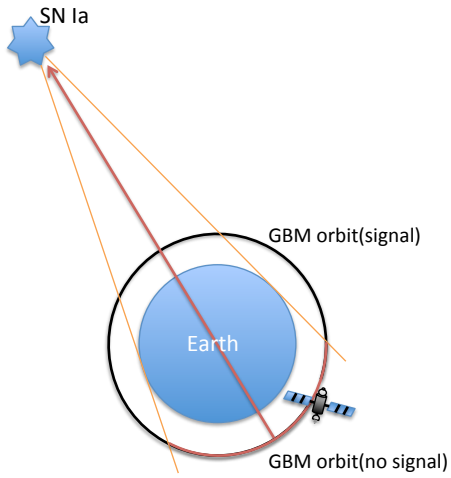

Figure 3.4: Sketch of how the Earth occultation technique localizes a Galactic SNIa. The signal will be occulted by the Earth during one orbit of the satellite, and the source position can be found by associating the occulting time and the satellite position.

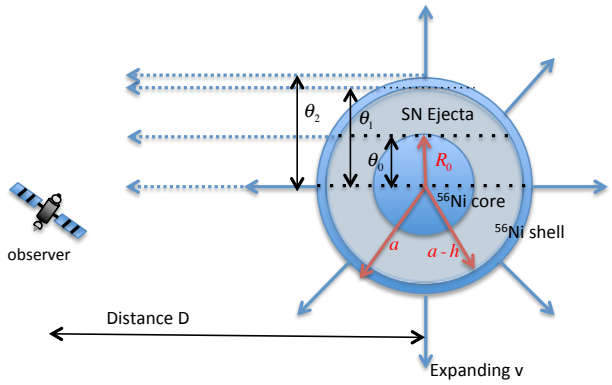

Figure 3.5: Sketch of the shell plus core model (shell model). For this model, ^{56}Ni is distributed at both the ejecta's outmost shell (10% of the mass) with depth h, and the inside core with radius R_0. The ejecta radius is a, the distance between the earth and the SNIa is D.

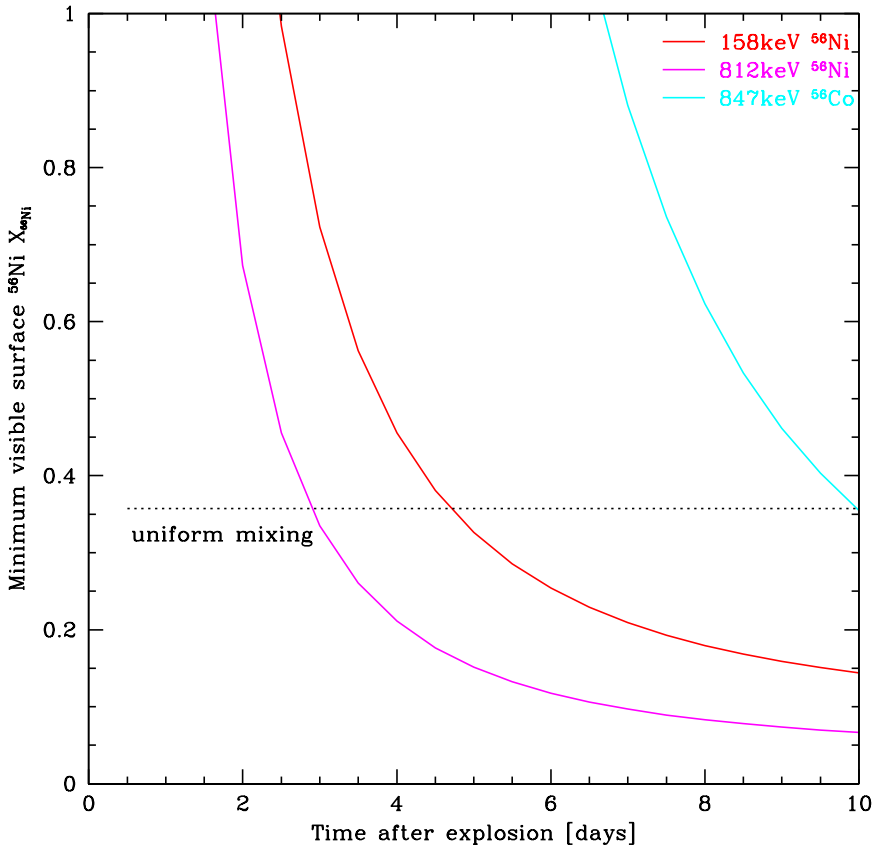

Figure 3.6: Minimum surface ^{56}Ni abundance $X_{^{56}\mathrm{Ni}}$ versus the detected time for a 10 kpc Galactic SNIa.

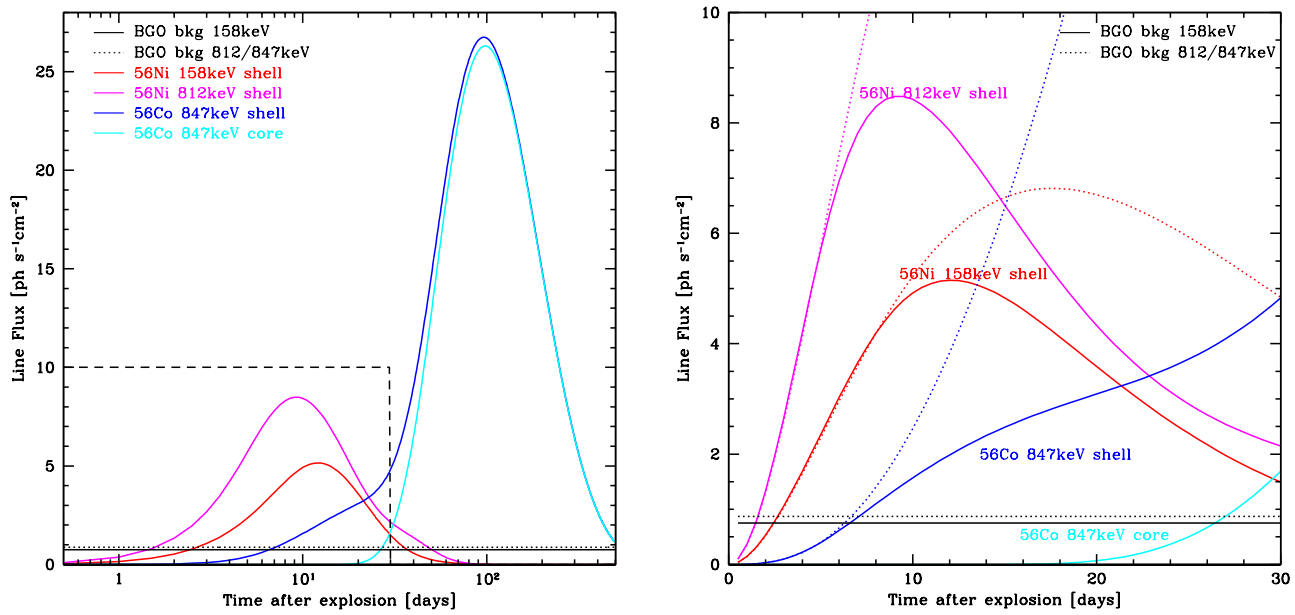

Figure 3.7: Simulated light curves of the gamma-ray lines from a 10 kpc Galactic SNIa. Black solid line is the average background flux measured in 158 keV bin of the BGO detector, black dotted line is background in 812/847 keV bin. Solid color lines are the simulation results, while dotted color lines are the analytical optically thick results (eq 3.13). Red lines are the ^{56}Ni 158 keV line signal intensity variation for the shell model, and magenta for the 811 keV lines. Blue lines are the ^{56}Co 847 keV line signal intensity variation for the shell model and cyan is the 847 keV line for the core model. Left panel: Light curves ranging in 500 days. Right panel: Light curves ranging in 30 days, which is the black dashed region in left panel.

Chapter 4

Conclusions

In this chapter, I will summarize the main preliminary results from my current work and discuss possible future prospects.

4.1 Preliminary and Future Work in Starburst Galaxies

4.1.1 The Extragalactic Gamma-ray Background Emission From Star-forming Galaxies

A main future work is to apply our "thick-target" model built in Chapter 2 to the diffusive extragalactic gamma-ray background emission (EGB).

4.1.1.1 Introduction

Star formation inevitably produces cosmic rays (via supernova explosions), and in turn cosmic-ray propagation through the interstellar medium unavoidably produces gamma rays (e.g., Pavlidou & Fields, 2001). Therefore all star-forming galaxies should be cosmic-ray accelerators and thus gamma ray emitters. Fermi observations have broadly confirmed these theoretical expectations. Fermi has mapped the LMC, detected two other normal star-forming galaxies, and detected or seen evidence for six starburst galaxies. These Fermi detections are limited to the nearest star-forming galaxies. All others–comprising nearly the

This section derives from a Fermi proposal written by Wang, X., & Fields, B.

entire star-forming universe–are too faint to be individually detected by Fermi. Thus, the overwhelming majority of star-forming galaxies are guaranteed but unresolved Fermi sources.

All the unresolved extragalactic gamma-ray sources can contribute to EGB (e.g., Dermer, 2007; Stecker & Venters, 2011). Studies by a number of other groups have verified the importance of star-forming galaxies for the EGB (e.g., Ackermann et al., 2015; Stecker & Venters, 2011; Ajello et al., 2015; Linden, 2017). Estimates for the intensity and spectrum are broadly similar across groups, but span a substantial factor. Starbursts have higher star formation rates and gas densities which will enhance the gamma-ray emission, so they can also contribute to the EGB (e.g., Thompson, Quataert and Waxman, 2007). Recent studies find the contribution of starburst galaxies to EGB in GeV range varies from 1% to 50% (e.g., Lacki et al., 2011; Stecker & Venters, 2011; Lamastra et al., 2017).

In the meantime, Fermi has presented a new EGB measurement (Ackermann et al., 2015). This observation spans the energy range from 100 MeV to 820 GeV, now probing the pion bump at low energies, and at high energies detecting the attenuation due to $\gamma\gamma \rightarrow e^+e^-$ absorption on the extragalactic background light. The EGB spectrum can be well fitted by a power law with exponential cutoff, having a spectral index 2.32 ± 0.02 and a break energy of (279 ± 52)GeV (Ackermann et al., 2015). The emerging picture is that the EGB is consistent with the "guaranteed" signal arising from unresolved counterparts of known sources–blazars/radio galaxies, and star-forming galaxies (e.g., Ajello et al., 2015). The data at present suggest a 30% contribution from star-forming galaxies, but with large uncertainties.

Thus, the time is ripe for a thorough analysis of the star-forming contribution to the EGB. We will perform a comprehensive calculation that includes all aspects of star-forming emissions: normal and starburst galaxies, hadronic and leptonic processes, core-collapse and thermonuclear supernovae; our models will be calibrated to Milky-Way diffuse emission and supernova data, and to resolved star-forming galaxies.

4.1.1.2 Method

As the thick-target model for the gamma-ray emission from individual starburst galaxy has been established in Chapter 2, we can proceed to calculate the pionic contribution to the EGB measured by Fermi in calorimeter case by the expression:

$$\frac{dI}{dE} = \frac{c}{4\pi} \int (1+z) \mathcal{L}_\gamma[(1+z)E_\gamma, z] \left| \frac{dt}{dz} \right| dz \tag{4.1}$$

where $|dt/dz| = (1+z)^{-1} H(z)^{-1} = H_0^{-1}(1+z)^{-1}[(1+z)^3\Omega_{\rm M} + \Omega_\Lambda]^{-1/2}$, assuming a ΛCDM universe with $H_0 = 71 km s^{-1} Mpc^{-1}$, $\Omega_{\rm M} = 0.3$,and $\Omega_\Lambda = 0.7$ (Fields et al., 2010).

The pionic luminosity density follows from the gamma-ray luminosity per galaxy L_γ:

$$\begin{aligned} \mathcal{L}_\gamma(z) &= \langle L_\gamma n_{\rm gal} \rangle \equiv \int L_\gamma \frac{dn_{\rm gal}}{dL_\gamma} dL_\gamma \\ &= \int \frac{L_\gamma}{\psi} \psi \frac{dn_{\rm gal}}{dL_\gamma} dL_\gamma = \frac{L_\gamma}{\psi} \dot{\rho}_*(z) \end{aligned} \tag{4.2}$$

where $n_{\rm gal}$ is the co-moving number density of gamma-ray-luminous galaxies, $\dot{\rho}_* = \langle \psi n_{\rm gal} \rangle = \int \psi dn_{\rm gal}/dL_\gamma dL_\gamma$ is the cosmic star formation rate, here assuming all the star-forming galaxies are in the calorimetric case.

Equation 2.13 shows that L_γ/ψ is constant and independent of redshift, therefore it comes out of the integral and the overall amplitude of the cosmic pionic calorimetric luminosity density is linearly proportional to the cosmic star formation rate. We will adopt the Horiuchi et al. (2009)'s cosmic star formation rate as Fields et al. (2010).

Assuming all gamma-ray luminous galaxies are calorimetric and use equation 4.2 we can calculate the pionic calorimetric contribution to the EGB, with $\epsilon_{\rm sn} = 0.1 foe$ and source proton spectral index $s = 2.2$ and 2.4. As our model gives an upper-limit to the pionic contribution, the final results can test whether EGB can come from starbursts alone. By varying the redshift of starburst in the calculation, we can evaluate the redshift's effects on the contribution of starbursts to EGB. Finally, by quantifying the difference of the extra-

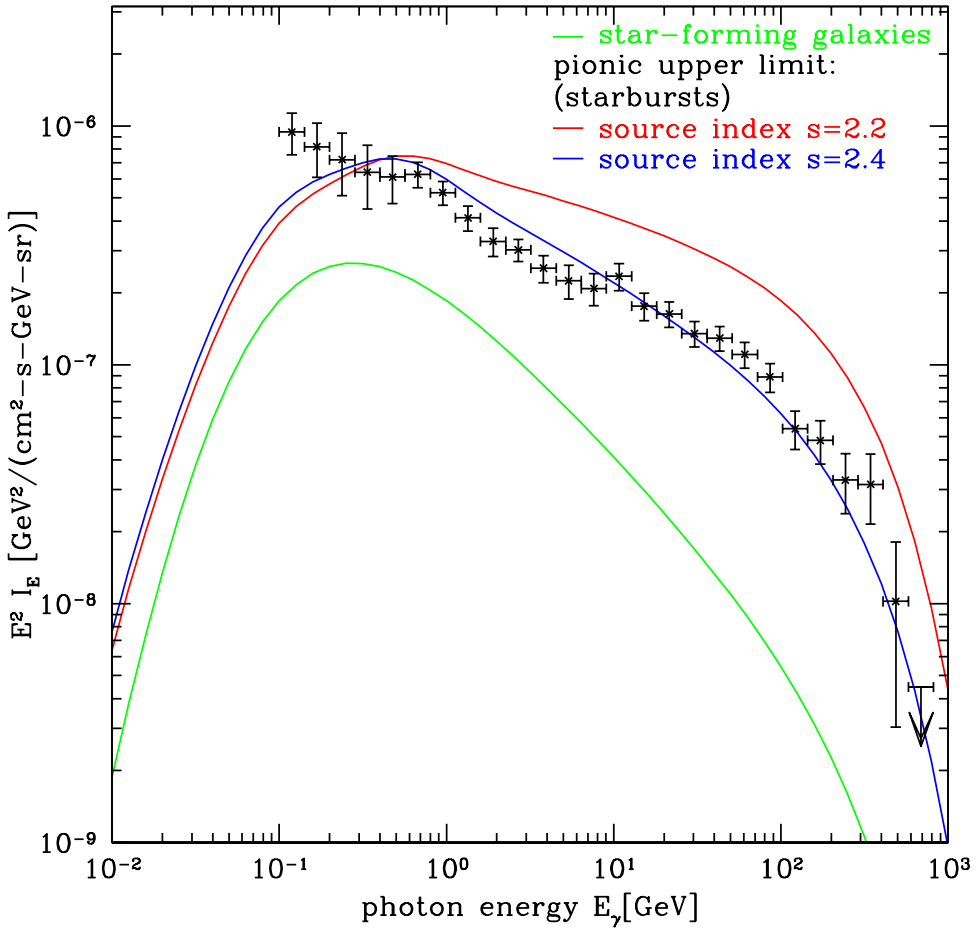

Figure 4.1: The observed EGB and pionic contribution from star-forming galaxies. Green: Fields et al. (2010) calculation assuming only contributions from ordinary star-forming galaxies. Red and blue: upper limit to EGB assuming all galaxies are calorimetric starbursts and thus maximally efficient emitters. Black points: Fermi/LAT EGB measurements Ackermann et al. (2015).

galactic gamma-ray flux between calculated and observed value, we will manage to constrain cosmic-ray properties of star-forming galaxies in the universe (the percentage of starbursts of all star-forming galaxies or the percentage of cosmic rays in star-forming galaxies which "die" in collisions).

Then we will perform a comprehensive calculation of the star-forming EGB. Fields et al. (2010) calculated the EGB for the case of normal star-forming (i.e., not starburst) galaxies: Fig. 4.1, green curve. It is assumed that in these galaxies, cosmic rays are escape-dominated as in the Milky Way. We see that the pionic star-forming component: (a) has a character-

istic feature which reflects the peaked pionic source spectrum, and (b) is a significant EGB component, but also (c) has a spectrum that at high energies is a power law with the same index as the underlying propagated cosmic rays, here s= 2.75. EGB data reveal a shallower index, with $s = 2.32 \pm 0.02$ (Ackermann et al., 2015). Furthermore, the peaked nature is not reflected in the two lowest data points, which will play a critic role in constraining the star-forming component. Indeed, the pionic peaked shape is unlike that of the other guaranteed EGB component, active galaxies, suggesting that these sources could play an important role.

Pavlidou & Fields (2002) showed that a normal galaxy's luminosity from cosmic-ray interactions with the interstellar medium depends on the cosmic-ray flux $\Phi_{\rm cr}$ and the total number of targets given by the interstellar gas mass $M_{\rm gas}$; thus $L_\gamma \propto \Phi_{\rm cr} M_{\rm gas}$. Fields et al. (2010) builds on this, in the cosmological context of mass/baryon accretion, using observed distributions of star formation rates (Madau et al., 1996; Hopkins, 2004), and incorporating the empirical Schmidt-Kennicutt Kennicutt (1998) correlation between star formation and gas content.

Fields et al. (2010) ignored starburst galaxies, which are rare at low redshifts but become increasingly dominant at high redshifts. Wang & Fields (2018) (Chapter. 2) has developed a self-consistent model for starburst galaxies as partial or nearly total calorimeters. In these dense systems, cosmic ray losses are dominated by interactions rather than escape, and a large fraction of the injected cosmic-ray energy is ultimately emitted in gamma rays. Thus the gamma-ray luminosity is maximal for a given supernova or star-formation rate. Moreover, Wang & Fields (2018) showed that the resulting gamma-ray high-energy spectrum is a power law whose index reflects the injected cosmic-ray index and thus is flatter than in the normal galaxy case.

For all of these reasons, it is critical to carefully explore the starburst galaxy contribution to the EGB. To give an extreme example, the blue and red curves in Fig. 4.1 show the result if all star-forming galaxies were calorimetric. We see that the resulting gamma-ray signal is substantially boosted in intensity, with a notably flatter slope. This extreme case obviously

represents and upper limit. Thus, in a realistic model that includes a mix of starburst and normal galaxies, we expect the EGB signal to be bracketed by the curves in Fig. 4.1.

Star-forming galaxies also emit leptonically due to cosmic-ray electrons. At higher energies of Fermi observation, this is dominated by inverse Compton emission, modeled by Chakraborty & Fields (2013). At lower energies, bremsstrahlung contributes, as modeled by Foreman et al. (2015). We will include both components self-consistently.

Finally, Type Ia supernovae also serve as cosmic-ray accelerators. Lien & Fields (2012) examined this problem in detail, and produced models for self-consistently including the Type Ia supernova contributions to the cosmic star-forming emissivity. We will use these models and extend them to the cases of leptonic emission and starburst galaxies.

We will systematically combine these components of the cosmic star-forming gamma luminosity, and study their interrelations and the dependence on model inputs such as injection index, scaling between star formation rate and gamma-luminosity, and on the treatment of starburst evolution over time. This will yield the most comprehensive study to date. We will characterize the uncertainties in the resulting EGB, which are very likely dominated by systematics in the modeling. Fig. 4.1 illustrates that the star-forming galaxy contribution to the EGB depends on the details of how these galaxies evolve, through a starburst to a normal phase. Using our suite of models we will compare with the observed EGB to determine the fraction of the EGB allowed for star-forming galaxies, and its uncertainty.

4.1.1.3 Discussion

This work will provide a rigorous, empirically-calibrated prediction of a major portion of the Fermi EGB signal. The star-forming signal offers a new probe of cosmic star formation. Detection of this signal also will provide direct evidence for cosmic ray acceleration (and associated energy inputs, interactions, and feedback) throughout the star-forming universe. Indeed, the star-forming signal provides a unique and direct measure of cosmic-ray activity over cosmic time. More broadly, star-forming galaxies and active galaxies represent the

two "guaranteed" EGB components. The residuals form the star-forming galaxies thus must either be accounted for by active galaxies, or a new source is needed. Our work allows the EGB to place limits on more exotic components such as that due to dark matter annihilation. In addition, star-forming galaxies are also neutrino sources, thus this EGB work will also provide clues to the diffusive neutrino background study.

4.1.2 Future Prospects of Starburst Study

Multi-wavelength Analysis of NGC253 We are currently collaborating with Tonia Venters to work on the multi-wavelength emissions (mainly from X-rays to TeV) from starburst galaxy NGC 253, with the new 8 years Fermi/LAT data and reanalyzed HESS data (H. E. S. S. Collaboration et al., 2018). A hard and robust "lower limit" on the leptonic emission comes from the secondary electron contributions that inevitably follows the hadronic emission. So we will use this to put a firm lower bound on the X-ray emission from NGC 253. Any X-ray signal from NGC 253 above our lower bound must be due to primary electrons, and thus constrains the primary e/p ratio. Therefore NuSTAR's data (Wik et al., 2014) could be used to constrain our models. In this work, there are complications that will lead to a range of model predictions, like advection losses, re-acceleration, distributions in the initial cosmic ray injection index, and we will limit to explore the most important ones. We will also make predictions for future observations, as future data would put real constraints on starburst scenarios: a) hard X-rays should test and perhaps detect the leptonic component, giving us the e/p ratio and/or some measure of the advection losses of cosmic rays inside the galaxy; b) whether MeV measurements around 100 MeV see a feature of the pion bump will directly determine the signal is dominantly from hadronic emission or not; c) CTA in TeV range will not only do the spectrum measurement precisely, but may also resolve the emission spatially, and thus will be a unique new probe of the size of the emitting region and thus of the particle sources and propagation.

Neutrinos from Starbursts A high-energy neutrino is detected by IceCube recently and is spatial correlated with a blazar (IceCube et al., 2018), suggesting blazars as neutrino sources. So now it's a good time to look at cosmic neutrinos. Star-forming galaxies, especially starbursts, are plausible high-energy neutrino sources. Cosmic neutrinos are also generated through the same hadronic interactions between cosmic rays and the interstellar medium, in addition to gamma-ray photons. Based on my starburst work in Chapter. 2, the neutrino fluxes from nearby starbursts are too faint to be seen by current neutrino detectors. But the starbursts may also contribute to the measured diffusive neutrino background. Recent works have shown that whether starbursts are measured neutrino sources still remains controversial. Following the similar technique for the gamma ray modeling, I would like to calculate the neutrino flux from individual starbursts, and thus also getting the upper-limit to the contribution of star-forming galaxies (assuming all star-forming galaxies are 100% proton calorimetric starbursts) to the diffusive neutrino background. We would expect to see neutrinos from star-forming galaxies in the near future with improved detectors.

Open Questions There still remain a number of questions unanswered about the starburst galaxies, some may be addressed with the improved observations: a) whether hadronic or leptonic process dominates the gamma ray emissions from starburst galaxies; b) whether the average supernovae activities (acceleration efficiency, output energy) are same or not in starbursts and ULIRGs; c) whether the scaling relations of supernova rate/SFR are same in starbursts, ULIRGS, and our Milky Way; .... We expect future work to uncover the mysteries of star-forming galaxies with more precise observations.

4.2 Preliminary and Future Work in Type Ia Supernovae

An obvious next step to our current SNIa work would be building pipelines for Fermi/GBM and doing Monte Carlo simulations of various SNIa models.

4.2.1 Fermi/GBM background analysis and deep learning algorithm for supernova-like point sources search

A natural future work for SNIa is to built pipelines for Fermi/GBM to monitor SNIa-like objects and analyze the background of the detectors.

4.2.1.1 Introduction

Fermi/GBM is a powerful and unique tool to identify high energy transients in and beyond our Galaxy, because it constantly monitors the sky, and the Galaxy is transparent to gamma rays. Although GBM is optimized for gamma ray burst (GRB) detection, as astronomy opens time domain, it's also important to keep an open mind for longer-lived gamma ray transients like Type Ia supernovae.

For long duration transients (rise times last ∼hours or more), GBM's GRB-based alerts will probably not be triggered, and the signal could go missed, hidden in the detectors' background which varies with the spacecraft rocking and geomagnetic location. Hence new analyses and algorithms are needed to search existing data, analyze GBM background and prepare for future transients.

We will do a new analysis of GBM data over long timescales. We will characterize the background and its variations with, e.g., the solar cycle, and we will develop algorithms for extracting signals from the background. These results will be useful for other GBM

This section derives from a Fermi proposal written by Wang, X., & Fields, B.

applications in addition to GRB triggering, such as finding hidden signals like SNIa signal in background data, studies of long-duration emission from gamma-ray bursts, and of solar flares, and check on instrumental stability.

4.2.1.2 Method

Long-duration transients can fail to trigger GBM detectors, but would likely appear as an increase in the background signal. To detect such transient events, it is essential to characterize GBM background variations over time.

We will analyze GBM data to look at long-term background time variability. For our purposes we can exclude orbits passing the South Atlantic Anomaly (SAA). We will characterize background as a function of energy, over timescales of days to years, durations much longer than have been studied in detail heretofore. For each GBM detector, we will provide lightcurves as a function of energy, and characterize the variance and drift in mean. We will also look at the variation over 15 and 30 orbit periods, when Fermi returns to the same geomagnetic location. We will compare variations between the two BGO detectors and among the 12 NaI detectors to check for same time variability, which could hint at instrument issues.

We also analyze the background in particular line energies of interest; e.g., SNIa Co and Ni lines, the 511 keV positron annihilation line and 2.22 MeV neutron capture line that arise in solar flares, and the diffuse lines from 26Al and 60Fe decays. For example, the left panel of Fig. 4.2 shows the comparison of one-day background signal in the bin containing the 847 keV ^{56}Ni line, for a BGO detector in different years. The variations here over solar cycle may be due to the filtering effect of our earth's magnetosphere. Moreover, we will plot line/line ratio and line/continuum ratio to look for energy dependent variability of GBM background. We expect the low energy versus high energy ratios to follow the solar cycle, since low energy background is astrophysical while high energy background is due to the cosmic ray interactions in spacecraft and the earth.

We have built Wang & Fields (2018)'s models in Chapter. 3 that explore the SN gamma-

ray emission in a range of ejecta scenarios. These will generate templates for our study of the SNIa signal in GBM. The SN gamma-ray sources are the ^{56}Ni $\rightarrow$ ^{56}Co $\rightarrow$ ^{56}Fe radioactive decays, whose lines are emitted in precisely known ratios, and their observed widths encode information about ejecta dynamics and energetics (Sim & Mazzali, 2008; The & Burrows, 2014).

In the right panel of Fig. 4.2, we see a 1-day light curve for 4 energy bins surrounding the 847 keV ^{56}Co line, at 24 days after explosion. The top panel shows background, represented by real BGO data from 21 Feb 2017. The middle panel shows the SN signal, with time structure reflecting the changing angle from the SN to the BGO detector, calculated from the Spacecraft Pointing file[1]. The complicated structure reflects the BGO angular response (here assumed a cosine) and a combination of Fermi's rocking, orbit, and roll to keep the solar panels facing sunwards. This distinct, periodic lightcurve is well-determined for each possible SN location in the Galactic disk. Sounding the SN alarm then amounts to identify and confirm this signal as early as possible.

Taking SNIa for example, we will develop a set of templates for SN light curves and spectra, varying SN parameters (^{56}Ni mass and distribution), and location in the Galactic plane. Using these we will simulate the SN signal in the GBM, where the background at the relevant energies is dominated by cosmic rays. The earlier the rising SN lines can be reliably found, the better. We must search noisy background for signals that match known templates; this situation is similar to that facing LIGO.

We thus will adapt a new and powerful LIGO-inspired neural network deep learning algorithm (George & Huerta, 2016) to search for and extract a SN signal from the data. We will train and test the algorithm on existing GBM data with fake SN signals injected; a by-product of this analysis will be a characterization of the GBM background over long timescales. We also will determine the timescales at which the earliest reliable detection will occur. This algorithm could also be generalized to other point sources especially long

[1] `https://fermi.gsfc.nasa.gov/ssc/observations/timeline/ft2/`

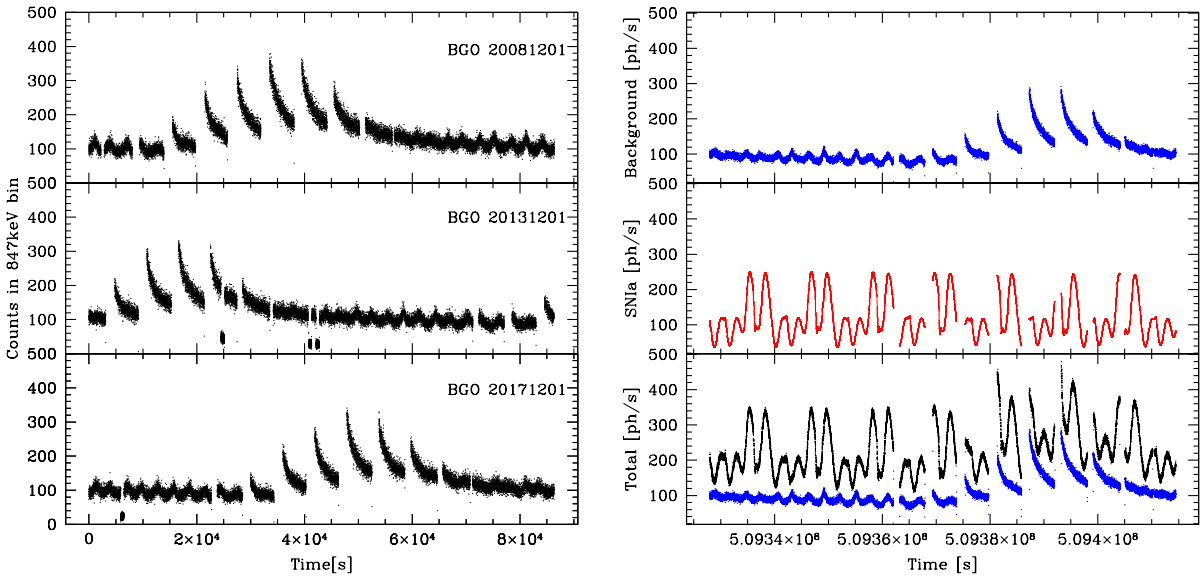

Figure 4.2: BGO background signal variation and BGO response to SNIa. *Left:* Background signal in one BGO detector over one day in different years, in energy bins containing 847 keV line arising in ^{56}Ni decay as expected in a SNIa. *Right:* Simulated BGO response to a SNIa over one day, in energy bins containing 847 keV line. Top panel: GBM data (blue), representing typical background. Middle panel: SN signal (red). Botton panel: total signal (black), summing SN and background.

duration transients.

In order to follow up a GBM SNIa like long duration transients detection, we must infer the location of the event as precisely as possible. The algorithms developed above will simultaneously localize the source, via cross correlation–phase lag of the signal detected in multiple GBM detectors and comparing the signal peak with the characterized pure background peak. This technique will provide direction information of the source in complementary to the Earth occultation technique (Wilson-Hodge et al., 2012). We will use Crab to test the localization precision of our search technique. Furthermore, *Swift* followup could leverage the superior positional resolution of *Swift*/BAT, and possibly still better localization from *Swift*/XRT if there is an X-ray signal.

4.2.1.3 Conclusion

Our work will provide a new analysis of GBM data over long timescales. We will characterize the background and its variations with, e.g., the solar cycle, and we will develop algorithms for extracting signals from the background. These results will be useful for other GBM applications, such as studies of long-duration emission from gamma-ray bursts, and of solar flares. *These benefits will accrue even if no SNIa occurs in Fermi's lifetime and work for future burst alert detectors.*

4.2.2 Monte Carlo Simulations for SNIa Ejecta Model

With the ^{56}Ni shell model in Chapter. 3, we can estimate the alert timescale of a Galactic SNIa can be as short as first days after its explosion. Although the ^{56}Ni shell model worked for SN2014J, it's not guaranteed this model is the actual case. When the SNIa signal is distinctive from GBM background depends the ejecta scenario adapted in our model. Therefore we'll also build models with a range of ejecta structures (like mixed structure and "onion skin"), following Sim & Mazzali (2008) and The & Burrows (2014)'s work, to do a Monte Carlo simulation of the the signal from a SNIa and fit to SN2014J's gamma-ray data, to determine which model works best based on current observations.

We find that the early phase observation will determine the ejecta structure; while late stage will give a direct measurement of ^{56}Ni mass. Shown in Fig. 3.5, the signal is sensitive to the ^{56}Ni location at early days while merge to the same at late days with the same ^{56}Ni mass. And the fluxes at line energy bin are expected to vary over time following the decay feature, appeared in Fig. 4.4 for example.

4.2.3 Future Observations of Type Ia Supernova

With several large synoptic surveys, such as LSST, and next generation gamma-ray telescopes, like AMEGO or e-ASTROGAM, either ready to come online or under proposal, the

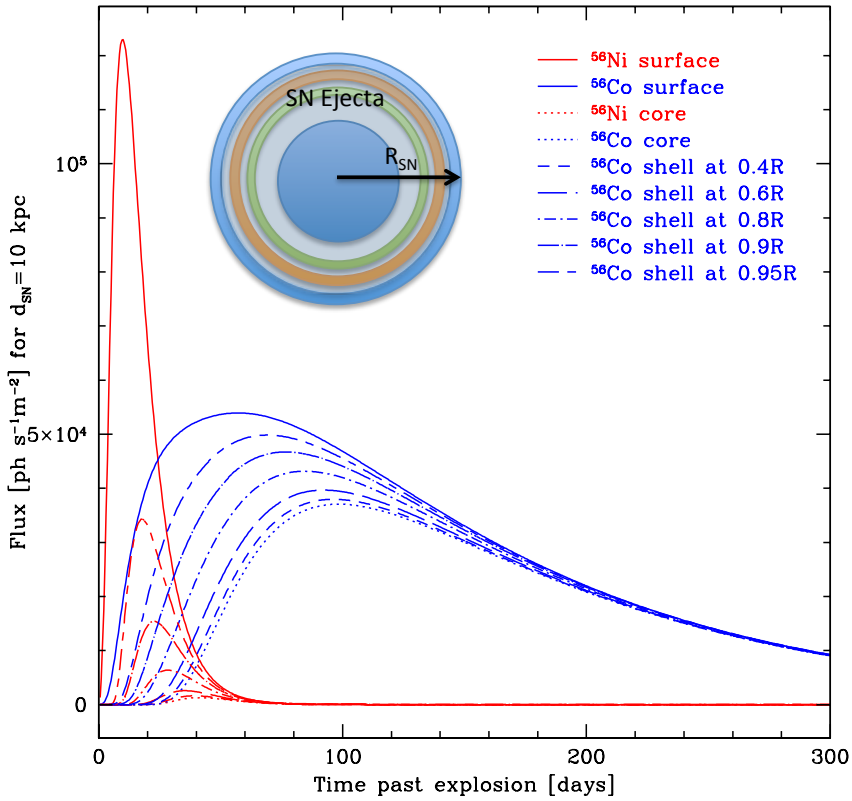

Figure 4.3: Simulation of light curves from a 10 kpc SNIa shells. Red lines are the 56Ni gamma-ray signal intensity variations while blue lines are 56Co gamma-ray signals from different 56Ni distributions in the ejecta (from outermost shell/surface to the innermost core), respectively. The ^{56}Ni in each shell is 0.05 solar mass.

coming decade will be an exciting time for astrophysics and cosmology. Transients, especially supernovae, will be well studied through the upgraded multi-messenger detections, and we hope a Galactic supernovae event would happen and observed if lucky enough. These improvements will greatly benefit our understandings of stars, galaxies and the Universe.

4.2.3.1 Gamma Ray Observations

We recommend the following gamma ray detectors to prepare for the inevitable and exciting Type Ia event in the future.

(a) As we have shown in Chapter. 3, we recommend that future gamma-ray burst missions

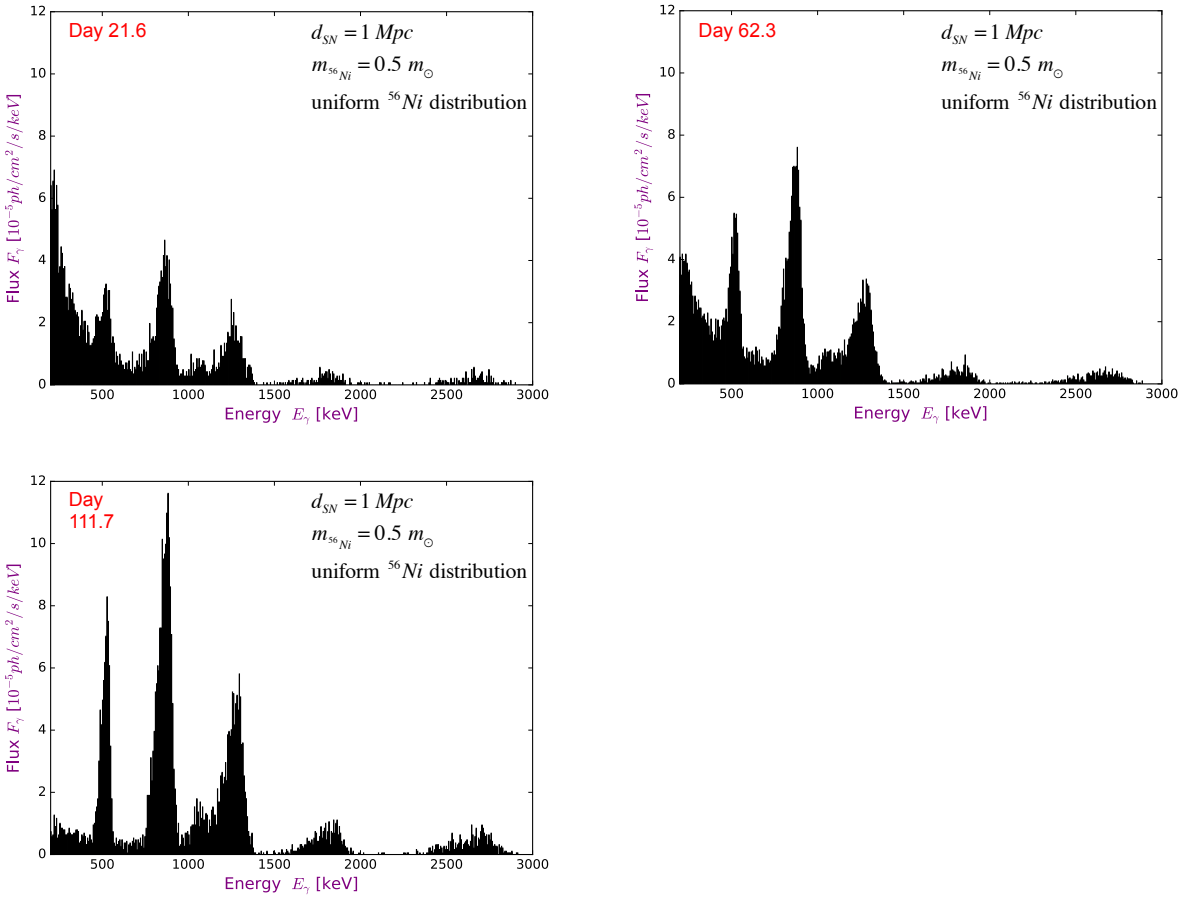

Figure 4.4: Simulated ^{56}Co lines energy spectra from a SNIa with the uniform ^{56}Ni distribution at day 21.6, 62.3 and 11.7 after the explosion, respectively. The SNIa is assumed to be 10kpc away with total ^{56}Ni to be 0.5 solar mass.

succeed existing missions without gaps in time, with visits to the Galactic Plane in the scans, and ideally sensitivity to higher energy photons; the SNIa search can piggyback on the ordinary GRB-focused observing strategy at no additional cost. A Swift-like X-ray and UVOT combination would be very useful for rapid localization and initial multi-wavelength observations.

(b) MeV telescopes with large fields of view like AMEGO or e-ASTROGAM will be ideal, with good resolution to see all of the brightest ^{56}Ni and ^{56}Co lines and measure the line shapes, gaining information about SNIa explosion and position. The 511keV line, which maps the positron annihilation and thus separately probes density, will also be detectable.

If there is sensitivity to the gamma line polarization, this will give even more information of SNIa Churazov & Khabibullin (2018). Such missions will likely detect extragalactic SNIa as well.

Take AMEGO for example. The All-Sky Medium Energy Gamma-ray Observatory (AMEGO) will scan the entire sky every 3 hours from $\sim 200keV$ to $\geq 10GeV$, covering 80% of the sky every orbit with a FOV of ∼2.5 steradian. Most of the SNIa gamma-ray lines are squarely within the AMEGO energy range. Thus AMEGO will be an ideal monitor and early warning system for SNIa from the Milky Way and nearby obscured starburst regions. The early stage observations of SNIa will allow us to explore the progenitor types and the ejecta structure (nucleosynthesis) of SNIa. And the SNIa in dusty starbursts discovered by AMEGO will help probe star-formation rate and test scaling relations like supernova rate/star-formation rate. Moreover, with the excellent polarization and nuclear line sensitivity, AMEGO will be able to finely detect SNIa at a rate of ∼2 events/yr, with a total ∼20 SNIa over the mission lifetime to sample SNIa, as shown in Fig. 4.5. Although the detection rate is still small, it's already 100 times higher than the Galactic SNIa rate, and it may be is enough considering that this estimation takes 10% of AMEMGO observing time each year, if we want AMEGO to observe the SNIa at 4 different epochs, each with a 10-day durations. The high SNIa detection rate will also enable the precise and accurate measurements of the total ^{56}Ni mass of SNIa, testing the cosmic distance calibration and probe the cosmic acceleration.

Therefore, AMEGO will detector more gamma-ray SNIa for sampling as well as the precise and accurate measurement of ^{56}Ni mass synthesized, which is important for the "standard model" application in cosmology. Moreover, AMEGO will also explore the long-lived 44Ti, 27Al, 60Fe nuclear lines, and the 511 keV line from electron-positron annihilation.

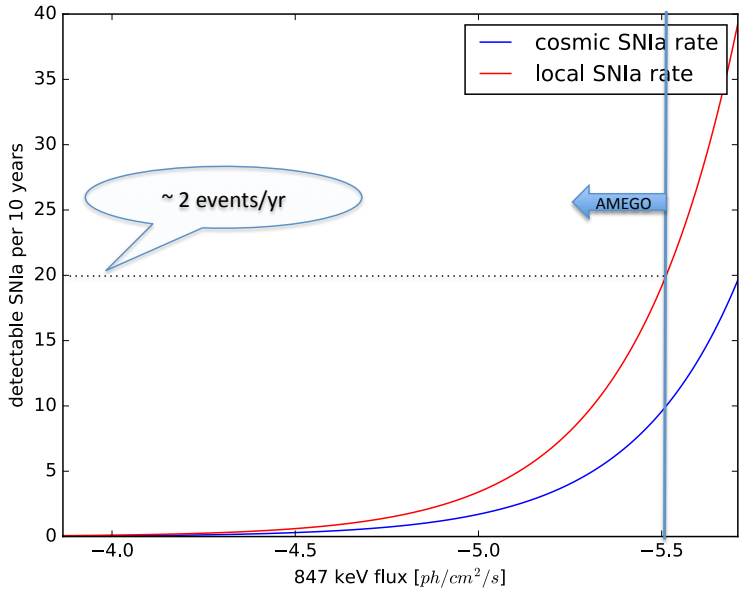

Figure 4.5: Total number of gamma-ray detectable SNIa per 10 years, as a function of the 847 keV ^{56}Co line flux (calibrated from SN2014J's 847 keV line of $1.0*10^{-4}ph/cm^2/s$ at 100 day (Churazov et al., 2015)). The blue curve is calculated basing on the cosmic SNIa rate ($\sim 3*10^5 events/Mpc^3/yr$ Horiuchi & Beacom (2010)), red curve is based on the local SNIa rate (estimated to be 2 times higher than the cosmic rate, considering about the Virgo galaxy cluster and the existence of the obscured SNIa (e.g., Horiuchi & Beacom, 2010; Smartt et al., 2009)). With sensitivity $F_{3\sigma} \sim 3*10^{-6}ph/cm^2/s$, AMEGO is expected to detect $\sim$ 20 events per 10 years.

4.2.3.2 LSST Observation

The next-generation synoptic survey–the Large Synoptic Survey Telescope (LSST)– will be a 8.4 meter telescope located in Cerro Pachon, Chile. It will have a special three-mirror design that produces a particularly large field-of-view. In the scanning mode, the telescope will be capable of observing the entire available sky every ∼3 days. About 90% of the survey time will be carried out in this mode with a single-visit depth of ∼25mag, which is much better than the ∼20mag to 22mag survey depths of the contemporary synoptic surveys. The remaining 10% survey time will be carried out in a deep mode with greater single-visit depth of ∼27mag. This time will be dedicated to very deep surveys of a variety of special regions.

Adams et al. (2013) found that the the optical/near-IR scanning of LSST can detect over 99% of Galactic SNIa at peak in the brightest observable waveband, assuming LSST always monitors the Galactic plane. This is a welcome news, and LSST will play a crucial role in the event of a Galactic SNIa. However, in practice one must not only *detect* but also *identify* the SNIa. Several practical issues can delay the LSST identification until after the SNIa peak: (a) the LSST observing season (air mass <1.5), is only about 7 months per year (i.e., 60%) for the inner Galactic plane [2]; (b) even if the SNIa happens during the observing season, the present "baseline" of LSST observing strategy *minion*_1016 (LSST Science Collaboration et al., 2017) *will not visit the Galactic plane at all beyond the first 7 months*; (c) even the alternate proposed strategy *astro_lsst*_01_1004 having Galactic plane scans throughout the LSST mission, the cadence is reduced to one visit every $\sim$ 10 days; (d) the explosion will occur randomly in the LSST filter cycle, and identification will involve comparing magnitudes and colors among filters that may not at first be optimal. Thus the identification of a SNIa may be delayed until after the optical peak, and the opportunity for early followup will be lost. LSST will very probably discover a Galactic SNIa eventually, but if another search could identify a SNIa soon after the explosion, combing this search with LSST makes a more effective alarm and localization strategy. Also we strongly urge that LSST scans the Galactic Plane over the entire mission duration, ideally with the same cadence as the main wide-fast-deep survey.

We will work on the LSST observation strategies for the Galactic SNIa, as well as other Galactic transients like novae. We will map the spatial and probability distribution of these transients based on supernova remnants observations(Green, 2015) and simulations (Adams et al., 2013). We will also evaluate LSST's detection sensitivity and observing time in the Milky Way events.

The future observations of a nearby SNIa would uniquely advance a wide variety of astronomy research. (a) Type Ia explosions serve as "standarizable" candles and thus cosmic

[2] `https://www.eso.org/sci/observing/tools/calendar/observability.html`

distance indicators, famously leading to the discovery of cosmic acceleration. Multiwavelength observations of a nearby Type Ia event would offer a powerful new probe of the Phillips relation used to standardize the lightcurves (Phillips, 1993). (b) The nature of Type Ia progenitors remains a mystery (single vs double degenerate scenarios). A nearby SNIa would offer unique insight into the progenitor, e.g., via radio and X-ray probes of the circumstellar environment. (c) SNIa are also the dominant cosmic source of iron-group elements. The gamma ray observations will precisely measure the ^{56}Ni mass, the gamma-ray line shapes and the light curves would diagnose the explosion features and spatial information of the supernova, as well as encode a map of the structure and mixing of the ejecta. Thus we look forward to seeing the next Galactic supernova in multi-messenger observations!

4.3 Spallation of the R-process Elements from the Neutron Star Mergers

Neutron star mergers are the nucleosynthesis sites for r process elements, confirmed by the recent spectacular event GW170817 (Abbott et al., 2017). The synthesized heavy r-process nucleons will be ejected from the mergers at a very high velocity $\sim$0.1-0.2c. Thus these r-process nuclei will have high kinetic energy ranging from $\sim$10 MeV to $\sim$1000 MeV. They will hit the surrounding interstellar medium and lose energy through nuclear reactions, elastic scattering and ionization energy loss processes (ionization loss dominates at MeV energy range). This energy loss calculation will be similar to the cosmic ray propagation calculation in Chapter. 2. The nuclear reactions will usually remove one or a few nucleons from the heavy r-process nuclei. This process is called as spallation. Therefore, the spallation from neutron star mergers will increase the r-process elements at abundance "valley" while decrease the abundance "peak", matching the observed solar r-process abundance pattern. Comparing the spallation results with observations will also help explore the r-process nucleosynthesis and surrounding environments of neutron star mergers. Currently we are working with

Rebecca Surman on this project. We will start with the third peak elements of the r-process abundance pattern, which are more sensitive to the abundance change due to the spallation, to test the effect of spallation on the abundance at the "valley". We assume the ejected material is in adiabatically expanding. We find that the neutron spallation reactions, which have larger cross sections, matters in the first several year after the explosion when the neutron decay rate is smaller than the nuclear reaction rate.

References

Abbott, B. P., Abbott, R., Abbott, T. D., et al. 2017, ApJ, 848, L12

Abbott, T., Akiba, Y., Beavis, D., et al. 1992, Phys. Rev. D, 45, 3906

Abdo, A. A., Ackermann, M., Ajello, M., et al. 2009, Physical Review Letters, 103, 251101

Abdo, A. A., Ackermann, M., Ajello, M., et al. 2010, A&A, 512, A7

Abdo, A. A., Ackermann, M., Ajello, M., et al. 2010, A&A, 523, A46

Abdo, A. A., Ackermann, M., Ajello, M., et al. 2010, A&A, 523, L2

Abdo, A. A., Ackermann, M., Ajello, M., et al. 2010, ApJ, 709, L152

Abramowski, A., Acero, F., Aharonian, F., et al. 2012, ApJ, 757, 158

Acciari, V. A., Aliu, E., Arlen, T., et al. 2009, Nature, 462, 770

Acero, F., Aharonian, F., Akhperjanian, A. G., et al. 2009, Science, 326, 1080

Acero, F., Ackermann, M., Ajello, M., et al. 2016, ApJS, 224, 8

Ackermann, M., Ajello, M., Allafort, A., et al. 2012, ApJ, 755, 164

Ackermann, M., Ajello, M., Allafort, A., et al. 2013, Science, 339, 807

Ackermann, M., Ajello, M., Albert, A., et al. 2015, ApJ, 799, 86

Adams, S. M., Kochanek, C. S., Beacom, J. F., Vagins, M. R., & Stanek, K. Z. 2013, ApJ, 778, 164

Aharonian, F., Akhperjanian, A. G., Bazer-Bachi, A. R., et al. 2005, A&A, 441, 465

Aharonian, F., Akhperjanian, A. G., Bazer-Bachi, A. R., et al. 2008, A&A, 481, 401

Ahlers, M., & Murase, K. 2014, Phys. Rev. D, 90, 023010

Aliu, E., Archambault, S., Arlen, T., et al. 2013, ApJ, 764, 38

Ajello, M., Greiner, J., Sato, G., et al. 2008, ApJ, 689, 666

Ajello, M., Gasparrini, D., Sánchez-Conde, M., et al. 2015, ApJ, 800, L27

Anchordoqui, L. A., Goldberg, H., Halzen, F., & Weiler, T. J. 2004, Physics Letters B, 600, 202

Baade, W., & Zwicky, F. 1934, Proceedings of the National Academy of Science, 20, 259

Baumgartner, W. H., Tueller, J., Markwardt, C. B., et al. 2013, ApJS, 207, 19

Bell, A. R. 1978, MNRAS, 182, 147

Blandford, R. D., & Ostriker, J. P. 1978, ApJ, 221, L29

Blandford, R., & Eichler, D. 1987, Phys. Rep., 154, 1

Blasi, P., & Amato, E. 2012, JCAP, 1, 10

Blom, J. J., Paglione, T. A. D., & Carramiñana, A. 1999, ApJ, 516, 744

Bussard, R. W., Burrows, A., & The, L. S. 1989, ApJ, 341, 401

Caprioli, D. 2012, JCAP, 7, 38

Chabrier, G. 2003, PASP, 115, 763

Chakraborty, N., & Fields, B. D. 2013, ApJ, 773, 104

Chupp, E. L., Forrest, D. J., Higbie, P. R., et al. 1973, Nature, 241, 333

Churazov, E., Sunyaev, R., Isern, J., et al. 2015, ApJ, 812, 62

Churazov, E., & Khabibullin, I. 2018, MNRAS,

Clayton, D. D., Colgate, S. A., & Fishman, G. J. 1969, ApJ, 155, 75

Clayton, D. 2003, Handbook of Isotopes in the Cosmos, by Donald Clayton, pp. 326. ISBN 0521823811. Cambridge, UK: Cambridge University Press, October 2003., 326

Clifford, F. E., & Tayler, R. J. 1965, MmRAS, 69, 21

Colgate, S. A., & McKee, C. 1969, ApJ, 157, 623

de Cea del Pozo, E., Torres, D. F., & Rodriguez Marrero, A. Y. 2009, ApJ, 698, 1054

Dermer, C. D. 1986, A&A, 157, 223

Dermer, C. D. 2007, The First GLAST Symposium, 921, 122

Dermer, C. D., & Powale, G. 2013, A&A, 553, A34

Diehl, R., Siegert, T., Hillebrandt, W., et al. 2014, Science, 345, 1162

Diehl, R., Siegert, T., Hillebrandt, W., et al. 2015, A&A, 574, A72

Domingo-Santamaría, E., & Torres, D. F. 2005, A&A, 444, 403

Downes, D., & Eckart, A. 2007, A&A, 468, L57

Eichmann, B., & Becker Tjus, J. 2016, ApJ, 821, 87

Evoli, C., Gaggero, D., Grasso, D., & Maccione, L. 2008, JCAP, 10, 18

Feenberg, E., & Primakoff, H. 1948, Physical Review, 73, 449

Fermi Collaboration, 2013, proc. ICRC, p. 1165

Fields, B. D., Olive, K. A., & Schramm, D. N. 1994, ApJ, 435, 185

Fields, B. D., Olive, K. A., Cassé, M., & Vangioni-Flam, E. 2001, A&A, 370, 623

Fields, B. D., Pavlidou, V., & Prodanović, T. 2010, ApJ, 722, L199

Fitzpatrick, G., Connaughton, V., McBreen, S., & Tierney, D. 2011, arXiv:1111.3779

Fitzpatrick, G., McBreen, S., Connaughton, V., & Briggs, M. 2012, Proc. SPIE, 8443, 84433B

Foreman, G., Chu, Y.-H., Gruendl, R., et al. 2015, ApJ, 808, 44

Forrest, D. J., & Chupp, E. L. 1983, Nature, 305, 291

Fox, O. D., & Casper, C. 2015, IAU General Assembly, 22, 2258045

Gao, Y., & Solomon, P. M. 2004, ApJ, 606, 271

George, D., & Huerta, E. A. 2016, arXiv:1701.00008

Ginzburg, V. L., & Syrovatskii, S. I. 1964, The Origin of Cosmic Rays, New York: Macmillan, 1964

Gould, R. J. 1982, ApJ, 263, 879

Green, D. A. 2015, MNRAS, 454, 1517

Griffin, R. D., Dai, X., & Thompson, T. A. 2016, ApJ, 823, L17

Halzen, F., & Hooper, D. 2002, Reports on Progress in Physics, 65, 1025

Hassan, T., Arrabito, L., Bernlör, K., et al. 2015, preprint (arXiv:1508.06075)

Hayakawa, S. 1952, Progress of Theoretical Physics, 8, 571

Hayashida, M., Stawarz, Ł., Cheung, C. C., et al. 2013, ApJ, 779, 131

Helder, E. A., Vink, J., Bassa, C. G., et al. 2009, Science, 325, 719

H. E. S. S. Collaboration, 2011, Proc. 25th TEXAS Symposium, Relativistic Astrophysics, preprint (arXiv:1104.5003)

H. E. S. S. Collaboration, Abdalla, H., Aharonian, F., et al. 2018, arXiv:1806.03866

Horiuchi, S., Beacom, J. F., & Dwek, E. 2009, Phys. Rev. D, 79, 083013

Horiuchi, S., & Beacom, J. F. 2010, ApJ, 723, 329

Horiuchi, S., Beacom, J. F., Kochanek, C. S., et al. 2011, ApJ, 738, 154

Hopkins, A. M. 2004, ApJ, 615, 209

Iben, I., Jr., & Tutukov, A. V. 1984, ApJS, 54, 335

IceCube Collaboration et al. 2014, ApJ, 796, 109

IceCube, T., Fermi-LAT, MAGIC, et al. 2018, arXiv:1807.08816

Janka, H.-T., Langanke, K., Marek, A., et al. 2007, Phys. Rep., 442, 38.

Johansson, J., Goobar, A., Kasliwal, M. M., et al. 2017, MNRAS, 466, 3442

Kamae, T., Karlsson, N., Mizuno, T., Abe, T., & Koi, T. 2006, ApJ, 647, 692

Kang, H., Jones, T. W., & Edmon, P. P. 2013, ApJ, 777, 25

Kasen, D. 2006, ApJ, 649, 939

Kelner, S. R., Aharonian, F. A., & Bugayov, V. V. 2006, Phys. Rev. D, 74, 034018

Kennicutt, R. C., Jr. 1998, ApJ, 498, 541

Kennicutt, R. C., & Evans, N. J. 2012, ARA&A, 50, 531

Klebesadel, R. W., Strong, I. B., & Olson, R. A. 1973, ApJ, 182, L85

Krause, O., Tanaka, M., Usuda, T., et al. 2008, Nature, 456, 617

Kraushaar, W., Clark, G. W., Garmire, G., et al. 1965, ApJ, 141, 845

Krimm, H. A., Holland, S. T., Corbet, R. H. D., et al. 2013, ApJS, 209, 14

Krumholz, M. R. 2014, Phys. Rep., 539, 49

Krymskii, G. F. 1977, Akademiia Nauk SSSR Doklady, 234, 1306

Kurfess, J. D., Johnson, W. N., Kinzer, R. L., et al. 1992, ApJ, 399, L137

Lacki, B. C., Thompson, T. A., & Quataert, E. 2010, ApJ, 717, 1

Lacki, B. C., & Thompson, T. A. 2010, ApJ, 717, 196

Lacki, B. C., Thompson, T. A., Quataert, E., Loeb, A., & Waxman, E. 2011, ApJ, 734, 107

Lacki, B. C., Horiuchi, S., & Beacom, J. F. 2014, ApJ, 786, 40

Lacki, B. C., & Thompson, T. A. 2013, ApJ, 762, 29

Lamastra, A., Menci, N., Fiore, F., et al. 2017, A&A, 607, A18

Lemoine-Goumard, M., Renaud, M., Vink, J., et al. 2012, A&A, 545, A28

Lichti, G. G., Bignami, G. F., & Paul, J. A. 1978, Ap&SS, 56, 403

Lien, A., & Fields, B. D. 2009, JCAP, 1, 47

Lien, A., & Fields, B. D. 2012, ApJ, 747, 120

Lien, A., Sakamoto, T., Barthelmy, S. D., et al. 2016, ApJ, 829, 7

Linden, T. 2017, Phys. Rev. D, 96, 083001

Loeb, A., & Waxman, E. 2006, JCAP, 5, 3

Longair, M. S. 1981, High energy Astrophysics, 1st edn., Cambridge Univ. Press, Cambridge and New York, p. 420

LSST Science Collaboration, Marshall, P., Anguita, T., et al. 2017, arXiv:1708.04058

Madau, P., Ferguson, H. C., Dickinson, M. E., et al. 1996, MNRAS, 283, 1388

Mahoney, W. A., Ling, J. C., & Wheaton, W. A. 1994, ApJS, 92, 387

Maoz, D., & Mannucci, F. 2008, MNRAS, 388, 421

Margutti, R., Parrent, J., Kamble, A., et al. 2014, ApJ, 790, 52

Matz, S. M., Share, G. H., Leising, M. D., et al. 1988, Nature, 331, 416

Meegan, C., Lichti, G., Bhat, P. N., et al. 2009, ApJ, 702, 791

Meneguzzi, M., Audouze, J., & Reeves, H. 1971, A&A, 15, 337

Meyer, J.-P. 1985, ApJS, 57, 173

Miller, M. L., Reygers, K., Sanders, S. J., & Steinberg, P. 2007, Annual Review of Nuclear and Particle Science, 57, 205

Morlino, G., & Blasi, P. 2016, A&A, 589, A7

Morlino, G., & Caprioli, D. 2012, A&A, 538, A81

Mori, M. 2009, Astroparticle Physics, 31, 341

Morrison, P. 1958, Il Nuovo Cimento, 7, 858

Murase, K., Ahlers, M., & Lacki, B. C. 2013, Phys. Rev. D, 88, 121301

Murase, K., & Waxman, E. 2016, Phys. Rev. D, 94, 103006

Nakamura, K., Horiuchi, S., Tanaka, M., et al. 2016, MNRAS, 461, 3296

Ng, K. C. Y., Horiuchi, S., Gaskins, J. M., Smith, M., & Preece, R. 2015, Phys. Rev. D, 92, 043503

Nolan, P. L., Abdo, A. A., Ackermann, M., et al. 2012, ApJS, 199, 31

Nomoto, K., Thielemann, F.-K., & Yokoi, K. 1984, ApJ, 286, 644

Odrzywolek, A., & Plewa, T. 2011, A&A, 529, A156

Ohm, S. 2016, Comptes Rendus Physique, 17, 585

Olive, K. A., & Particle Data Group 2014, Chinese Physics C, 38, 090001

Paglione, T. A. D., Marscher, A. P., Jackson, J. M., & Bertsch, D. L. 1996, ApJ, 460, 295

Paglione, T. A. D., & Abrahams, R. D. 2012, ApJ, 755, 106

Pavlidou, V., & Fields, B. D. 2001, ApJ, 558, 63

Pavlidou, V., & Fields, B. D. 2002, ApJ, 575, L5

Peng, F.-K., Wang, X.-Y., Liu, R.-Y., Tang, Q.-W., & Wang, J.-F. 2016, ApJ, 821, L20

Pérez-Torres, M. A., Lundqvist, P., Beswick, R. J., et al. 2014, ApJ, 792, 38

Perlmutter, S., Aldering, G., Goldhaber, G., et al. 1999, ApJ, 517, 565

Persic, M., Rephaeli, Y., & Arieli, Y. 2008, A&A, 486, 143

Phillips, M. M. 1993, ApJ, 413, L105

Pisarski, R. L., Helfand, D. J., & Kahn, S. M. 1984, ApJ, 277, 710

Planck Collaboration, Ade, P. A. R., Aghanim, N., et al. 2016, A&A, 594, A13

Pohl, M. 1993, A&A, 270, 91

Pohl, M. 1994, A&A, 287, 453

Powell, L. C., Slyz, A., & Devriendt, J. 2011, MNRAS, 414, 3671

Punch, M., Akerlof, C. W., Cawley, M. F., et al. 1992, Nature, 358, 477

Rephaeli, Y., Arieli, Y., & Persic, M. 2010, MNRAS, 401, 473

Rephaeli, Y., & Persic, M. 2013, Astrophys. Space Sci. Proc., Cosmic Rays in Star-Forming Environments, Vol. 34, Springer-Verlag Berlin, Heidelberg, p. 193

Reynolds, S. P., Borkowski, K. J., Hwang, U., et al. 2007, ApJ, 668, L135

Riess, A. G., Filippenko, A. V., Challis, P., et al. 1998, AJ, 116, 1009

Rodi, J., Cherry, M. L., Case, G. L., et al. 2014, A&A, 562, A7

Sakamoto, K., Wang, J., Wiedner, M. C., et al. 2008, ApJ, 684, 957-977

Salamon, M. H., & Stecker, F. W. 1998, ApJ, 493, 547

Sanders, D. B., Mazzarella, J. M., Kim, D.-C., Surace, J. A., & Soifer, B. T. 2003, AJ, 126, 1607

Sim, S. A., & Mazzali, P. A. 2008, MNRAS, 385, 1681

Slane, P., Lee, S.-H., Ellison, D. C., et al. 2014, ApJ, 783, 33

Smartt, S. J., Eldridge, J. J., Crockett, R. M., & Maund, J. R. 2009, MNRAS, 395, 1409

Stamatikos, M. 2009, arXiv:0907.3190

Stecker, F. W. 1970, Ap&SS, 6, 377

Stecker, F. W. 1971, NASA Special Publication, 249

Stecker, F. W., & Venters, T. M. 2011, ApJ, 736, 40

Stecker, F. W., Malkan, M. A., & Scully, S. T. 2012, ApJ, 761, 128

Stephens, S. A., & Badhwar, G. D. 1981, Ap&SS, 76, 213

Stephenson, F. R., & Green, D. A. 2002, Historical supernovae and their remnants, by F. Richard Stephenson and David A. Green. International series in astronomy and astrophysics, vol. 5. Oxford: Clarendon Press, 2002, ISBN 0198507666, 5,

Strong, A. W., Wolfendale, A. W., & Worrall, D. M. 1976, MNRAS, 175, 23P

Strong, A. W., & Moskalenko, I. V. 1998, ApJ, 509, 212

Strong, A. W., Moskalenko, I. V., & Ptuskin, V. S. 2007, Annual Review of Nuclear and Particle Science, 57, 285

Strong, A. W., Porter, T. A., Digel, S. W., et al. 2010, ApJ, 722, L58

Swanenburg, B. N., Bennett, K., Bignami, G. F., et al. 1978, Nature, 275, 298

The, L.-S., & Burrows, A. 2014, ApJ, 786, 141

Thompson, D. J., Fichtel, C. E., Kniffen, D. A., & Ogelman, H. B. 1975, ApJ, 200, L79

Thompson, T. A., Quataert, E., & Waxman, E. 2007, ApJ, 654, 219

Torres, D. F. 2004, ApJ, 617, 966

Torres, D. F., Cillis, A., Lacki, B., & Rephaeli, Y. 2012, MNRAS, 423, 822

Tueller, J., Barthelmy, S., Gehrels, N., et al. 1990, ApJ, 351, L41

Tueller, J., Baumgartner, W. H., Markwardt, C. B., et al. 2010, ApJS, 186, 378

Tully, R. B., Rizzi, L., Shaya, E. J., et al. 2009, AJ, 138, 323

Tunnard, R., Greve, T. R., Garcia-Burillo, S., et al. 2015, ApJ, 800, 25

VERITAS collaboration, 2015, PoS ICRC, p. 745

Voelk, H. J. 1989, A&A, 218, 67

Wang, X., & Fields, B. D. 2014, American Institute of Physics Conference Series, 1595, 231

Wang, X., & Fields, B. D. 2016, PoS ICRC **2015**, 905 (2016).

Wang, X., Fields, B., & Lien, A. 2015, 34th International Cosmic Ray Conference (ICRC2015), 34, 904

Wang, X., & Fields, B. D. 2018, MNRAS, 474, 4073

Webbink, R. F. 1984, ApJ, 277, 355

Webbink, R. F. 2010, American Institute of Physics Conference Series, 1314, 217

Whelan, J., & Iben, I., Jr. 1973, ApJ, 186, 1007

Wik, D. R., Lehmer, B. D., Hornschemeier, A. E., et al. 2014, ApJ, 797, 79

Wilson, C. D., Rangwala, N., Glenn, J., et al. 2014, ApJ, 789, L36

Wilson-Hodge, C. A., Case, G. L., Cherry, M. L., et al. 2012, ApJS, 201, 33

Woosley, S. E., & Weaver, T. A. 1995, ApJS, 101, 181

Woosley, S. E., Heger, A. & Weaver, T. A. 2002, Reviews of Modern Physics, 74, 1015.

Yoast-Hull, T. M., Everett, J. E., Gallagher, J. S., III, & Zweibel, E. G. 2013, ApJ, 768, 53

Yoast-Hull, T. M., Gallagher, J. S., III, Zweibel, E. G., & Everett, J. E. 2014, ApJ, 780, 137

Yoast-Hull, T. M., Gallagher, J. S., & Zweibel, E. G. 2015, MNRAS, 453, 222

Yoast-Hull, T. M., Gallagher, J. S., III, Aalto, S., & Varenius, E. 2017, MNRAS, 469, L89

Zhao, F.-Y., Strom, R. G., & Jiang, S.-Y. 2006, ChJAA, 6, 635